batteries

MDPI

Review

Emerging Capacitive Materials for On-Chip Electronics Energy Storage Technologies

Bukola Jolayemi [1,2], Gaetan Buvat [1,2,3], Pascal Roussel [3,*] and Christophe Lethien [1,2,4,*]

[1] Institut d'Electronique, de Microélectronique et de Nanotechnologies, Université de Lille, CNRS, Université Polytechnique Hauts-de-France, UMR 8520-IEMN, F-59000 Lille, France
[2] Réseau sur le Stockage Electrochimique de l'Energie (RS2E), CNRS FR 3459, 33 rue Saint Leu, 80039 Amiens CEDEX, France
[3] Unité de Catalyse et de Chimie du Solide (UCCS), Université de Lille, CNRS, Centrale Lille, Université d'Artois, UMR 8181–UCCS, F-59000 Lille, France
[4] Institut Universitaire de France (IUF), 92073 Paris, France
* Correspondence: pascal.roussel@univ-lille.fr (P.R.); christophe.lethien@univ-lille.fr (C.L.)

Abstract: Miniaturized energy storage devices, such as electrostatic nanocapacitors and electrochemical micro-supercapacitors (MSCs), are important components in on-chip energy supply systems, facilitating the development of autonomous microelectronic devices with enhanced performance and efficiency. The performance of the on-chip energy storage devices heavily relies on the electrode materials, necessitating continuous advancements in material design and synthesis. This review provides an overview of recent developments in electrode materials for on-chip MSCs and electrostatic (micro-/nano-) capacitors, focusing on enhancing energy density, power density, and device stability. The review begins by discussing the fundamental requirements for electrode materials in MSCs, including high specific surface area, good conductivity, and excellent electrochemical stability. Subsequently, various categories of electrode materials are evaluated in terms of their charge storage mechanisms, electrochemical performance, and compatibility with on-chip fabrication processes. Furthermore, recent strategies to enhance the performance of electrode materials are discussed, including nanostructuring, doping, heteroatom incorporation, hybridization with other capacitive materials, and electrode configurations.

Keywords: electrostatic (micro-/nano-)capacitors; micro-supercapacitors; on-chip micro-energy storage; EDLC; psedocapacitance; porous electrodes; multicationics

Citation: Jolayemi, B.; Buvat, G.; Roussel, P.; Lethien, C. Emerging Capacitive Materials for On-Chip Electronics Energy Storage Technologies. *Batteries* **2024**, *10*, 317. https://doi.org/10.3390/batteries10090317

Academic Editor: Douglas Ivey

Received: 22 July 2024
Revised: 20 August 2024
Accepted: 23 August 2024
Published: 7 September 2024

1. Introduction

The global consumer markets of artificial intelligence (AI) and internet of things (IoT) technology are expanding rapidly, thanks to wireless microsensor networks, wearable and implantable microelectronics, and other smart devices. These technologies find applications in home automation, medical control, space and defense surveillance, agriculture, environmental monitoring, unmanned aerial vehicles (UAVs), and industrial process tracking. However, the full autonomy of these wirelessly interconnected microelectronics is constrained by self-powering mechanisms, a major drawback of the technology. To overcome this limitation, energy scavenging/harvesting techniques such as solar cells [1,2] and nanogenerators [3,4] are used to harness and utilize ambient energy sources [5]. Intermittent and unstable energy generation sources necessitate complementary micro-energy storage technologies to capture the energy generated and deliver it on demand to mitigate discontinuity, periodicity, and indeterminacy [3,4,6–9]. Presently, the IoT industries are constrained by on-chip energy supply, which hinders their ability to meet the fast-growing consumer markets. Therefore, there is an urgent need for the expeditious implementation and improvement of on-chip electronics power sources to ensure self-powered and maintenance-free systems with minimal human intervention. By addressing these energy

constraints through careful design, optimization, and management strategies, IoT industries can create devices that deliver the desired functionality while maximizing energy efficiency and minimizing operational costs.

In recent years, microelectronic systems have continued to evolve towards ultra-miniaturized, flexible, aesthetic, versatile, and integrable devices in ultra-low form factors; they require commensurate features with on-chip electronics energy storage/supply modules [8,10]. The ongoing efforts to meet the energy requirements are enabled by technological advancements in system-on-chip (SoC) and system-in-package (SiP). SoC integrates multiple components of an electronic system into a single millimeter-sized silicon chip, and SiP incorporates various SoC components, such as sensors, data management units, radiofrequency transceivers, and energy supply units, into a single module to optimize space utilization. These technologies demand stringent requirements on the form factor of the on-chip energy supply unit, leading to the miniaturization of traditional energy storage systems like electrostatic capacitors, electrochemical capacitors or supercapacitors, and Li-ion batteries.

Miniaturization of classical energy storage systems through advanced microfabrication technologies has been remarkably prioritized in the expedition to meet the on-chip energy needs for IoT applications. The on-chip energy storage devices are miniaturized power sources integrated directly and seamlessly onto semiconductor chips to provide localized power supply solutions for various electronic devices, including IoT devices. They are designed to be compact with a footprint close to several square millimeters and the footprint of the electrode in the range, depending on the power/energy storage capacity and form factor requirements [1,6,9,11,12]. Considering the ultra-low form factors, downsizing the components of the energy storage devices, particularly the active materials (i.e., electrode materials/dielectrics), will inevitably jeopardize the energy and power deliveries since the performance of the device strongly relies on these materials [6,13–18]. As such, the energy and power densities are critically dependent on the electrode materials or dielectric properties, such as specific capacity/capacitance, rate capability, cycling stability, dielectric constant, voltage breakdown (in the case of electrostatic capacitors), and also the topology or configuration of the device [6,18].

The recent cutting-edge on-chip energy storage microsystems technologies have been focusing on engineering and developing new functional materials, innovative electrode design, and advanced microfabrication processes to concomitantly enhance the energy and power densities, aiming to improve the system performance, efficiency, and reliability in order to surmount the constraints of on-chip energy supply restricting the IoT industries to meet the fast-growing consumer markets. Miniaturized electrostatic capacitors (micro-capacitors), micro-supercapacitors (MSCs), and microbatteries (MBs) have drawn considerable attention as on-chip electronics energy storage systems. Recently, several authors have conducted reviews on emerging functional materials such as anode, cathode, and solid electrolyte materials used in MBs and provided state-of-the-art technologies [19–32]. The present review focuses on emerging (pseudo)capacitive materials used in electrostatic (micro-) capacitors and MSCs.

Electrostatic Metal/Insulator/Metal (MIM) (nano-/micro-) capacitors in silicon technology are essential components of any power distribution network in microelectronics; not only do they provide power to the microdevices, but they also subdue voltage instabilities [10]. They are known for delivering ultrahigh power density and ultra-fast charge/discharge rates, making them suitable for many high-power microelectronic systems, including DC/AC converters [33] and dynamic random-access memory (DRAM) circuits [34–37]. Apart from correcting the power factor, they are widely utilized in band-pass filters [38,39], and they can also perform specific functions, such as timing and decoupling. Their aim is to respond instantaneously to current peaks in the electrical circuit to which they are connected when used as decoupling elements [40]. They, therefore, reduce variations in the supply voltage, providing (very quickly) the amount of current needed to keep the voltage constant. They can be directly integrated via (i) conventional (2D hetero-

geneous integration of chips next to each other), (ii) on silicon interposers (2.5D integration, coupling the concept of side-by-side and 3D chip integration), or (iii) in 3D integration (vertical stacking) for optimal integration densification. However, the energy density is extremely low compared with MBs and MSCs, as revealed in the Ragone plot in Figure 1; this impedes its use in many applications compared to MSCs and MBs microdevices [36]. Nevertheless, the advantages of the micro-capacitors could be leveraged when coupled with other energy storage micro-devices, especially the MBs, to improve the overall performance and efficiency of the energy storage and delivery system; this configuration could enable ultrafast energy storage and release, commonly desirable in applications requiring high pulse discharge or high peak power, which MBs alone might not efficiently offer due to their typically much slower charge/discharge rate, though maintaining a steady energy supply [10]. On the other hand, micro-capacitors could serve as a stabilizer for MB's output (power supply) in applications that require consistent power delivery to smooth out fluctuations in voltage and current. Coupled with a Li-ion battery in a smartphone or a Li-ion micro-battery within a miniaturized connected object, a 30% gain in (micro-) battery life is expected [41]. Note that surface-mount capacitors (SMDs) are too bulky to cope with this need for miniaturization.

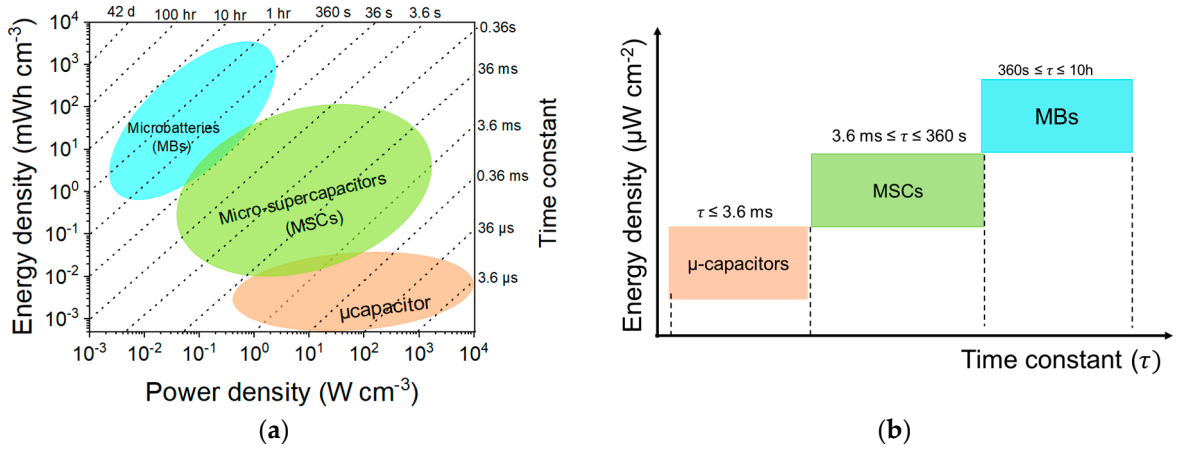

Figure 1. Performance of energy storage microdevices. (**a**) Ragone plot relating energy and power density for the micro-energy storage devices. (**b**) Energy versus time constant of the various energy storage microdevices.

On the other hand, MSCs are miniaturized electrochemical capacitors that operate on the same principles as traditional supercapacitors; they offer higher capacitance and energy density but lower power density, rapid charge/discharge rates, and a longer cycle life compared with electrostatic (micro-/nano-) capacitors [42,43]. MSCs are a bridge between devices operating with short charge–discharge times (<0.1 s) and those with longer discharge times (>0.1 h) under and over which electrostatic (micro-/nano-) capacitors and microbatteries, respectively, find their niche [44]. The Ragone plot relates the energy density (E) and power density (P) for the micro-energy storage devices, using the numerical values to allow a performance comparison exhibited by different devices. The performance requirement of MSC depends on the intended applications. Nevertheless, it is important to take into account the collective fabrication of MSC at the wafer level and subsequently process compatibility with micro-/nanoelectromechanical systems (MEMS/NEMS) technology instead of lab prototyping in order to facilitate the technological readiness level of such MSC [6].

The material selection process is crucial to enhancing energy storage performance, especially for on-chip integration, considering factors such as energy density, power requirements, form factor requirements, and microfabrication techniques. Additionally, the properties of the functional capacitive materials (e.g., specific capacitance) are the main drivers of the energy and power densities of a capacitor (whether electrostatic or elec-

trochemical). The energy stored (E) in a capacitor and the rate at which it delivers the energy (i.e., charge/discharge rates; power density) are important performance metrics; the energy is expressed as a function of both the capacitance (C) and the cell voltage (V) (Equation (1)) [40,45].

$$E = \frac{1}{2}CV^2 \quad (1)$$

Another important performance metric to evaluate the charge/discharge rates of energy storage devices is the time constant (τ), which is the time required for the capacitor to charge/discharge in response to a step change in voltage [46,47]. The time constant is highly influenced by the material properties and is often determined to identify the materials that are capable of retaining high capacity at high charge/discharge rates by providing insights into the device's response time. It is calculated as the product of the equivalent series resistance (ESR) and capacitance (C), as expressed in Equation (2).

$$\tau = R_{ESR} \cdot C \quad (2)$$

Materials that are capable of retaining high capacity at high charge/discharge rates typically exhibit low ESR and high capacitance [48]. Low ESR minimizes energy losses and heat generation during charge/discharge cycles, while high capacitance gives rise to storing more amounts of energy. The relationship between the various devices' energy and time constants is shown in Figure 1b. However, the overall performance of MSCs, for instance, is influenced by two main factors [47]—the choice of the active electrode materials, which define the capacitance of the device, and the electrolyte, which determines the operational voltage. When evaluating electrode materials (and/or electrolytes) for MSCs, it is essential to consider their properties, such as electrical conductivity, surface area, pore structure, and ion transport kinetics [47,48].

Materials with high electrical conductivity and a large surface area can facilitate rapid electron/ion transfer and, in return, faster charge/discharge rates. Also, materials with efficient ion transport properties enable swift diffusion of ions within the electrode/electrolyte interface, which enhances the device's overall performance. The trade-off between the energy and the time constant ($\tau = RC$) of the device is essential for practical applications; to achieve a significant increase in power capability, for instance, a substantial energy reduction may be necessary as a sacrifice in order to get a commensurate reduction in the time constant [47–53].

Moreover, realizing miniaturized on-chip electronic energy storage devices requires meticulous functional material design and deposition techniques compatible with advanced microfabrication processes. Most electrode preparation methods employed in traditional macro-energy storage devices cannot satisfy the requirements imposed by the miniaturization process. In addition, many of the recent electrode preparation techniques for the development of flexible microdevices for printable electronics largely rely on wet processing routes by using colloidal solutions or suspensions of particles, which are not fully compatible with semiconductor device manufacturing usually encountered in the electronics industry [54–56]. Nevertheless, developing various functional material layers may involve more than one growth mechanism and micro-processing techniques. The commonly used electrode film deposition and device microfabrication techniques are shown in Figure 2. The microfabrication process may further be classified as top-down etching techniques, bottom-up printing techniques; and emerging microfabrication techniques, the details on these techniques can be found in the literature [6,11,57,58]. Thin film deposition of functional materials compatible with MEMS/NEMS technology is prioritized to speed up the technological readiness level of efficient on-chip micro-energy storage devices by collective fabrication at the wafer level. Vacuum deposition techniques, such as physical vapor deposition (PVD) and atomic layer deposition (ALD), are favored for this task and are commonly employed in the electronics industry. Although other techniques, especially solution-based routes such as electrophoretic deposition/electrodeposition (Figure 2), have been used to produce high-performance porous electrode materials or high-k dielectric

materials for on-chip energy storage applications—such deposition techniques are instead suitable for lab prototyping [6,59].

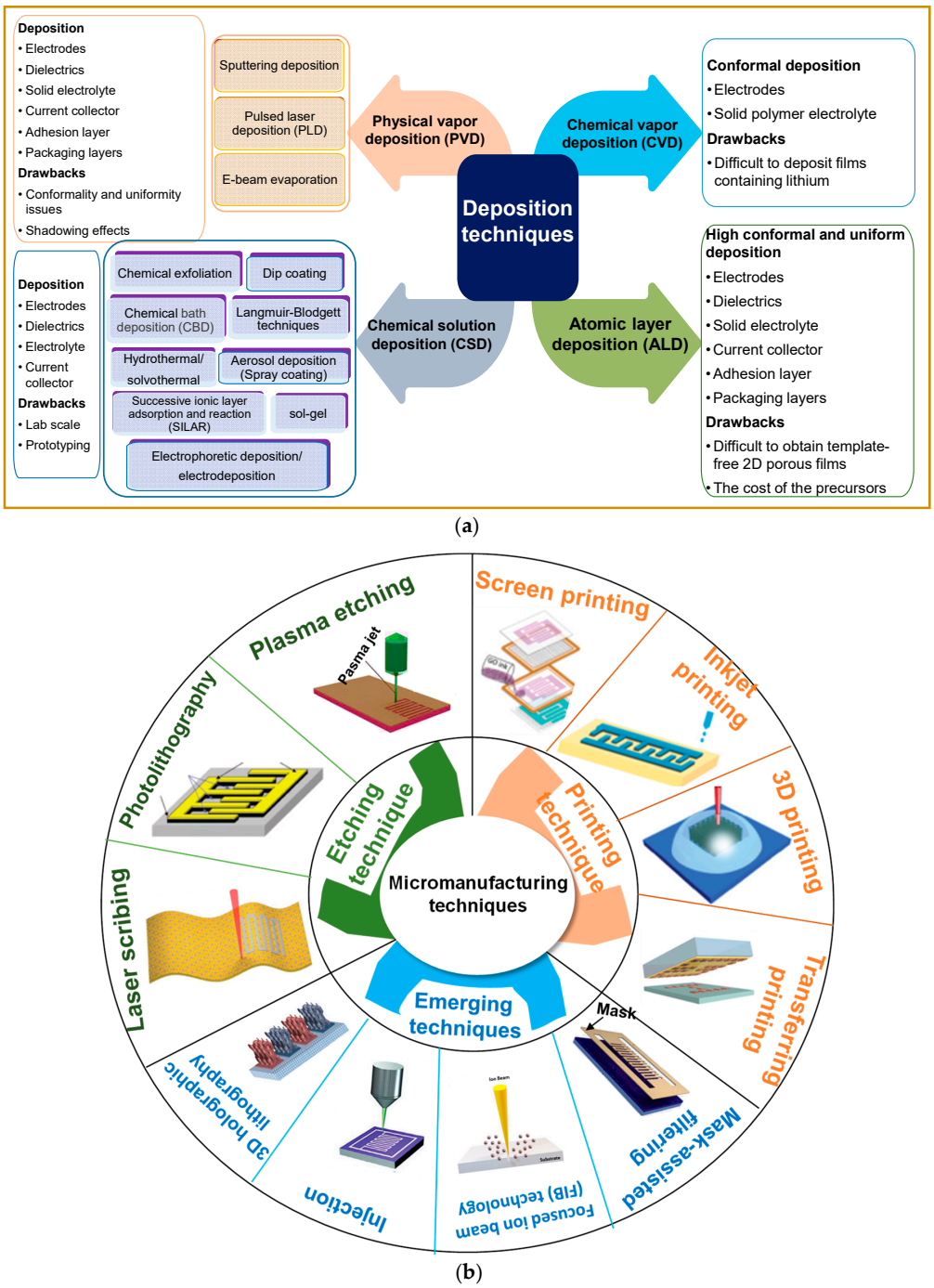

Figure 2. Microfabrication of functional materials for on-chip energy storage microdevices. (**a**) Thin film deposition techniques for electrode materials. (**b**) Microfabrication techniques for on-chip electronics energy storage systems. Laser scribing, photolithography, screen printing, inkjet printing, injection, and transferring printing. Reproduced with permission from [11]. © IOP Publishing Ltd. CC BY 3.0. 3D printing. Reproduced with permission from [60]. Copyright (2016), American Chemical Society. Focused ion beam (FIB) technology. Reproduced with permission from [61]. © MDPI. CC BY 4.0. 3D holographic lithography. Reproduced with permission from [12]. Copyright (2022), Elsevier. Mask-assisted filtering and plasma etching. Reproduced with permission from [17]. Copyright (2020), John Wiley & Sons.

It is also essential to consider the selection of a suitable substrate for film development to accommodate different electrode microfabrication techniques. The substrate provides mechanical support to the functional materials, facilitating electron transport and influencing the device's performance in certain extreme conditions. Substrates are usually classified as rigid (Si, Si/SiO_2, glass, and quartz) and flexible (polyethylene terephthalate, polyimide, polyvinyl alcohol, polydimethylsiloxane, paper, and textile) [62,63]. However, silicon wafers are highly versatile substrates compatible with various semiconductor fabrication processes and technologies. They provide a reliable foundation for implementing various semiconductor technologies and are widely adopted across different segments of the electronics industry. Their uniformity, purity, scalability, and compatibility with semiconductor manufacturing processes make them indispensable in producing advanced electronic components that power modern technology. Several reviews have been conducted on on-chip energy storage devices, focusing more on design, fabrication, integration, applications, and performance metrics. This review provides an overview of capacitive materials for on-chip electrostatic (micro-/nano-) capacitors and electrochemical MSCs, with more emphasis on recent electrode developments, challenges, and future directions. Emphasis is given to the electrode materials, and the preparations are largely compatible with MEMS technology.

2. Materials for Electrostatic (Nano-/Micro-) Capacitors

Electrostatic capacitors are energy storage devices typically consisting of two closely spaced parallel conducting electrodes separated by an insulating material known as a dielectric (see Figure 3) [64]. The configuration is designated as metal–insulator–metal (MIM). The device obeys Coulomb's law when a voltage (V) bias is applied to the electrodes; it initiates a polarization of the dielectric by the applied electric field, resulting in a charge accumulation on opposing electrode surfaces; this is known as the electrostatic charge storage process [65–67]. Capacitance (C) is the most important performance metric for a capacitor, as it determines its capability to store charge.

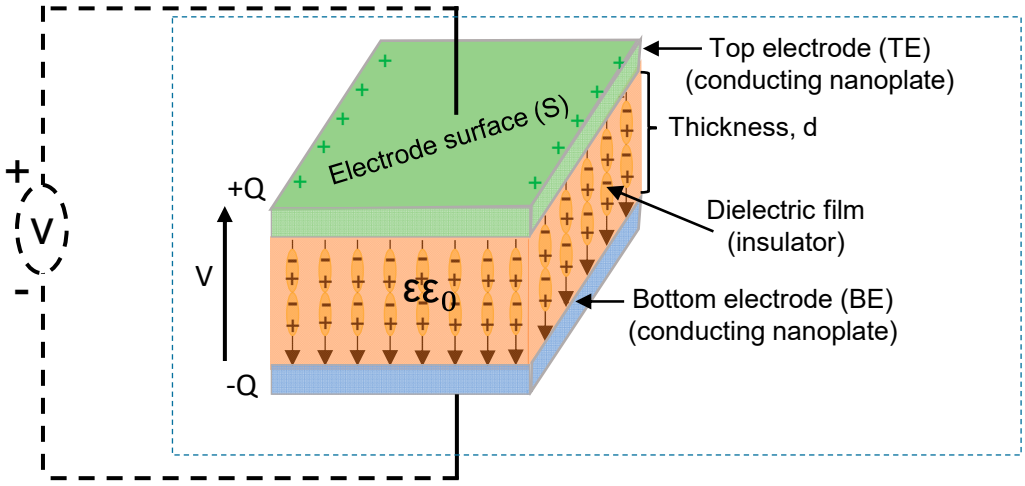

Figure 3. Schematic diagram of a typical electrostatic (micro-) capacitor.

The ratio of the total accumulated charge (Q) and the electric potential (V) is used to express capacitance, which can be calculated using the following formula:

$$C = \frac{Q}{V} \tag{3}$$

$$Q = C \cdot V \tag{4}$$

The ability of a dielectric material to hold or store charge is an important intrinsic property known as dielectric permittivity (ε). However, in the absence of the dielectric, the

space between the electrodes becomes empty; the ε is replaced by the permittivity of the free space or vacuum, ε_0, a constant that is approximately equal to 8.854×10^{-12} Fm^{-1}. The capacitance further defines the relationship between the surface area (S) of the electrodes, the distance (d) between the electrodes, and the dielectric permittivity (ε), as given in Equation (5). In order to measure how effectively the dielectric can store energy in an electric field relative to a vacuum, another parameter, known as relative permittivity or dielectric constant, κ, is introduced, as shown in Equation (6).

$$C = \varepsilon(S/d) \tag{5}$$

$$C = \kappa\varepsilon_0(S/d) \tag{6}$$

where $\kappa = \varepsilon_r = \frac{\varepsilon}{\varepsilon_0}$.

A distinctive feature of electrostatic capacitors is their high power due to their rapid charge/discharge rates, with the rates limited only by external circuit RCs. However, energy storage is limited as only a flat surface or parallel plate electrode configuration is utilized, unlike MSCs, where charges are stored in electric double layers or through fast redox reactions in porous electrodes, allowing larger energy density storage on the porous electrode surfaces [67]. The energy (E) is an important performance metric, which is a function of both the capacitance (C) and the voltage (V), i.e., $E = \frac{1}{2}CV^2$ (Equation (1)), derived from $dE = VdQ$ [40]. Materials with a higher dielectric constant (known as high-k) and/or increased surface area of the electrodes can enhance charge storage, thus increasing the energy density. Applying a higher voltage can also increase the energy while taking the breakdown voltage of the dielectric material into account. However, it is noteworthy that other factors like polarization and applied electric field also play a significant role in determining the capacitor's energy performance, which is detailed elsewhere [40,68,69].

Miniaturization of the capacitors can compromise their performance/efficiency as the size is significantly reduced along the footprint of the electrodes, leading to capacitance loss [70] To compensate for the loss of capacitance, the thickness of the dielectric films (d) needs to be reduced. Having an extremely thin dielectric can result in leakage current from direct electronic tunneling through the dielectric, leading to a complete breakdown of the dielectric when the leakage current becomes too high at a certain electric field E_{bd} [70,71]. The voltage at which the dielectric materials experience breakdown is known as breakdown voltage (V_{bd}) and is expressed as:

$$V_{bd} = E_{bd} \cdot d \tag{7}$$

$$E_{bd} = \frac{V_{bd}}{d} \tag{8}$$

where E_{bd} is known as the dielectric breakdown strength (DBS).

There is a trade-off between dielectric constant (k) and breakdown voltage (E_{bd}) when achieving high capacitance and voltage due to thickness, as expressed below [71,72]

$$E_{bd}\ (\text{orDBS}) \sim \frac{20}{\sqrt{\kappa}}\left[\text{MV cm}^{-1}\right] \tag{9}$$

Hence, electrostatic capacitors are typically metal–insulator–metal (MIM) and designed to be integrated directly onto silicon substrates alongside other electronic components, enabling highly integrated systems-on-chip (SoCs). Physical vapor deposition (PVD) techniques such as sputtering deposition are popular in the electronics industry and can be used to deposit dielectric and electrode materials on top of the silicon substrate, but the issues of film conformality and uniformity limit these deposition techniques for 3D silicon-integrated capacitors [73–75]. A 3D nanostructured electrode configuration is introduced to achieve a higher surface area and, thus, a higher capacitance value. Hence, realizing extremely high aspect ratio structures such as deep reactive ion etched (DRIE) silicon [64] and anodized aluminum oxide (AAO) [67], electrostatic silicon-integrated capacitors are typically fabricated using semiconductor microfabrication techniques, including

photolithography, etching, and deposition processes, particularly atomic layer deposition (ALD) (Figure 1). These microfabrication techniques ensure precise control over capacitor dimensions, dielectric materials, and electrode configurations.

The ALD technique is usually preferred due to its unique features for fabricating ultrathin films, nano-laminating layers, high degree of thickness control, and conformal surface coatings in high-aspect-ratio trenches [67,70]. The ALD technique has shown significant improvements in the areal capacitance of nearly 1 μF mm^{-2} [64,67,71]. However, some dielectric films prepared by ALD exhibit a low dielectric constant due to the low deposition temperature, inhibiting a high degree of crystallization [70,76]. Extensive screening and exploration of various high-k dielectric materials to increase the capacitance and energy density of silicon-integrated capacitors while maintaining a good breakdown voltage are on the radar of the researchers. The commonly used dielectrics are shown in Figure 4, featuring their bandgap versus the dielectric constant. It is essential that the k-value be high, over 12 or preferably 25–35, while the high bandgap is required to suppress leakage current [77,78]. There is a critical trade-off relationship between high-k dielectrics and bandgap that needs to be taken into account; when the dielectric constant is increased, the band gap is decreased [78]. As the dielectric constant increased, the conduction band offsets (i.e., the barrier height) between the metal electrode and dielectric decreased, leading to a decrease in dielectric strength [78]. The phase of the dielectric materials with a uniform crystal structure is expected to remain unchanged in the temperature range of operation to prevent grain boundaries and crystal dislocations favoring carrier recombination and potential leakage paths [70].

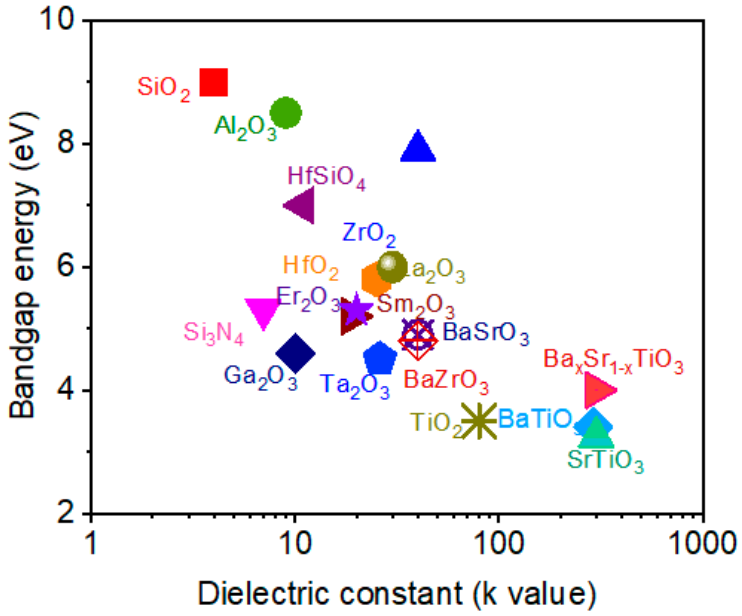

Figure 4. Band gap versus dielectric constant of dielectric materials.

The summary of the emerging dielectric materials is given in Table 1. SiO_2 deposited on Si wafers is the most commonly used substrate, suitable for on-chip capacitors; however, other types of substrates have been reported. The same electrodes are traditionally used for both bottom and top electrodes in a symmetric configuration, even though some may prefer to use different materials with high work functions to suppress leakage current. Nonetheless, the performance of micro-capacitors mainly depends on the dielectric material [79]. The electrode materials commonly used are usually the participating metals in the oxide dielectric compounds; other electrode materials with higher work functions, including Ni, Al, Pt, Ag, Au, Cu, TiN, and TaN, may be used to minimize the leakage current [79–82].

2.1. Binary Oxide Dielectric Materials

Al_2O_3, Si_3N_4 (nitride dielectric), and SiO_2 exhibit good dielectric breakdown strength but suffer low dielectric constants. Efforts have been made to explore several high-k dielectric materials, such as HfO_2 [83], Sm_2O_3 [84], Er_2O_3 [85], Ta_2O_5 [82,86], ZrO_2 [87–89], and La_2O_3 [90,91]. However, the low breakdown field of these high-k insulators is a major concern for capacitor reliability [92]. To address the low breakdown field and improve leakage performance, binary oxide dielectrics are usually stacked. Examples are the high-k nanolaminated MIM capacitors [93–95]. The preparation of the stacked oxide dielectrics is usually carried out via vacuum deposition techniques such as sputtering, PLD, and ALD. Yu et al. [96] fabricated planar MIM capacitors with HfO_2-Al_2O_3 laminate dielectric on SiO_2 substrate using the ALD technique, demonstrating a capacitance density of 12.8 fF μm^{-2} from 10 kHz up to 20 GHz and a low leakage current of 3.2 $\times$ 10^{-8} A cm^{-2} at 3.3 V. Si_3N_4/laminated Al_2O_3–HfO_2 was fabricated using back-end-of-line (BEOL) fabrication to demonstrate a capacitance density of 4.2 fFμm^{-2} [92]. Other stacked dielectrics have also been reported, including $ZrO_2/Ta_2O_5/ZrO_2$ [97], $HfO_2/Ta_2O_5/HfO_2$ [97,98], $Al_2O_3/TiO_2/HfO_2$ [99], and $Al_2O_3/HfO_2/Al_2O_3$ [100]. Films have been exploited for the MIM capacitors to increase the capacitance density. In addition, the breakdown field can also be improved through doping, as reported for $Hf_xZr_{1-x}O_2$ thin films fabricated by the atomic layer deposition (ALD) technique on SiO_2/Si substrate [101,102].

Table 1. Emerging dielectrics for micro-capacitors.

Dielectric	Thickness (nm)	Preparation Technique	Breakdown Voltage ($MVcm^{-1}$)	ESD (Jcm^{-3})	Reference
Al_2O_3	25	ALD	4.8	-	[67]
BT-BMZ	230	Sputtering	7.9	87.26	[73]
BSMT	280	Sputtering	3	91	[75]
BZT	130	Sputtering	4.56	40.6	[37]
Sm-BFO-BTO	650	PLD	3.5	152	[103]
BFO25-BTO75-2.5Mn	200	PLD	3	80	[104]
BST–BMN	400	PLD	5	86	[105]
BZT	60	PLD	6.5	65.1	[106]
BZT	90	PLD	7.94	89.9	[74]
La:HZO	10	ALD	4	50	[102]
Si:HfO_2	9	ALD	3.3	40	[107]
Si:HZO	10	ALD	4.5	53	[108]
Al:HZO	10	ALD	5	52	[108]
HZO/$Hf_{0.25}Zr_{0.75}O_2$	1/9	ALD	6	71.97	[109]
TZT	8	ALD	5.38	114.5	[110]
HfO_2/ZrO_2	2.2/6.6	ALD	4	49.9	[111]

ESD = electrostatic discharge, PLD = pulsed laser deposition; ALD = atomic layer deposition, BST = barium strontium titanate; BT-BMZ = 0.85$BaTiO_3$-0.15$Bi(Mg_{0.5}Zr_{0.5})O_3$, BSMT = $Ba_{0.5}Sr_{0.5}(Ti_{0.97}Mn_{0.03})O_3$, BZT = $BaZr_{0.35}Ti_{0.65}O_3$, HZO = $Hf_{0.5}Zr_{0.5}O_2$, TZT = $TiO_2/ZrO_2/TiO_2$.

The use of highly regular three-dimensional (3D) architecture has been exploited and demonstrated both high energy and high-power density [67,112]. For instance, Banerjee et al. [67] fabricated 3D arrays of MIM nanocapacitors in self-assembly and self-aligning anodic aluminum oxide nanopores via ALD, employing TiN as the conducting electrodes and Al_2O_3 as the insulator (Figure 5). It was demonstrated that the conformality for the bottom electrode TiN and Al_2O_3 in a 20:1 aspect ratio pore was better than 95%. The SEM images show the nanotubular MIM structure, indicating the AAO barrier layer and three layers corresponding to the TiN bottom electrode (BE), Al_2O_3, and TiN top electrode (TE), and wafer-based production showing capacitors of different areas, with each dot capacitor being 125 µm wide and comprising about 10^6 nanocapacitors (or nanotubes). The nanocapacitors achieved an enhanced 100 µF cm^{-2}, substantially exceeding previously reported values for nanostructured electrostatic capacitors [67]. In another study,

Hourdakis et al. [113] fabricated 3D structured MIM capacitors using photolithography and plasma etching, HfO_2 dielectric was deposited via ALD, and the device achieved 3.2 μF cm^{-2} with stable operation up to a frequency of 10^5 Hz.

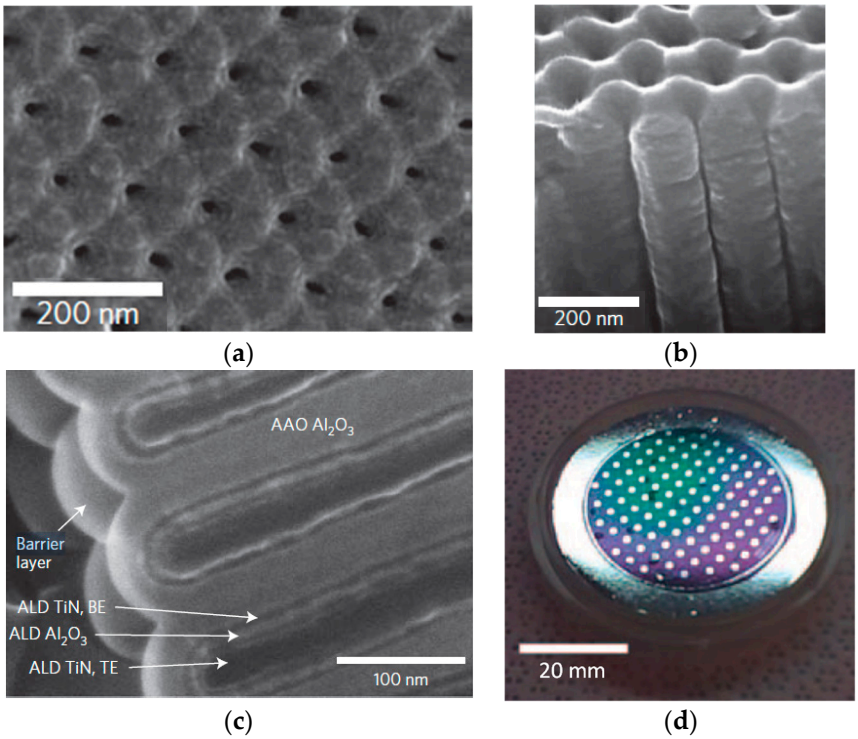

Figure 5. MIM nanocapacitor. (**a**,**b**) SEM plan-view and cross-section of an AAO MIM structure. (**c**) The bottom of the tube, showing the AAO barrier layer and three layers corresponding to the TiN bottom electrode (BE), Al_2O_3 and the TiN top electrode (TE). (**d**) Two-inch wafer with nanocapacitors. Reproduced with permission from [67]. Copyright (2009), Springer Nature.

2.2. Ternary Oxide Dielectric Materials

As the efforts to improve the performance of the dielectric capacitors intensified, ternary oxide dielectric materials with perovskite crystal structure, especially class II ceramic capacitor materials such as barium titanate ($BaTiO_3$, BTO), strontium titanate ($SrTiO_3$, STO), bismuth ferrite ($BiFeO_3$, BFO), silver niobate ($AgNbO_3$, ANO) [114], $BaZrO_3$, $SrTiO_3$, $SrRuO_3$ [115], and $LaGdO_3$ [116], are considered to be very promising due to the exceptionally high permittivity (>1000) obtainable in the perovskite crystal structure [78]. The permittivity of the materials can be extensively modified to vary the material composition, which could lead to different polar structures of perovskite dielectrics, resulting in the formation of linear dielectrics, ferroelectrics, relaxor-ferroelectrics, and anti-ferroelectrics [117]. However, the MIM capacitor-based on perovskite dielectrics also suffers from severe leakage current problems due to the trade-off relationship between the dielectric constant and bandgap; the main reason for severe leakage current problems is because of their narrow bandgaps [77,78,117–119]. Like binary compounds via dielectric stacking, doping, or elemental substitution [120]. The breakdown voltage of the perovskite materials could be significantly improved when their A-site or B-site are fully or partly substituted or are found in stacked systems [68,79]. Unfortunately, many substitutions are carried out via solution-based processes, which are not suitable for the on-chip microfabrication protocols. Nevertheless, some of the derivatives from the substitution/doping of BTO have been obtained via PLD, including La-doped $Ba_{1-x}La_x(Zr_{0.25}Ti_{0.75})O_3$ (BLZT) [74,121] and Mn-doped $BiFeO_3$–$BaTiO_3$ thin films [105], $BiFeO_3$-$BaTiO_3$-$SrTiO_3$(0.55 − x)BFO−xBTO-0.45STO) were also realized by PLD, exhibiting high energy density with a low leakage voltage [73].

3. Materials for Micro-Supercapacitors

For convenience, it is often necessary to classify electrochemical micro-supercapacitors (MSCs) into two according to the charge storage mechanisms, namely, miniaturized electric double-layer capacitors (EDLCs) and pseudo(micro-) capacitors [6,45]. It is also important to discuss the mechanisms for the charge storage process in MSCs in terms of EDLC and pseudo-capacitance separately. Miniaturized EDLCs store charges principally on the adsorption/desorption (physisorption) of ions on the electrode surface, particularly carbon-based materials, where under an electric field, the charge carriers become polarized and accumulate on the parallel porous electrode surfaces to form electrochemical double layers (EDL); the physisorption is very fast and reversible, and they usually operate in an organic electrolyte or ionic liquid [45,122].

In contrast, the charge storage processes in pseudo(micro-) capacitors utilize non-polarized electrodes (known as pseudocapacitive electrodes) that operate based on chemical potential, undergoing fast reversible Faradic reactions at the surface or subsurface, thereby facilitating high power capabilities [12,66,122]. MSCs are distinctly different from microbatteries (MBs) that exhibit an in-depth and relatively sluggish bulky redox reaction mechanism involving Li-ions shuttling between the cathode and anode; MBs, unlike pseudo(micro-) capacitors, exhibit higher energy density but lower power density, poor rate capability, and a shorter lifespan [25,123–127].

MSCs are known for power delivery, capable of operating at a high rate but relatively low energy density. Since both energy and power densities are important for IoT applications, their energy delivery needs critical improvement. The energy density (E) of the MSCs can be maximized by either increasing the capacitance and/or the working voltage window, since $E = \frac{1}{2}C \cdot \Delta V_{MSC}^2$, where C is the capacitance and ΔV_{MSC} is the cell voltage [45,128,129]. Both C and V are influenced by the nature or properties of the electrode materials and electrolyte [129]. Besides the electrolytes' influence, increasing the surface area of the electrode films can effectively enhance the capacitance and, thus, energy density. The performance of the MSCs strongly depends on the properties of the electrode materials, such as the crystallographic structure and morphology of the active material (e.g., nanorods, nanowires, nanofeather, and porous nanoflakes), and other factors include electrical contact with current collectors, exposed surface area, amounts of cations, etc. [130,131].

In the meantime, increasing surface capacitance results in a higher time constant, according to this formula, $\tau = RC_{MSC}$, leading to lower power performance, necessitating a trade-off between capacitance and power capabilities [6]. A pertinent strategy consists of lowering the resistance of the electrode materials [53]. In addition, the energy and power densities can also be enhanced through the topology or configuration of the device (the arrangement or geometry of the positive and negative electrodes) [6,132]. The overview of the schematic topologies used in MSCs, including parallel plate, interdigitated, and three dimensional (3D) interdigitated configurations, is shown in Figure 6a. The interdigitated topology is the most suitable configuration for on-chip MSC applications, having both electrodes in the same plane. However, the amount of active material per electrode is reduced by half due to the inactive gap between the two interdigitated electrode fingers. As a result, the surface capacitance decreases drastically to less than one-fourth of the areal capacitance of a single electrode. In order to enhance the energy density of MSCs, 3D interdigitated configurations have been explored. Lethien et al. [6] provide comprehensive details on the different MSC topologies and configurations. Again, the energy storage capacity can be improved through a 3D electrode design that unblocks the "dead surface" of MSC electrodes while maintaining high mass loading within the device's footprint area [6,132,133].

Further, increasing the cell voltage will also substantially enhance the energy to the tune of four-fold, according to Equation (1) [129]. The width of the safe electrochemical window of the electrode material, which defines the cell voltage, needs to be critically considered. Several electrode materials, especially pseudocapacitive materials, exhibit high capacitance in aqueous electrolytes, but their cell voltage is limited to around 1 V due to

the water splitting at 1.23 V. However, the most efficient energy density delivered by these MSCs is around 100 μWh cm^{-2} [6,128]. Nevertheless, the safe electrochemical window can be extended when two different active materials are used in the negative and positive electrodes to have an asymmetric configuration (as shown in Figure 6b), combining the potential windows of both electrodes (i.e., with complementary electrochemical potential windows) without damaging the materials [6,45]. This is a major departure from the symmetric configuration, where the same (pseudo)capacitive material is used in the two electrodes and the cell voltage is restricted to about 1.2 V in the potential window.

Asymmetric MSCs could exhibit up to 2 V cell voltage in aqueous media [134–145]; the cell voltage depends on the positive electrode's upper potential limit and the negative electrode's lower potential limit [146]. The overpotentials at the positive electrode (for oxygen evolution) and the negative electrode (for hydrogen evolution) extend the cell voltage windows beyond the thermodynamic limit of 1.23 V of the water decomposition voltage [146]. An example of asymmetric configuration was demonstrated by Asbani et al. [145] (Figure 6c), combining sputtered vanadium nitride film (VN) and electrodeposited hydrous ruthenium oxide ($hRuO_2$) film to fabricate an asymmetric micro-supercapacitor (A-MSC). Taking advantage of their complementary electrochemical potential windows in 1 M KOH electrolyte to achieve a cell voltage up to 1.15 V and high specific capacitance values for the device (≈100 mF cm^{-2}). The effect of asymmetric configuration is evident in the galvanostatic charge and discharge plots shown in Figure 6c. Concerted efforts have been focused on exploring various active electrode materials, including carbon-based, conducting polymer, and metal-based materials (oxides, nitride, and MXene), to optimize the power and energy delivery of on-chip MSCs. Additionally, there have been attempts to combine battery-type materials with (pseudo) capacitive materials to form hybrid (asymmetric) MSCs, commonly referred to as Li-ion micro-supercapacitors [147–150]. However, these efforts have only been able to obtain prototyping MSCs [147,148]. An example of this was demonstrated by Zheng et al. [8], who fabricated a prototype hybrid MSCs featuring lithium titanate nanospheres and graphene in an MSC asymmetric configuration. Another area of interest is optimizing the existing solid electrolytes and developing new ones for better performance.

MSC performance is evaluated based on the surface area or volume of the device to normalize capacitance (F), energy (Wh), and power (W). The surface performance metrics are given as mF cm^{-2}, mWhcm^{-2}, and mW cm^{-2}, which are normalized by the operated area of the active electrode [6,9,56,151]. Volumetric performance is derived by normalizing the surface metrics to the thickness of the active layer, giving rise to mF cm^{-3}, μWhcm^{-3}, and mW cm^{-3} for capacitance, energy, and power, respectively [56,151]. When comparing the performance of MSCs, volumetric performance metrics are appropriate, but it is important in that case not to take into account the thickness of the substrate, which is only used as a mechanical support in most cases with various thicknesses (from 200 μm up to 2 mm as an example). It is useless to divide the surface performance by this substrate thickness.

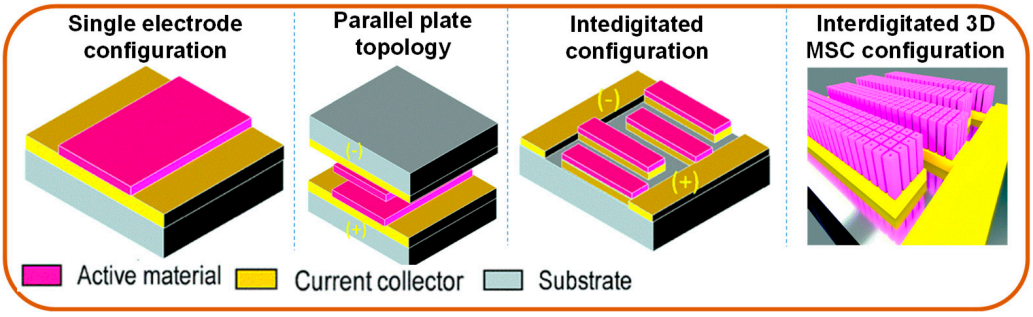

(**a**)

Figure 6. *Cont.*

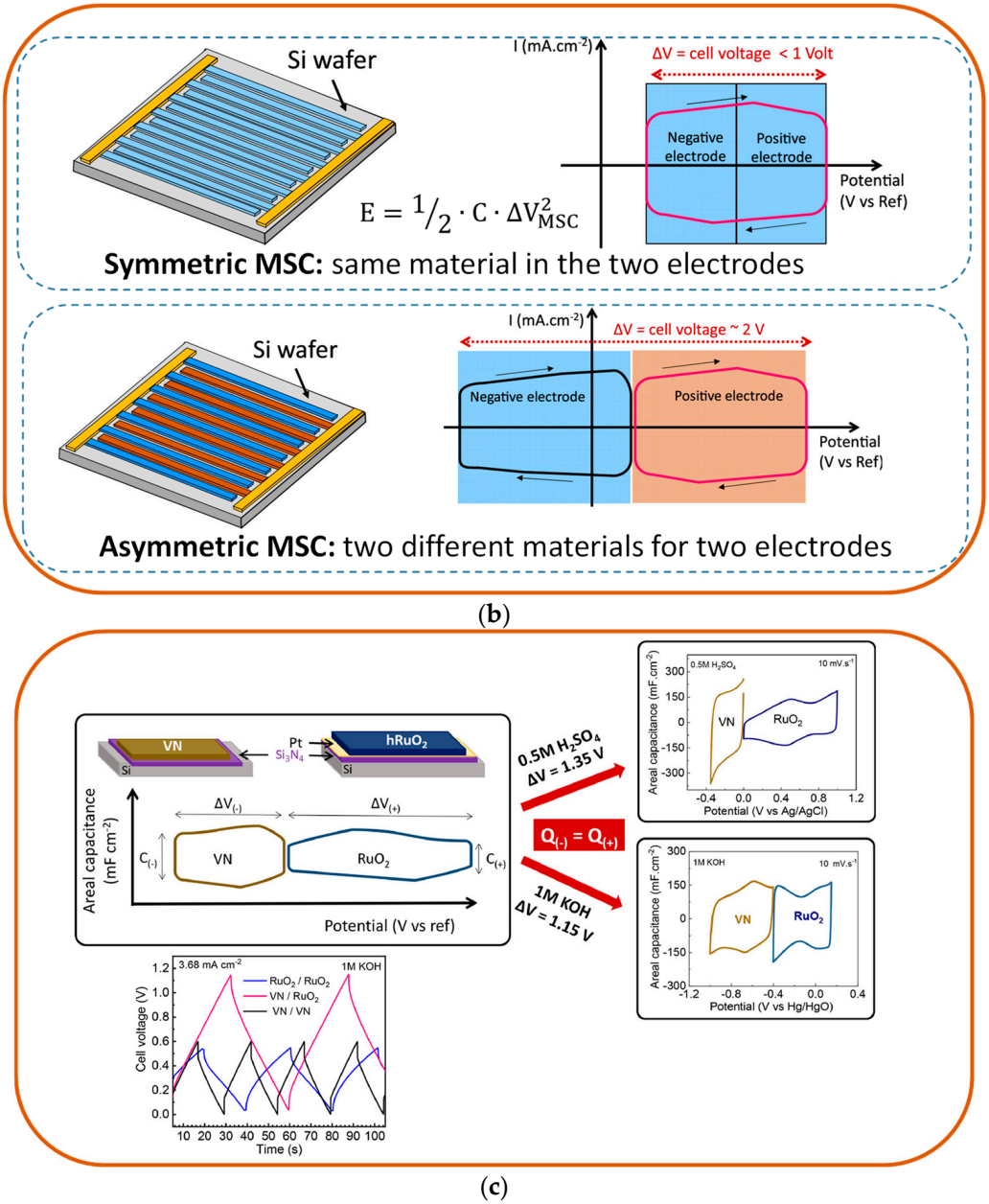

Figure 6. Representative electrode topologies/configurations for on-chip micro-supercapacitors. (**a**) Various electrode configurations. Reproduced with permission from [6]. Copyright (2019), Royal Society of Chemistry. (**b**) MSC based on interdigitated topologies with a symmetric configuration or an asymmetric configuration. Reproduced with permission from [45]. © American Chemical Society. CC BY 4.0. (**c**) Sketch up of the VN/$hRuO_2$ asymmetric MSC in face-to-face topology operating in 0.5 M H_2SO_4 and 1 M KOH aqueous electrolytes, and galvanostatic charge and discharge plots of the symmetric and asymmetric MSCs, using $hRuO_2$ as the positive and VN as the negative electrodes, respectively. Reproduced with permission from [145]. Copyright (2021), Elsevier.

This metric is also used by many researchers to exacerbate the performance of nanometer-thick film electrodes. In that case, the volumetric energy and power densities are exaggerated, and that does not reflect the real performance of the MSC. The most important thing for a microdevice is the footprint surface of the energy storage source, which is constrained by the miniaturization of the electronics. It is thus reasonable to evaluate the performance of the MSC based on the surface metric since the footprint area is

a crucial factor to consider in on-chip applications [9,56,151]. The performance of the MSCs could be influenced by the following parameters:

- MSC topology
- Capacitance retention of the MSC
- Material/electrolyte conductivity
- Material surface area
- Material/electrolyte ion transport properties.
- Mass-loading of the active materials
- The width of the safe electrochemical window

3.1. Electric Double-Layer Capacitor Materials

Electric double-layer capacitor (EDLC) materials are low-cost porous carbon-based electrodes, such as carbon nanotubes [152–154], activated carbons [155], carbide-derived carbons (CDC) [44,156,157], onion-like carbon [158], carbon foam [159], and graphene [160]. They exhibit a high specific surface area, good electrical conductivity, and chemical stability. They are usually operated in organic electrolytes, demonstrating true capacitive behavior and excellent chemical stability upon cycling [6,36,44,54,155,156,159,161,162]. However, carbon-based MSCs suffer from low energy density, limiting their practical applications in high energy microdevices [159]. To improve the energy performance, carbon-based materials are usually composited/doped with other (pseudo)capacitive materials. Table 2 provides a summary of the recently researched carbon-based MSCs electrodes for on-chip applications.

3.1.1. Graphene-Based Materials

Graphene-based materials are the most explored carbon-based electrodes for MSCs applications. They exhibit excellent electrical properties due to their high electron mobility (2.5×10^5 cm^2 V^{-1} s^{-1}) at room temperature [163]. They also possess a large theoretical surface area (2630 m^2g^{-1}) [43] and have the capability to offer ultrahigh power performance and excellent frequency response [160,164]. Graphene is a single layer of sp^2-hybridized carbon atoms tightly bound in a two-dimensional (2D) honeycomb lattice with monoatomic layer thickness [151]; the intrinsic capacitance of single-layer graphene (SLG) of ~21 μF cm^{-2} sets the upper limit for EDL capacitance for all carbon-based materials [165–167]. They are typically synthesized by the chemical vapor deposition (CVD) method under a high temperature and with a catalytic metal substrate (mostly grown on copper or nickel foam), requiring transfer to a final substrate; the processing conditions, restacking due to the van der Waals interaction between platelets [168–170], and low throughput limit their widespread application in in-plane (on-chip) MSCs [167,171]. Therefore, other synthesis routes are being explored, including solution-processing techniques (especially the liquid-phase exfoliation method), reduction in graphene oxides (GO) [168], and laser induction.

Reduced GO (rGO) constitutes the majority of the reported graphene-based MSCs electrodes. They are obtained by removing the oxygen-containing functional groups from graphene oxides (GO) through various methods such as laser, thermal, chemical, or ultraviolet irradiation; however, the chemical reduction method is the most widely used [172–174] Generally, GO is a highly resistive material; hence, its electrical conductivity needs to be improved to meet the requirements of MSC applications, while on the other hand, rGO is a conducting material that is very close to pure graphene. For instance, Wu et al. [168] used the methane-plasma reduction technique to obtain rGO on Si substrate, followed by oxygen-plasma etching for interdigitated patterning of the film. The MSCs delivered low capacitance values (80.7 μF cm^{-2}/17.9 F cm^{-3}) with power and energy densities of 495 W cm^{-3} and 2.5 mWh cm^{-3}, respectively, showing how maximizing volumetric performance while surface energy and power densities are very low. However, some of the conversion methods involve wet processing routes that could be detrimental to the microfabrication protocols, thereby impeding their implementation in on-chip MSC

applications [170]. Additionally, many of the reduction processes, such as high temperature, plasma, or reductant treatment, are not suitable for scalable and on-chip MSC integrated applications [170].

Exfoliated Graphene

Exfoliated graphene (EG) is typically in powder form and is prepared through a process called liquid-phase exfoliation. To make an ink or slurry, it is dispersed in a solvent along with other additives such as surfactants, stabilizers, binders, and conductive agents. The resulting mixture can be deposited onto substrates or current collectors using microfabrication techniques (see Figure 2b) such as screen printing [175,176], mask-assisted filtration [177,178], inkjet printing [179], electrophoretic deposition [180], spray coating [181,182], or electrodeposition [181,182]. Additionally, EG can be combined with other electroactive materials like transition metal oxides and conducting polymers to create composite materials [151,183,184].

Table 2. EDLC materials for on-chip MSCs.

Electrode Material	Substrate	Synthesis/Fabrication	Thickness	Electrolyte	Cell Voltage/ Pot. Window	Areal Cap.	Vol. Cap.	Energy Density	Power Density	Configuration	Reference
			nm		V	$mFcm^{-2}$	Fcm^{-3}	$mWhcm^{-3}$	Wcm^{-3}		
Graphene	PET	CVD/DLW	17	PVA-H_2SO_4 hydrogel	1	0.063	36.8	5.1	1714	Intedigitated	[170]
Graphene	PET	CVD/DLW	17	EMITFSI/Fumed silica ionogel	2.5	0.045	147	23	1860	Intedigitated	[107]
Graphene	Si/SiO_2	CVD/Lithography	5	PVA-H_2SO_4 hydrogel	1	0.066	131	NA	NA	Intedigitated	[185]
Graphene	Glass/Ni	Drop casting/plasma etching	1000	PVA-H_2SO_4 hydrogel	0.8	0.1	20	1.5	2000	Intedigitated	[186]
Graphene	Si/SiO_2	CVD/Plasma etching	5	PVA-H_2SO_4 hydrogel	1	0.2	307	42.6	2000	Intedigitated	[187]
Graphene	Si/SiO_2 and PET	Spin coating/Inkjet printing	750	PSSH	1	0.7	9.3	1.3	0.6	Intedigitated	[187]
Graphene (Exfoliated)	PET	Electrochemical exfoliation/ Mask-assisted filtration	600	PVA-H_2SO_4 hydrogel	1.2	0.822	13.7	2.74	493	Intedigitated	[188]
Graphene (Exfoliated)	PET	Electrochemical exfoliation/ Mask-assisted filtration	600	KTFSI-P14TFSI ionogel	3.4	0.54	9.03	14.5	2.6	Intedigitated	[188]
Graphene	Polyimide	Laser scribing	25,000	H_2SO_4	1	4	1.6	0.4	50	Intedigitated	[189]
rGO	Polyimide	Mask-assisted vacuum filtration	1020	PVA-H_3PO_4 hydrogel	0.8	0.6845	6.7	0.37	5	Intedigitated	[190]
rGO	PET	Spin-coating/lithography	15	PVA-H_2SO_4 hydrogel	1	0.08	17.9	2.5	495	Intedigitated	[168]
rGO	Si/SiO_2	Spin coating/Laser scribing	7600	EMITFSI/Fumed silica ionogel	2.5	2.32	2.32	2.1	200	Intedigitated	[160]
rGO-CNTs	Si/SiO_2/TiAu	Electrostatic spray deposition (ESD)/photolithography	6000	3 M KCl	1	5.6	4.9	0.68	77	Intedigitated	[164]
Graphene-CNTs	PET	Wet-Jet Milling Exfoliation/ screen printing	27,000	PVA-H_3PO_4 hydrogel	1.8	1.32	0.49	0.22	<1	Intedigitated	[191]
CNTs		3D Printing	27,600	PVA-H_3PO_4 hydrogel	1	4.69	1.7	0.12	3.72	Intedigitated	[152]
CNTs	Si/SiO_2	Injection/Plasma etching	5000	PVA-H_3PO_4 hydrogel	0.8	2.75	5.5	0.4	0.19	Intedigitated	[153]
CNTs	Si/SiO_2/Fe	Plasma enhanced CVD		PVA–KCl hydrogel	0.8	5	2.5	-	-	Single electrode	[192]
CNTs-carbon nanosheet (CN)	Si/SiO_2	CVD/photolithography	100,000	PVA-H_3PO_4 hydrogel	1	110	11	2	0.45	Intedigitated	[193]

Table 2. *Cont.*

Electrode Material	Substrate	Synthesis/Fabrication	Thickness	Electrolyte	Cell Voltage/ Pot. Window	Areal Cap.	Vol. Cap.	Energy Density	Power Density	Configuration	Reference
			nm		V	$mFcm^{-2}$	Fcm^{-3}	$mWhcm^{-3}$	Wcm^{-3}		
Carbon nanowires (CNWs)	$Si/Si_3N_4/Cr/Pt$	Electrodeposition + CVD/ direct laser writing	12,000	PVA-H_3PO_4-SiWA	0.8	5.7	4.75	NA	NA	Single electrode	[194]
Activated carbon	Si/SiO_2	Photolithography/etching process/inkjet printing	20,000	1 M Et_4NBF_4	2.5	2.1	-	-	-	Intedigitated	[155]
TiC-CDC	Si/SiO_2	DC magnetron sputtering + Chlorintion	1400	1 M H_2SO_4	0.9	49	350	10.1	2	Intedigitated	[54]
TiC-CDC	Si/SiO_2	DC magnetron sputtering + Chlorintion	4100	2 M EMI, BF_4:CH_3CN	3	61.5	150	35	1	parallel plates	[54]
TiC-CDC	Si/SiO_2	DC magnetron sputtering + Chlorintion	2200	2 M EMI, BF_4:CH_3CN	3	35.2	160	30	10	parallel plates	[54]
TiC-CDC	Si/SiO_2	DC magnetron sputtering + Chlorination	5000	1 M H_2SO_4	0.8	205	410	NA	NA	Single electrode	[54]
TiC-CDC	Si/SiO_2	DC magnetron sputtering + Chlorination	3200	1 M H_2SO_4	0.9	112	350	39	0.94	parallel plates	[161]
TiC-CDC	Si/SiO_2	DC magnetron sputtering + Chlorination	4600	1 M KOH	1.1	71	152	NA	NA	Single electrode	[156]
TiC-CDC-Anthraquinone (AQ)	Si/SiO_2	DC magnetron sputtering + Chlorination + Electrochemical grafting	4600	1 M KOH	1.1	44	338	NA	NA	Single electrode	[156]

CVD = Chemical Vapor Deposition; DLW = direct laser writing; PET = polyethylene terephthalate

Laser-Induced Graphene

Laser-induced graphene (LIG) or laser scribed graphene (LSG) has attracted much attention for its application as MSC electrodes since its discovery in 2014 as a 3D porous material prepared from various carbon materials by direct laser writing [151,195]. Its popularity is due to the fact that it can be prepared and patterned into highly porous 3D graphene in a single step without the need for wet chemical processes [151]. The high porosities created, due to the release of gas during the laser scribing process, result in a large surface area, thereby facilitating the electrolyte penetration into the active materials [195].

Some innovative strategies, including photochemical reduction in GO, are being explored to address the scalability challenges [54,196]. Another strategy is the introduction of spacers, such as carbon nanotubes (CNTs), between the graphene sheets to prevent their restacking [164]. Heteroatom doping can effectively tune the material structure, introduce pseudocapacitance, and facilitate electrolyte wettability, consequently enhancing charge storage capacity [151,197–199]. Such doping elements include S [199], F [197], P [198], and heteroatoms O/N/S [200]. In addition, surface modification is an effective approach to incorporating high-mass-loaded electroactive materials such as other carbon materials [181], such as other carbon materials layer [181], transition metal oxides/hydroxides [201–203], MXene [173], and conductive polymers [204]) to the porous surfaces to enhance the electrochemical performance [167,171,205–207].

The use or incorporation of the pseudocapacitive materials with a larger specific capacitance moves the carbon electrode from pure double-layer to pseudocapacitive charge storage, combining their synergistic/complementary properties (pseudocapacitance and EDLC) to offer better MSCs performance. However, this strategy has some drawbacks, as it can lead to reduced power capabilities, a shorter cycle life due to the kinetic limitations of the redox reactions, and low electronic conductivity [54,208].

An example is reported by Lin et al. [209] where interdigitated MSC electrodes based on a porous hierarchic 3D graphene-CNT composite were fabricated using conventional photolithography on a silicon substrate. The graphene-CNT composite was grown by CVD on a patterned Ni (a current collector and catalyst for the composite growth). The scheme of the device is shown in Figure 7a. The figure shows the SEM image of the fabricated MSC and a cross-sectional SEM image of the graphene-CNT structure grown on a Ni catalyst/current collector, respectively. The CV curves with a near-perfect rectangular shape show that the MSC based on the composite electrode (tested in an aqueous electrolyte of 1 M Na_2SO_4) shows improved performance over the one with only the graphene electrode. The enhanced capacitance was attributed to the ion absorption/desorption in the CNTs. The device achieved specific capacitances up to 2.16 mF cm^{-2} with a maximum power density of 115 W cm^{-3} in an aqueous electrolyte; the surface capacitance and volumetric energy density achieved in ionic liquids were 3.93 mF cm^{-2} and 2.42 mWh cm^{-3}, respectively.

Beidaghi et al. [164] fabricated interdigitated graphene-CNT composite-based MSC, combining electrostatic spray deposition (ESD) and photolithography lift-off methods for the device fabrication. The device was tested in a 3 M KCl aqueous electrolyte, exhibiting a capacitance of 6.1 mF cm^{-2} at 10 mV s^{-1}, an energy density of 0.68 mWh cm^{-3} and a power density of 77 W cm^{-3}. Lin et al. [189] obtained patterned 3D networks (porous) graphene films from polyimide (PI) films using a CO_2 infrared laser; the sp^3-carbon atoms of the PI were photothermally converted to sp^2-carbon atoms by pulsed laser irradiation, resulting in LIG (LI-rGO) formation. The interdigitated electrode exhibits a low specific capacitance of >4 mF·cm^{-2} and power densities of ~9 mW·cm^{-2}. The enhanced capacitance, compared to other carbon-based electrodes, has been attributed to the 3D network of highly conductive graphene, providing easy access for the electrolyte to form a Helmholtz layer [189].

In another study, Gao et al. [203] prepared LSG and LSG-MnO nanocomposite films on PET as interdigital electrodes for MSCs by one-step picosecond laser direct-writing (LDW) in air, having thicknesses of 52 μm and 55 μm, respectively. The performance of the LSG and LSG-MnO electrodes showed a specific capacitance of 191 and 470 mF cm^{-2}, respectively; the CV curves of the electrodes over 0.8 V showed that LSG-MnO exhibits

a larger integrated area and greater current response than the LSG electrode, indicating higher capacitance and better electrochemical activity, which is attributed to the synergistic effects of the EDLC of LSG and the pseudocapacitance process of MnO films. Moreover, the maximum area-specific capacitance of LSG-MnO-based MSCs with PVA/H_3PO_4 gel electrolyte is 55 mF cm^{-2} and recorded a good capacitance retention of about 96% after 5000 cycles. The device delivers a maximum energy density with PVA/H_3PO_4 gel electrolyte of 4.89 μWh cm^{-2} and a maximum power density of 0.72 mW cm^{-2}.

3.1.2. Carbon Nanotubes (CNTs)

Carbon nanotubes (CNTs) are considered promising electrode materials for on-chip MSC applications due to their high surface area, excellent electrical conductivity, mechanical flexibility, and chemical stability [152,153,210–212] CNTs are categorized into single-wall CNT (SWCNT) and multi-wall CNT (MWCNT) [154,210]. However, a major issue associated with the use of CNTs is their structural breakdown, which results in decreased electrical conductivity and mechanical strength [213]. This could be addressed by incorporating other functional materials inside their interconnected pores to prevent such structural breakdown [213]. In addition, CNT film preparations are mostly performed through solution routes, limiting their use for on-chip MSC applications. Several studies have explored alternative approaches to fabricating MSCs based on CNT electrodes, especially flexible MSCs [152]. Kim et al. [153] used selective wetting-induced micropatterning for MWCNTs-based MSCs. It has been demonstrated from recent studies that the performance of CNT-based electrode materials is highly dependent on nanotube alignment and packing density [154,210]. Highly aligned CNTs that are either horizontally (HACNTs) or vertically (VACNTs) aligned present good pathways for electron transport, which results in superior performance compared to randomly entangled CNT networks. HACNTs-sheet-based MSCs exhibit better electrochemical performance when compared with VACNT, as the latter exhibits lower areal capacitance and volumetric performance. This is because HACNTs have a long-range alignment interconnected network that facilitates charge transport, leading to better conductivity and a higher packing density, which enhances the energy density [152,210,211].

Cao et al. [192] prepared multiwall CNT-forest by plasma enhanced chemical vapor deposition (PECVD) on silicon wafer (before transferred onto elastomer) to achieve very low capacitance values (5 mF cm^{-2} and ≈ 2.5 F cm^{-3}) and retain close to 90% of the initial capacitance after 10,000 cycles (see Figure 7b). Pseudocapacitive materials are usually employed to enhance the electrochemical performance of the CNT-based electrodes, combining the synergetic effects of EDLC and pseudocapacitance [214,215]. This was demonstrated by Dousti et al. in 2020 [154], who for the first time fabricated an interdigitated electrode with HACNT using a single oxygen plasma etching process for fabrication. The device with HACNT (~300 nm-thick) films achieved volumetric capacitance, energy, and power densities of 75.7 Fcm^{-3} (at 5 mV s^{-1}), 10.52 $mWhcm^{-3}$ and 19.33 Wcm^{-3}, respectively, in 0.1 M Na_2SO_4, while the performance was significantly improved using the HACNT-MnO_2 composite (~300 nm-thick) electrode, demonstrating a volumetric capacitance, energy, and power densities of 242 Fcm^{-3} (at a scan rate of 5 mV s^{-1}), 33.7 $mWhcm^{-3}$, and 31 Wcm^{-3}, respectively, with an impressive long cycle life (>90% capacitance retention after 7000 cycles). It was reported that the interdigitated electrode HACNT-MnO_2 composite sheet-based MSCs outperformed the existing planar thin-film MSCs at the time and could match the performance of 3D MSCs [154]. Ouldhamadouche et al. [214] prepared hierarchically composite electrodes consisting of porous and nanostructured VN grown on vertically aligned CNTs (VACNTs) for micro-supercapacitor applications. The CNTs were grown on a Si/SiO_2 substrate through a distributed electron cyclotron resonance (ECR)–plasma enhanced chemical vapor deposition (PECVD) process, after which a direct deposition of vanadium nitride (VN) films over the as-prepared CNTs arrays was performed by means of reactive DC sputtering. The composite VACNTs-VN electrode demonstrated an areal capacitance of 37.5 mF cm^{-2} at a scan rate of 2 mV s^{-1} in a 0.5 M K_2SO_4 electrolyte solution

between −0.1 and 0.4 V potential windows. Pitkänen et al. [216] fabricated a composite VACNTs-MnO_x-electrode-based on-chip MSCs. The device achieved a specific areal capacitance of 37 mF cm^{-2}, and an energy density of 6.7 µWh cm^{-2}. Zhang et al. [217] fabricated interdigital 3DTiN-TiO_2-VACNT-based MSC using area-selective atomic layer deposition by aerosol jet printing technique. The device achieved the composite TiN-TiO_2-VACNT MSC with an areal capacitance of 6.55 mF cm^{-2}. This achieved nearly two orders of magnitude improvement compared to the pure VACNT MSC (0.07 mF cm^{-2}). The presence of the pseudocapacitive materials (TiN-TiO_2) significantly improved the energy density (3.28 mWh cm^{-2}) while maintaining a high power density (2.34 mW cm^{-2}).

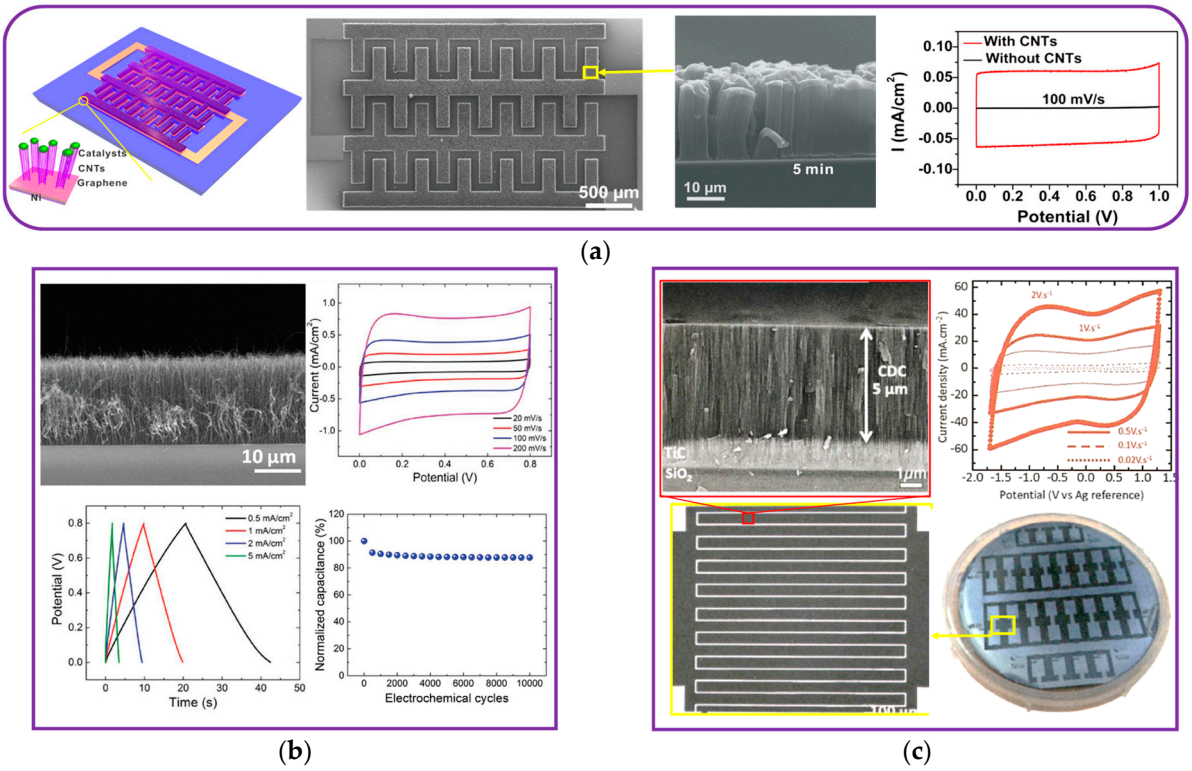

Figure 7. Carbon-based electrodes (**a**) Graphene-CNT grown on a Si substrate. Reproduced with permission from [209]. Copyright © 2024, American Chemical Society. (**b**) Vertically aligned carbon nanotube (VACNT) forests grown on a silicon wafer. Reproduced with permission from [192]. Copyright (2019), John Wiley & Sons. (**c**) Carbide-derived carbon (CDC) on a Si wafer. Reproduced with permission from [54]. Copyright (2016), American Association for the Advancement of Science.

3.1.3. Porous Carbide-Derived Carbons

Carbide-derived carbons (CDC) are a type of nanoporous carbon material that is obtained by subjecting a metal carbide, typically titanium carbide (TiC), to chlorination. This process results in the formation of a bilayer of TiC and porous carbon (TiC-CDC). TiC-CDC is a highly promising material for on-chip MSC applications due to its unique combination of high surface area, high capacitance, electrical conductivity, and chemical stability [54,157,161,218,219]. The use of TiC-CDC as electrode materials eliminates the presence of polymer binders between the substrate and the active materials, which is common to other carbon materials, ensuring a naturally strong interface between the current collector and the active material [157]. TiC films are typically deposited on Si wafers by reactive DC magnetron sputtering using a titanium target and acetylene (C_2H_2) gas as a carbon source. The reactive-sputtered TiC films are subsequently etched by chlorine

gas to form CDC films [54,157,161,218,219]. The following equation expresses the reaction process of carbide with chlorine gas [157,220].

$$TiC(s) + 2Cl_2(g) \rightarrow TiCl_4(g) + C(s) \quad (10)$$

A number of studies have fabricated TiC-CDC films as on-chip MSC electrodes at the wafer level [54,161,219]. For instance, Huang et al. [54] achieved MSC based on TiC-CDC electrodes via reactive DC magnetron sputtering followed by chlorination at the wafer level, as shown in Figure 7c. (A) The Si/TiC/CDC electrode with a 5 µm-thick CDC operated in 1 M H_2SO_4 electrolyte achieved 205 mF cm^{-2} (410 F cm^{-3}) with no capacitance loss after 10,000 cycles. Also, the MSC recorded 350 mF cm^{-2} in 1 M H_2SO_4 electrolyte at 10 mV s^{-1}.

3.2. Pseudocapacitive Electrodes

Pseudocapacitive materials are becoming the principal candidates for simultaneously delivering high energy and power densities as they occupy a middle ground between EDLCs and battery-type materials; they exhibit near-rectangular cyclic voltammetry (CV) profiles and almost linear galvanostatic charge/discharge (GCD) curves similar to EDLC [146,221]. The charge storage processes rely on a charge transfer mechanism instead of physically storing charge by electrostatic charge adsorption. The charge storage mechanism emanates from the electrosorption and/or fast Faradaic reversible redox reactions at the surface or subsurface of the redox-active materials; the surface Faradaic electron transfer is enabled by charge-compensating ions [45,222–224]. The Faradaic reaction in pseudocapacitive materials is ultrafast, which differs from battery-type materials where faradaic reactions occur at a constant potential, usually originating from the ideal Nernstian process [222,223]. Pseudocapacitance can arise from one or a combination of the following fast Faradic processes: redox, intercalation, and electrosorption [146,224,225].

From a technological point of view, it is highly desirable to prepare pseudocapacitive electrode films that are compatible with the cleanroom protocol, which is required by on-chip integration, and it is also important to consider microfabrication techniques capable of facilitating scale-up production of electrode materials at the wafer level. There are two main categories of pseudocapacitive materials: conducting polymers such as polyaniline (PANI) [226], poly(3,4-ethylene dioxythiophene) (PEDOT) [227], polypyrrole (PPy) polypyrrole (PPy) [227]), and metal-based pseudocapacitive compounds [228–231]. Metal-based materials are often preferred for on-chip applications due to their versatility and compatibility with microfabrication processes. Metal compound-based MSCs remain the exploration hotspot for achieving high power and energy densities in a limited footprint area and volume. The emerging metal-based electrode materials for on-chip MSC applications can be classified as follows:

i Metal oxides/hydroxides
ii Metalnitrides
iii 2D transition metal carbides/carbonitrides (MXene)

Other metal compounds, including metal dichalcogenides, such as MoS_2, exhibit pseudocapacitance properties, high electrical conductivity, and a good hydrophilic nature. However, their implementation for on-chip implementation is restricted due to processing techniques, including hydrothermal [232,233], colloidal [234], chemical bath [235], chemical precipitation and ion-exchange process [140], and successive ionic layers [6,9,11,12,236].

3.2.1. Metal Oxides

Metal oxides are the centerpiece of (micro-)pseudocapacitive electrode material exploration; they exhibit multiple oxidation states, allowing for effective redox charge transfer [150]. Oxides or hydroxides of different metals, such as Ru, Mn, Ni, Co, Fe, Ti, V, Mo, W, and Nb, have shown promise as redox-active materials for MSC electrodes. The electrochemical behavior of these oxides in aqueous electrolytes explains their charge

storage mechanisms, involving fast Faradaic and implicit non-Faradaic EDLC processes at the surface/subsurface [146]. The fast Faradaic redox process involves [146,237,238]:

i. valence changes (electron transfer) of the metallic species located near the oxide surface,
ii. serving as redox-active centers through cation intercalation/deintercalation, surface adsorption/desorption, or
iii. surface redox reactions with anions.

The valence changes in the oxide materials occur at different potential ranges, which are essentially determined by the nature of the electrolytes [237]; in aqueous electrolytes, for instance, the valence changes in Ni^{2+}/Ni^{3+} and Co^{2+}/Co^{3+} occur in the ranges of ≈0 and 0.6 V (0–0.6 V vs. Hg/HgO [239]), Mn^{3+}/Mn^{4+} (≈0–0.8 V vs. Ag/AgCl [228]), and Fe^{2+}/Fe^{3+} (−1–0 V vs. SCE) [240]. RuO_2 and MnO_2 are the most representative metal oxide electrode materials and are widely known for their high theoretical capacitance and high energy density capability [241,242]. Several other metal oxides, such as MoO_2 [243], Co_3O_4, NiO [244], $MnFe_2O_4$ [236], IrO_2 [245], and $FeWO_4$ [128], are currently investigated for on-chip MSCs applications. In addition, the synergistic contributions from pseudocapacitance and EDLC processes are considered to enhance the energy storage capabilities of the MSCs by exploring metal oxide/carbon composites as electrode materials [18,221].

Besides on-chip compatibility issues, the electrochemical performance is also influenced by the preparation techniques. Notably, studies have shown that amorphous structures or hydrous forms of transition binary oxides (e.g., $RuO_2{\cdot}nH_2O$, $IrO_2{\cdot}nH_2O$, and $WO_3{\cdot}nH_2O$) exhibit better pseudocapacitive behavior than those of anhydrous structures or crystalline phases [6,246]. Currently, chemical or solution routes are dominant in the preparation of oxide electrodes. These methods typically require the use of expensive precursor solutions (such as $RuCl_3{\cdot}xH_2O$ for RuO_2 synthesis) and complex steps to prepare porous nanostructured oxide films with a large surface area [247–249]. Solution-phase processes have the potential to offer better capacitance performance compared to vacuum-deposited oxide thin films, such as physical vapor deposition (PVD) techniques (ex: sputtering deposition). However, the chemical routes are typically not fully compatible with microfabrication protocols, especially when interfacing with other electronic devices. Indeed, some chemical routes, like electrodeposition and electrophoretic deposition techniques, are widely used to produce high-performance porous oxide thin film electrodes, especially 3D oxide electrodes, taking advantage of the film conformality feature [145,250–252]. These techniques may be attractive and compatible with electronic microfabrication protocols, but they are only suitable for individual prototyping and lab-scale applications [59,241]. Table 3 summarizes the recently explored metal oxide electrodes for on-chip MSC applications.

Electrodeposition has successfully created mesoporous oxide MSC electrodes with ordered 3D architectures, such as RuO_2 and MnO_2 electrodes [145,250–252]. These 3D electrode materials allow good penetration of electrolytes and reactants into the entire electrode matrix and high mass loading of active materials [6,253]. Three-dimensional electrode materials are desirable where the footprint area is limited, such as on-chip MSC, to improve the surface-to-volume ratio, leading to significantly enhanced energy densities [6,253]. Additionally, the active layer is conformally deposited on a 3D scaffold with a high area enhancement factor (AEF), resulting in at least one order of magnitude improvement in the areal capacitance of 3D MSCs compared to planar geometry [6].

Physical vapor deposition (PVD) techniques are receiving more attention for the preparation of high-quality and contamination-free oxide thin film electrode materials for MSC applications [131,254]. These techniques are more eco-friendly than chemical routes. Different types of PVD techniques are available, such as molecular beam epitaxy, evaporation, and magnetron sputtering. The semiconductor industry commonly uses these techniques to deposit dense metallic or semiconducting films on large substrates [59,128,236,255]. Among these techniques, magnetron sputtering is considered the most fascinating tool due to its versatility and ability to produce tailored porous oxide film electrodes for on-chip MSCs [59]. Additionally, sputtering deposition leverages the ability to prepare thin films on large substrates or silicon wafers, making it a preferred choice for mass production of

porous metal compound-based electrodes used in on-chip MSC applications. However, oxide electrode films produced through sputtering may exhibit lower capacitance compared to 3D electrodes produced through chemical routes.

Ruthenium Oxides

Ruthenium oxide (RuO_2) is a model pseudocapacitive electrode material for MSC applications. It is widely known for its high specific pseudocapacitance owing to its ability to undergo rapid redox reactions with its multiple valence states in a reversible manner [256], excellent conductivity, and high energy density capability [241,242,257]. It has multiple valence states for electron transition (Ru^{2+}, Ru^{3+}, Ru^{4+}, and Ru^{6+}) accessible within a 1.2 V electrochemical potential window during redox reactions [20,222,249]. The charge storage process in RuO_2 operated in acidic solutions is described in Equation (11) [6,18].

$$RuO_2 + xH^+ + x{\cdot}e^- \leftrightarrow RuO_{2-x}(OH)_x \quad (0 > x > 2) \tag{11}$$

The equation explains the participation of protons during the fast redox reaction where RuO_2 acts as a proton condenser; this reaction is electrochemically reversible [246]. The continuous change of 'x' during the fast redox reaction produces high specific capacitance [6]. Recent research has found that the specific capacitance of amorphous structures or hydrous forms of RuO_2 ($RuO_2{\cdot}nH_2O$) is superior to those of anhydrous structures or crystalline phase (i.e., rutile polymorph of RuO_2); this is because there are more permeable sites in $RuO_2{\cdot}nH_2O$ for protons, and the proton conduction inside RuO_2 is dominant compared to the electron conduction [6,246]. Hydrous regions are more permeable to protons, and as a result, proton conduction is the dominant form of conduction inside ruthenium dioxide instead of electron conduction. However, the hydrous forms of RuO_2 are usually prepared by solution-phase processes. The high cost associated with bulk RuO_2 has been controversial regarding its use for MSC applications. However, this concern has been arguably laid to rest as low mass loading (RuO_2) electrodes are required for MSC applications, typically less than 1 mg cm^{-2} [6,241,258].

Pioneering work on MSCs began two decades ago with a RuO_2 thin film electrodeposited by the reactive DC sputtering technique [256,259]. A solid electrolyte LIPON was sandwiched between two RuO_2 electrodes, but the capacitance realized was found to be much lower than the chemically obtained bulk RuO_2. The low capacitance was attributed to the dense morphology and anhydrous form of the thin film electrodes. Another issue identified was the low ionic conductivity of the solid electrolyte, limiting the rate capability due to the high ohmic drop [6,259]. Efforts have been made to improve the electrochemical performance through electrode topology/configurations. Hota et al. [247] explored different fractal electrode topologies, including Hilbert, Moore, and Peano, and the conventional interdigitated configuration of the sputtered RuO_2-based MSCs (Figure 8a).

Among the different electrode designs, Moore-design MSC topology exhibited the best electrochemical performance, with a capacitance of 11 mF cm^{-2} (168 F cm^{-3}) and an energy density of 23.2 mWh cm^{-3} at a power density of 769 mW cm^{-3}. The conventional interdigitated electrode structure has a capacitance of 8 mF cm^{-2} (125 F cm^{-3}) and delivers an energy density of 17.5 mWh cm^{-3} at the same power density. The MSC with the Moore design showed a 32% increase in energy density, which can be attributed to the active electrode surface being responsible for the improved performance and the increase in the electric lines of force coming from the edging effects in the fractal electrodes [247].

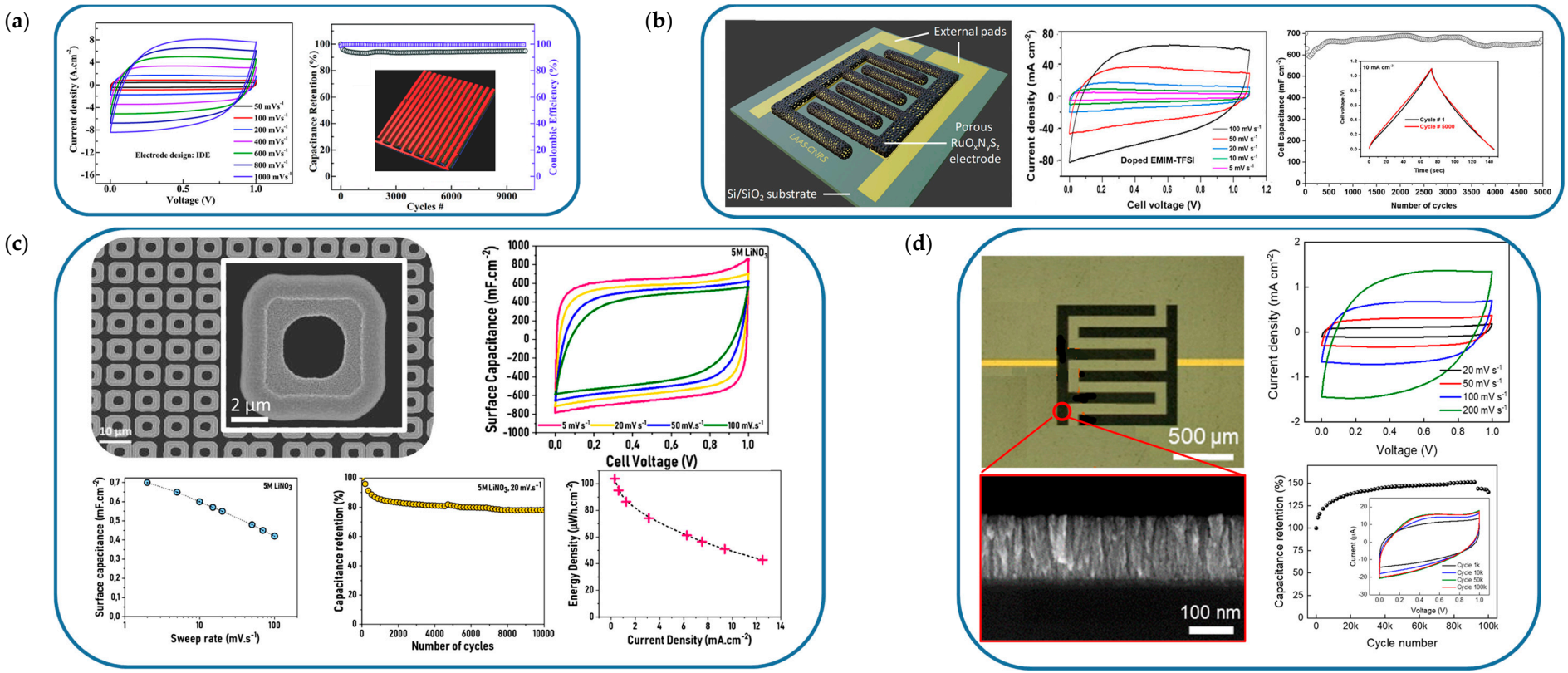

Figure 8. Metal oxide electrode materials for on-chip micro-supercapacitor applications. (**a**) Sputtered anhydrous RuO_2 thin-film electrodes. CV measurement, and stability of the interdigitated MSC of 10,000 cycles. Reproduced with permission from [247]. Copyright (2017), John Wiley & Sons-Books. (**b**) All-solid-state interdigitated microdevice based on porous $RuO_xN_yS_z$. CV plots in doped PVA and doped [EMIM] [TFSI] at different scan rates, and cell capacitance retention with the number of charge/discharge curves at 10 mA cm^{-2} (inset: 1st and 5000th potential–time curve during GCD). Reproduced with permission from [257]. Copyright © 2024, American Chemical Society. (**c**) 3D interdigitated MSCs based on electrodeposited MnO_2. Top view SEM images of the 3D MSC, CV of a 3D MSC in parallel plate configuration measured in 5 M $LiNO_3$ vs. the sweep rate, evolution of the surface capacitance, capacitance retention, and real energy density of the MSC, respectively. Reproduced with permission from [250]. Copyright (2021), Elsevier. (**d**) Interdigitated MSCs operating in physiological electrolytes based on sputtered iridium oxide films (SIROFs). SEM images of SIROF in cross-sectional view, CV measurements, and cycle stability of SIORF MSC over 100,000 CV cycles at 200 mV s^{-1}. Reproduced with permission from [245]. Copyright (2022), IOP Publishing.

Another approach to improving the electrochemical performance of RuO_2-based MSCs is the synergistic contributions of the unique properties of RuO_2 with other (pseudo)capacitive materials in a composite electrode configuration. Han et al. [249] demonstrated an example of this by uniformly coating vertical graphene with a porous RuO_2 film using a solution-free reactive magnetron sputtering technique. The composite electrode achieved an area capacitance of 15.3 mF cm^{-2}, with 50 nm-thick RuO_2 on 5 µm-thick graphene. Furthermore, the composite electrode retained excellent capacitance after 10,000 charging and discharging cycles. In another study featuring hydrous RuO_2 prepared on vertically aligned carbon nanowalls (CNW) through an expensive solution-based electrodeposition method reported by Dinh et al. [194], a high areal capacitance of 1 F cm^{-2} was achieved. This method is mainly suitable for laboratory applications. Despite concerted efforts, the satisfactory electrochemical performance of RuO_2-based MSCs via PVD techniques is yet to be achieved.

Several strategies have been proposed to scale up the collective fabrication of chemically prepared RuO_2 electrode-based MSCs and other oxide electrodes. For instance, Patrice Simon's group [241], demonstrated using laser writing techniques to integrate flexible MSCs on current collector-free polyimide foils. The microdevice delivered 27 mF cm^{-2} (540 F cm^{-3}) in 1 M H_2SO_4 and retained 80% of the initial capacitance after 10,000 cycles. The authors alluded to the fact that the laser writing fabrication process is simple and scalable on a large scale [241]. However, despite all the recorded landmarks with 2D electrode materials, the electrochemical performance of oxides has yet to meet the energy requirements of the microdevices employed in IoT applications.

This has led to the development of a novel 3D electrode material configuration, usually prepared through solution-phase processes, to boost the device's performance [251,260]. Asbani et al. [251] fabricated an efficient 3D RuO_2 electrode (∼400 nm-thick), which was step-conformally electrodeposited on a 3D silicon microtube. The 3D silicon microtubes were fabricated using deep reactive ion etching (DRIE). The 3D RuO_2 electrode exhibited remarkable areal capacitance of 4.5 Fcm^{-2} at 2 mVs^{-1}, while maintaining more than 2 Fcm^{-2} at 100 mVs^{-1} (10 s charge/discharge time) and maintaining 90% of the initial capacitance value after 10,000 cycles.

In addition, the introduction of heteroatoms like N and S in RuO_2 has been reported to influence the oxide microstructure and surface significantly and provide better access to active sites in MSCs, as demonstrated by the group of David Pech [257]. The group fabricated interdigitated MSCs based on hydrous $RuO_xN_yS_z$ electrodes (Figure 8b), and the conformally electrodeposited active material ($RuO_xN_yS_z$) on 3D porous current collectors exhibits an extremely high surface area with a nanodendritic network, demonstrating a high areal capacitance of 14.3 F cm^{-2} for the electrode (30 µm-thick films tested in 0.5 M H_2SO_4 at 5 mV s^{-1}) in an electrochemical window of 0 to 1.1 V and 714 mF cm^{-2} for an all-solid-state MSC fabricated on silicon wafer, using a poly(vinyl alcohol) (PVA)-based electrolyte doped with silicotungstic acid ($H_4SiW_{12}O_{40}$, SiWa), with stable performance (>80% retention after 5000 cycles). The device achieved a specific energy density of 120 µWh cm^{-2} and a maximum power density of 421 mW cm^{-2}. The cell voltage of the device was extended up to 2.3 V when doped [EMIM] [TFSI] was used as the electrolyte. However, this came at the expense of a lower cell capacitance and higher ESR, while it achieved the energy and power density of 128 µWh cm^{-2} and 110 mW cm^{-2}, respectively [257].

Table 3. Metal oxide electrodes for on-chip MSCs.

Electrode Material	Substrate	Synthesis/Fabrication	Thickness (nm)	Electrolyte	Cell Vol. /Pot. Window, V	Areal Cap. mF cm^{-2}	Configuration	Reference
RuO_2	3D-Pt nanotubes	Electrodeposition	130	0.5 M H_2SO_4	1.35	320	3D Single electrode	[261]
RuO_2	$Si/SiO_2/Ti/Au$	Electrodeposition/photolithography		0.5 M H_2SO_4	0.9	3		[262]
$hRuO_2$	3D silicon microtubes scaffold + Al_2O_3/Pt	Electrodeposition/photolithography	427	0.5M H_2SO_4	1	4300	3D-parallel plates	[251]
RuO_2-Au		Electrodeposition	NA	PVA-H_3PO_4-SiWA	0.9	3473	3D-parallel plates	[260]
$hRuO_2$-carbon nanowires (CNWs)	$Si/Si_3N_4/Cr/Pt$	Electrodeposition + CVD/direct laser writing	12,000	0.5 M H_2SO_4	0.8	1094	Single electrode	[194]
RuO_2-graphene	Si-SiO_2	PECVD + reactive sputtering	550	PVA-H_3PO_4 hydrogel	1	15.3	Single electrode	[249]
$RuO_xN_yS_z$	SiO_2-Ti-Au-3D Porous Au	Electrodeposition/photolithography	200,000	0.5 M H_2SO4	0.85	14,300	3D Single electrode	[257]
$RuO_xN_yS_z$	SiO_2-Ti-Au-3D Porous Au	Electrodeposition/photolithography	30,000	PVA-SIWA	1.1	714	3D Interdigitated	[257]
MnO_2	3D silicon microtubes scaffold	Electrodeposition	200	5 M $LiNO_3$	1	185	Single electrode	[250]
MnO_2	Si-SiO_2	Electrodeposition/photolithigraphy	3000	1 M Na_2SO_4	0.8	56.3	Intedigitated	[228]
MnO_2	3D silicon microtubes scaffold + Al_2O_3/Pt	Electrodeposition/photolithography	350	0.5 M Na_2SO_4	0.8	650	3D-interdigitated	[263]
MnO_2	3D siliconmicrotubes + Al_2O_3/Pt	Electrodeposition	15	0.5 M Na_2SO_4	0.8	670	3D-interdigitated	[162]
MnO_2nanotubes	PET/3D polycarbonate (PC) membrane	Electrodeposition/PDMS-assisted transfer/photolithigraphy	8000	PVA-Na_2SO_4 hydrogel	1	13.2	3D-interdigitated	[264]
MnO_2-graphene	Graphene (LSG)	Electrodeposition/direct laser writing	15,000	1 M Na_2SO_4	0.9	852	Interdigitated	[201]
MnO_x-Au	PET	E-beam evaporation/photolithography	50	PVA-H_2SO_4 hydrogel	0.8	0.164	Interdigitated	[265]
$Ni(OH)_2$	PET-Ni	hydrothermal + spin coating/photolithigraphy	600	PVA-KOH hydrogel	0.7	0.528	Interdigitated	[266]
$Ni(OH)_2$	Polyethylene naphthalate (PEN) sheet	chemical bath deposition process (CBD)/photolithigraphy	500	1 M KOH	0.6	16	Interdigitated	[239]
$NiFe_2O_4$	PET-Ni	electrospinning/photolithography	300	PVA-KOH hydrogel	0.8	0.067	Interdigitated	[267]
$FeWO_4$	$Si/Al_2O_3/Pt$	Reactive DC magnetron sputtering	900	5 M $LiNO_3$	0.6	3.5	Single electrode	[128]
$(Mn,Fe)_3O_4$	$Si/Al_2O_3/Pt$	Reactive DC magnetron sputtering	3870	1 M Na_2SO_4	1	80	Single electrode	[236]
IrO_x	Si/SiC/Ti/Pt	DC magnetron sputtering/ lift-off photolithography	300	Phosphate-buffered saline (PBS)	1	12.75	3D Interdigitated	[245]

Table 3. *Cont.*

Electrode Material	Substrate	Synthesis/Fabrication	Thickness (nm)	Electrolyte	Cell Vol. /Pot. Window, V	Areal Cap. mF cm^{-2}	Configuration	Reference
S-doped graphene	Si/SiO_2	Spin coating/plama etching	10	PVA-H_2SO_4 hydrogel	1	0.582	Interdigitated	[199]
F-doped graphene	PET	Mask-assisted filtration	1000	$EMIMBF_4$/PVDF-HFP ionogel	3.5	17.4	Intedigitated	[197]
P-doped graphene	Kevlar fabric	Laser direct writing	59,400	PVA-H_3PO_4 hydrogel	0.8	125.35	Intedigitated	[198]
Cl-doped graphene	PET	Mask-assisted filtration	500	$EMIMBF_4$/PVDF-HFP ionogel	3.5	8	Intedigitated	[268]
O-N-S-co-doped graphene	Wood	Slurry coating/Laser direct writing	60,100	PVA-H_2SO_4 hydrogel	0.8	82.1	Intedigitated	[200]
Graphen-Thiophene	PET	Vacuum-filtering/Plasma etching	105	PVA-H_2SO_4 hydrogel	1	3.9	Intedigitated	[269]
Graphene-Phosphorene	PET	Mask-assisted vacuum filtration	2000	BMIMPF6	3	9.8	Intedigitated	[177]
Graphene-PEDOT	PET	Pen lithography	20,700	PVA-H_2SO_4 hydrogel	1.2	16	Intedigitated	[204]
Graphene-CNTs/ Ag nanowires	Si/SiO2 and PET	Plasma-jet based 3D printing	20,000	PVA-H_3PO_4 hydrogel	0.8	21.6	Intedigitated	[270]
rGO-RuO_2	Free-standing fiber sheet	modified Hummers + hydrothermal	42,500	1 M H_2SO_4	1	4479.5	Free-standing fiber sheet	[202]
rGO-RuO_2	Free-standing fiber sheet	modified Hummers + hydrothermal	42,500	PVA-H_3PO_4 hydrogel	1	833.425	3D-interdigitated	[202]
rGO-MnO_2	NA (tansfarable to any substrate)	Photomodulation/shaped femtosecond laser (SSFL)	3000	0.5 M Na_2SO_4	2	128	3D-interdigitated	[271]
rGO-WO_3	highly oriented pyrolytic graphite (HOPG)	Electrodeposition	31,500	0.158 M H_2SO_4	1	178	parallel plates	[271]
rGO-MnO_2	Polyimide/Au	Doctor blade + electrodeposition/Laser scribing	15,000	0.5 M Na_2SO_4	0.9	852	3D-interdigitated	[201]
rGO-ZnO	PET	hydrothermal reaction/Laser scribing	11,000	PVA-H_2SO_4 hydrogel	1	4.3	Intedigitated	[272]
Graphene-V_2O_5	PET	Electrochemical exfoliation + hydrothermal method/Plasma etching	300	PVA-LiCl hydrogel	1	3.9	Intedigitated	[273]
rGO-V_8C_7	PET	Continuous centrifugal coating and laser scribing	13,000	PVA-LiCl hydrogel	0.8	49.5	Intedigitated	[274]
rGO-PPy	Free-standing nanosheets	Polymerization + Mask-assisted filtration	7000	PVA-H_2SO_4 hydrogel	0.8	81	Intedigitated	[275]
CNTs-Ni	Polycarbonate (PC) sheet	Maskless laser-assisted dry transfer/direct laser writing	50,350	TMOS:FA:EMI TFSI ionogel	3	0.43	Intedigitated	[211]

Manganese Oxides

Manganese oxides (MnO_x), especially MnO_2, are among the most appealing pseudocapacitive electrode materials due to their abundance, low cost, and high theoretical capacitance [18]. MnO_2 has been a focus of exploration as pseudocapacitive electrodes for MSC applications since the publication of the pioneering work by the Goodenough research group in 1999 [276]. Their work highlighted the pseudocapacitive behavior of MnO_2 in a neutral aqueous solution. However, achieving high capacitance performance with pristine MnO_2-based electrodes in a planar ultrathin configuration is challenging. This is primarily due to the low mass loading, poor electrical conductivity (10^{-5} to 10^{-6} S cm^{-1}), low structural stability and flexibility caused by volume expansion during charge and discharge, and electrochemical dissolution of active materials, leading to rapid capacitance degradation [146,253,265].

Consequently, several strategies have been undertaken to stabilize and improve the capacitance of the MnO_2 through structural optimization (e.g., amorphous and α-, β- and λ-type crystalline MnO_2 electrodes) [277,278], defect chemistry (e.g., mixed oxides, MnO_2–polymer composite electrodes, MnO_2-nanostructured carbon composites, noble metals) [131,279], tuning the morphologies (e.g., nanofilbers, nanorods, nanosheets) [130,280], and controllable incorporation of porosities [281], into the material to provide sufficient void nanospaces to accommodate volume expansions (i.e., better stress/strain accommodation). The porous morphology can provide a large accessible surface area, facilitate electrons/ions diffusion kinetics, stabilize the electrodes during the cycling process, and ensure good structural integrity for a long life cycle [131,282–284]. In addition, α-MnO_2 is considered the most promising phase among the various crystallographic structures of MnO_2; it has large tunnel sizes formed from double chains of MnO_6 octahedra, which position the material to store more foreign cations while enabling the conversion of Mn^{4+} to Mn^{3+} ions for charge balance in reversible redox reactions, delivering it with the highest specific capacitance [131]. The pseudocapacitive behavior of MnO_2 operated in neutral electrolytes can be explained by two fast Faradaic redox reactions: the intercalation process and the surface adsorption/desorption mechanism [285]. The first process involves the fast intercalation of protons (H^+) and/or alkali cations (C^+ = Na^+, Li^+, K^+...) coming from the aqueous electrolyte during the redox reaction via fast Faradaic reaction in the bulk film of the MnO_2, as described in Equation (12) [6,285].

$$MnO_2 + xH^+ + yC^+ + (x + y)\cdot e^- \leftrightarrow MnOOH_xC_y \quad (12)$$

where x and y represent the number of moles of H^+ and cations of C^+ in the electrolyte intercalated in MnO_2, respectively.

On the other hand, the adsorption/desorption mechanism involves fast and reversible surface redox reactions at the surface or near the surface of MnO_2 rather than ion intercalation [253,285], as expressed in Equation (13).

$$(MnO_2)_{surface} + C^+ + e^- \leftrightarrow (MnOOC)_{surface} \quad (13)$$

In both Faradaic processes, a redox reaction occurs between the III and IV oxidation states of Mn ions [253,285]. The pseudocapacitive behavior contributes to the high-power density of MnO_2-based electrochemical devices.

Thin-film electrodes based on MnO_2 are usually prepared via chemical routes such as sol–gel coating [286], vacuum filtration [284], electrodeposition [287,288], and electrophoretic deposition [287,288]. MnO_2 thin film electrode deposition via PVD techniques such as electron beam evaporation [265] and sputtering [131,289] has been reported. Si et al. [265] deposited MnO_2 thin film electrodes on polyethylene terephthalate (PET) substrates using electron beam evaporation; the 50 nm-thick MnO_x electrode exhibits a volumetric capacitance of 37.9 F cm^{-3} at a scan rate of 10 mV s^{-1}. The low capacitance obtained was attributed to the poor electronic conductivity of the film; the conductivity was enhanced by incorporating very thin layers of gold into the MnO_x layer as conductive

additives to enable effective charge transport and electrode integrity. The 50 nm-thick MnO_x/Au electrode exhibits a volumetric capacitance of 78.6 F cm^{-3} at a scan rate of 10 mV s^{-1}, resulting in ~107% performance enhancement over the pristine MnO_x electrode. The composite electrode stores charge through the synergetic contribution of the double-layer and pseudocapacitive processes of the active MnO_x coupled with the highly conductive gold, contributing to the total capacitance [265]. Interdigitated MSCs fabricated with 50 nm-thick MnO_x/Au composite film electrode fingers demonstrated a volumetric capacitance of 58.3 F cm^{-3}, exhibiting a maximum volumetric energy density of 1.75 mW h cm^{-3} and a maximum power density of 3.44 W cm^{-3}, which is adjudged to have performed better than many existing double layer MSCs [265].

Kumar et al. [131] deposited a high specific surface area and large aspect ratio a-MnO_2 nanorod's forest (~1 µm-thick) via reactive DC sputtering technique on silver (50 nm-thick) coated porous anodic aluminum oxide (AAO) substrate. The areal capacitance of the electrode tested in 1 M Na_2 SO_4 was found to be 207 mFcm^{-2} at a scan rate of 2 mVs^{-1}. Broughton and Brett [289] used a double-step sputtering-electrochemical oxidation process to obtain manganese oxide thin films; the electrode thin films were synthesized by anodic oxidation of metallic films deposited by sputtering, starting from vacuum deposition of manganese metal onto Pt coated Si wafers in an Argon atmosphere and subsequent electrochemical conversion of the metal film into capacitive oxide with a porous and dendritic structure in a 1 M Na_2SO_4 electrolyte. The oxidation behavior was studied by chronopotentiometry (CP) under constant current and linear sweep voltammetry (LSV) techniques. The thin film electrode exhibits pseudocapacitive behavior in the neutral electrolyte, but with a relatively low capacitance value.

Manganese oxide (MnO_x) composite electrodes have been reported for the MSC application [140,290,291], exhibiting higher stability of the oxidation states, which is crucial for long-term performance. The redox reaction of Mn ions in these oxidation states occurs spontaneously during the charge-discharge process and their relatively broad work potential window in aqueous electrolyte solution [292–295]. Li et al. [296] deposited Mn_3O_4 electrode thin films via electron beam evaporation on 300 nm-thick vertically porous nickel (VPN) sputtered on polyethylene terephthalate (PET) substrate. The Mn_3O_4 electrode achieved a volumetric capacitance of 533 F cm^{-3} at the scan rate of 2 mV s^{-1}; the interdigitated MSCs based on the Mn_3O_4 electrode were fabricated by a conventional photolithography process and achieved a volumetric capacitance of 110 F cm^{-3} at the current density of 20 µA cm^{-2}, retaining 95% of the initial capacitance after 5000 cycles under the current density of 20 µA cm^{-2} [296]. In another study, an asymmetric MSC comprising rGO//MnO_x exhibited an energy density of 1.02 mWhcm^{-3} at a maximal power density of 3.44 Wcm^{-3} [296], and the Sun group [297] achieved a specific capacitance of 73.25 mF cm^{-2} with graphene/MnO-Mn_3O_4 composite-based interdigitated MSC fabricated by the laser direct-writing method. The device delivered a maximum power and energy density of 1.29 mW cm^{-2} and 14.65 µWh cm^{-2}, respectively, retaining 90% of its initial capacitance after 5000 cycles.

Like 3D RuO_2 electrode materials, 3D MnO_2 electrode materials have been demonstrated by various groups [162,250,252,298]. For instance, Bounor et al. [250] demonstrated a collective fabrication of 3D MSCs integrated on silicon wafers (Figure 8c), using MnO_2 as the active electrode material deposited by a pulsed electrodeposition method. The 3D electrodeposited MnO_2 electrode films (1.24 µm-thick) exhibited 1.7 F cm^{-2} in 5 M $LiNO_3$ measured at a scan rate of 2 mV s^{-1}. The MSCs fabricated with 3D MnO_2 (450 nm-thick) exhibited the areal capacitance of 0.75 F cm^{-2} at 2 mV s^{-1} in 5 M $LiNO_3$ with the cell voltage of 1 V, delivering the energy density of 50–100 µWh cm^{-2} while keeping the power density high (>1 mW cm^{-2}) and the cycling life, retaining > 82% of the initial capacitance after 10,000 cycles [250]. In a recent study by the David Pech group, 3D MSCs were fabricated based on highly electrodeposited porous scaffolds of Ni/MnO_2. The electrodes exhibit high areal capacitance of over 4 F cm^{-2} and excellent cycling stability in the ionic liquid-based electrolyte using NaFSI/Pyr_{13}FSI [299].

Molybdenum Oxides

Molybdenum oxides (MoO_x, $2 \leq x \leq 3$) exhibit (pseudo)capacitive behavior in neutral or slightly acidic aqueous solutions, making them highly promising as MSC electrode materials, especially as negative electrodes [144,300,301]. The pseudocapacitive behavior of molybdenum oxides primarily arises from fast and reversible surface redox reactions. Mo oxides are structurally diverse with multi-valence states, multielectron redox is expected, given that Mo^{6+}, Mo^{5+}, and Mo^{4+} are all accessible and stable oxidation states [243,302–304]. Mo oxides exist in various stoichiometries, ranging from the nonconductive full stoichiometry MoO_3 with a large bandgap of about 3.0 eV to the more conductive reduced oxide MoO_2 [246,303]. These oxides are composed of layered MoO_6 octahedra structures formed by der Waal forces through edge or corner sharing; the structures are beneficial for the permeation of small ions such as H^+, Na^+, and K^+ [225,303,305,306]. Various forms of Mo oxide nanostructures [307,308] and nanocomposites [309] have been widely investigated as pseudocapacitive electrodes in classical supercapacitors, exhibiting outstanding theoretical specific capacitance (2700 F g^{-1}) [307,308]. However, there are limited reports on the use of Mo oxides as on-chip MSC electrodes [300,310].

The charge storage mechanism of MoO_x in an aqueous electrolyte can be explained by the fast Faradaic redox reactions, involving ion adsorption at the surface or near the surface of MoO_x accompanied by rapid and reversible electron transfer, as expressed in Equation (14) [225].

$$MoO_x + zC^+ + ze^- \leftrightarrow MoOOC \quad (14)$$

where C^+ and z represent surface-adsorbed alkali cations (C^+ = Na^+, Li^+, K^+, Zn^{2+}…) coming from the aqueous electrolyte and the number of electron transfers, respectively.

Orthorhombic phaseα-MoO_3 and MoO_2 are attracting more attention due to their thermodynamic stability, the unique layered crystal structure of α-MoO_3 with two interleaved sublayers, and the tunnel structure of MoO_2 [144,225,243,307,308,311–313]. However, the widespread practical applications of MoO_3-based electrodes in MSCs are limited due to poor electrical conductivity, low specific capacitance, and rapid deterioration owing to the lack of structural reliability during electrochemical reactions, resulting in poor electrochemical performance, which is attributed to the lack of electrochemically active centers and the low surface electrochemical activity of MoO_3-based materials [243,309,314].

The electrical conductivity of MoO_3 can be improved by (i) doping engineering, (2) defect engineering, such as introducing oxygen vacancies, MoO_{3-x} ($2 < x < 3$), to act as shallow donors by increasing the carrier concentration, and (3) crystal engineering, such as reducing crystal size and converting into quantum dots [243,315,316]. Both doping engineering and crystal engineering involve complex material preparation processes, which can limit their applications in on-chip devices. Additionally, accurately controlling doping atoms can be challenging, while crystal engineering may face difficulties such as coalescence. To introduce oxygen vacancies, several techniques can be employed, including heat treatment in a specific atmosphere, high-energy particle bombardment, and chemical post-treatment, among others [225,243,315,317]. Non-stoichiometric oxygen-deficient MoO_{3-x} ($2 < x < 3$) has been demonstrated to enhance the intrinsic electrical conductivity and produce an expanded interlayer distance in the MoO_3, structure, thus improving the electrochemical performance [315,317,318]. Synthesis of composites and doped MoO_3 electrode materials with metal ions can increase the number of electrochemically active centers at the surface, thus addressing the low specific capacities and rapid deterioration [309,313,319,320].

Zhang et al. [321] employed the screen printing technique to fabricate interdigitated MSCs on Au/polyimide (PI) substrates. The device delivered 41.7 mF cm^{-2} and 5.8 μWh cm^{-2} for the MSC with MoO_{3-x} nanorod microelectrodes with PVA/H_2SO_4 gel electrolyte, retaining 81% of the initial capacitance after long-term charging-discharging cycling at 2.5 mA cm^{-2} for 8000 cycles; this is considered one of the highest for the MSCs with interdigital metal oxide electrodes [296,321–323]. For on-chip implementation, more attention is given to growing the oxide film electrodes directly onto the substrate by PVD, especially the sputtering techniques; for instance, the Zhang group [243,300] deposited

MoO_x (x = 2.3) thin film via RF magnetron sputtering, and the MoO_x (~1 µm-thick) electrode achieved an areal capacitance of 31 $mFcm^{-2}$ at 5 mVs^{-1} in 0.5 M Li_2SO_4 [243]. The group further investigated the performance of the sputtered films (860 nm-thick) in an asymmetric MSC configuration containing $MoO_{2+x}(-)//2$ M $Li_2SO_4//MnO_2(+)$, demonstrating an energy density of 2.8 µWh cm^{-2} at areal power density of 0.35 mW cm^{-2}, and good stability with no capacitance loss for 10000 cycles [243,300].

As earlier remarked, MoO_2 electrodes exhibit better electronic and ionic conductivity, and the unique tunnel structure can facilitate fast ionic transport during intercalation/deintercalation reactions, expected to result in a high energy density [144,301]. However, MoO_2 suffers from instability; hence, most reports on MoO_2 electrodes for MSC applications are based on MoO_2 composite materials [324,325]. For instance, Lin et al. [325] prepared a laser-induced graphene/MoO_2 (LIG/MoO_2) composite using Mo ion homodispersed hydrogel ink as a precursor for the laser scribing process to fabricate interdigitated MSCs to deliver an areal capacitance of 81.8 mF cm^{-2} and an areal energy density of 113.7 µWh cm^{-2} at a power density of 2.5 mW cm^{-2} with PVA-H_3PO_4 gel electrolyte. Most of the reported MoO_2- and MoO_3-based electrodes for MSC applications are usually synthesized via chemical processes [144,326].

Iridium Oxide (IrO_2)

Iridium oxide (IrO_2) is an electrically conductive transition metal oxide and is projected as one of the most interesting oxide materials for MSC applications owing to its fast reversible redox reactions between the Ir^{3+} and Ir^{4+} oxidation states, good conductivity at room temperature, and excellent stability in acidic and basic solutions [327,328]. IrO_2 thin films, especially sputtered iridium oxide films (SIROFs), have been widely explored in other applications such as neural stimulation and recording electrodes in implantable bioelectronics due to their high charge capacity, low impedance, and biocompatibility [245], while the applications in MSCs are yet to be widely known. IrO_2 exhibits better pseudocapacitive behavior with its hydrated phase in an acidic solution, like most binary transition metal oxides such as RuO_2 and MnO_2. IrO_2 electrodes for aqueous MSCs application deposited by radio frequency (RF) sputtering were first reported by Liu et al. [327]. The sputtered IrO_2 thin films electrode was tested in 1 M $LiNO_3$ electrolyte, demonstrating the capacitive behavior; the sputtered IrO_2 thin films electrode was tested in 1 M $LiNO_3$ electrolyte, demonstrating the capacitive behavior within the potential window of 0–1.0 V (vs. SCE) (Figure 8d). The IrO_2 thin film electrode exhibits excellent cycling stability over 10,000 cycles in $LiNO_3$ solution, and the pseudocapacitive process within the IrO_2 thin film electrode was expressed as:

$$(IrO_2)_{surface} + C^+ + e^- \leftrightarrow (IrO_2^- C^+)_{surface} \quad (15)$$

where C^+ is the electrolyte cation

Inspired by the applications in neural interface research, Geramifard et al. [245] studied the electrochemical performance of the interdigitated MSCs based on 300 nm-thick SIROFs; the device was fabricated via lift-off photolithography and was operated in two different physiological aqueous electrolytes, phosphate-buffered saline (PBS) and an inorganic model of interstitial fluid (model-ISF) in a potential range of −0.6 to +0.8 V, exhibiting capacitance of 12.75 mF cm^{-2} (425 F cm^{-3}) in PBS and 6.7 mF cm^{-2} (223 F cm^{-3}) in model-ISF, and an energy density of 59.1 mWh cm^{-3} in PBS and 30.9 mWh cm^{-3} in model-ISF. The device demonstrated stability over 100,000 cycles at 200 mV s^{-1} without loss of capacitance in these electrolytes. In addition, a number of studies have investigated IrO_2 electrode composites [329].

Iron Oxides

Iron oxides, especially Fe_2O_3 and Fe_3O_4, are promising negative electrode materials in aqueous alkaline [330–332] and neutral [333–336] electrolytes; they exhibit a surface redox pseudocapacitance in a relatively wide operating potential window in negative

potential (0 to -0.8 V vs. Ag/AgCl) and behave like a battery material when the window is extended [337–340]. Fe oxides are structurally diverse with multi-valence states (Fe^0, Fe^{2+}, Fe^{3+}, etc.), and the rich oxidation-reduction reactions (Fe^{2+}/Fe^{3+}, Fe^0/Fe^{2+}, Fe^0/Fe^{3+}, etc.) are beneficial to high specific capacitance performance [341]. Crystal structures play a crucial role in adjusting the electrochemical properties/performance of the iron oxide electrode materials. Among the various crystal structures of Fe_2O_3, α-Fe_2O_3 (rhombohedral-centered hexagonal) is the most thermodynamically stable and more attractive candidate for MSC applications, while other phases such as β-Fe_2O_3 (cubic body-centered), γ-Fe_2O_3 (cubic structure of inverse spinel type), and ε-Fe_2O_3 (orthorhombic) are intermediary metastable and can easily evolve to α-Fe_2O_3 when subjected to heat treatment [342,343].

Despite their potential benefits, significant volume expansion, poor rate stability, low cycle lifetime, and poor electrical conductivity limit their practical applications as MSC electrodes [344]. However, attempts have been made to address these challenges, such as combining them with a highly conductive matrix to mitigate the structural distortion that usually leads to the deterioration of the inherently fragile material structure [344–347].

Tungsten Oxides

Tungsten oxides (W oxides), particularly WO_3, exhibit good electronic conductivity (10^{-6}–10 Scm^{-1}), high intrinsic density (>7 gcm^{-3}), multi-valence states (from W^{2+} to W^{6+}), and high theoretical specific capacitance (1112 Fg^{-1}) [348–353]. The charge storage mechanism of WO_3 arises from electrochemical intercalation/deintercalation with protons, as expressed in Equation (16).

$$WO_3 + xH^+ + xe^- \rightleftharpoons H_xWO_3 (0 < x < 1) \quad (16)$$

The demonstration of pseudocapacitive behaviors is considered an important merit for MSC applications [350,353,354]. Just like Mo oxides, W oxides appear in various stoichiometries, from stoichiometric WO_3 to more conductive nonstoichiometric WO_{3-x} ($2 < x < 3$) [355]. The crystal structure of W oxides plays a critical role in the electrochemical performance; WO_3 exists in various polymorphs, including tetragonal (α-WO_3), orthorhombic (β-WO_3), monoclinic (γ-WO_3), triclinic (δ-WO_3), monoclinic (ε-WO_3), and hexagonal (h-WO_3) [355,356]. Monoclinic (γ-WO_3) is the most stable phase among the crystal structures, while hexagonal (h-WO_3) is more attractive due to larger hexagonal tunnels to benefit the insertion of protons without changing the crystal structure, but unfortunately, the phase is metastable and can easily be transformed to monoclinic, which is the most stable phase [345,355,356].

It is worth noting that the bulk state of WO_3 exhibits battery-type energy storage behavior with redox phase transformation, so WO_3 is mostly used in composite electrodes, especially within a porous conductive carbon network; they exhibit pseudocapacitive behavior [141,353,354,357,358]. For instance, Shi et al. [359] prepared 3D hierarchical porous carbon/WO_3 nanocomposites using carbonization and solvothermal processes. The MSC based on the nanocomposites achieved a specific capacitance of 20 mF cm^{-2} in polyvinyl alcohol–sulfuric acid gel electrolyte. Again, Hapel et al. [360] employed a multi-step process to prepare a nanocomposite comprising WO_{3-x} and rGO by grafting WO_3 nuclei onto GO defect sites by electrochemical processing and nanoparticle growth, followed by the electroreduction in unprotected oxidation sites of GO to form a highly conductive reduced graphene oxide (rGO) support. The fabricated MSCs based on the composite electrode achieved a maximum energy density of 19.8 Wh cm^{-3} and a maximum power density of 80.4 Wcm^{-3}.

In addition, Shinde et al. [355] have proposed that metallic tungsten can be converted into various tungsten oxides through an electrochemical route, initiating from the surface of metallic tungsten interpenetrated with an aqueous electrolyte. The electrochemical properties of the surface oxide on metallic tungsten can be harnessed and greatly benefit the pseudocapacitance [361–364]. In this context, pure metallic W can be investigated as MSC electrodes.

Vanadium Oxides

Vanadium oxides are pseudocapacitive electrode materials and are known for their high power density, natural abundance, and high theoretical specific capacitance [221,344,365]. V oxides exhibit multiple oxidation states from +2 to +5. V^{5+} is the most stable, while V^{4+} is the most unstable, making V_2O_5 more attention-grabbing [221,344,357,366]. The crystalline form of V_2O_5 (orthorhombic) does not exhibit capacitive behavior when in bulk form but instead displays battery electrode characteristics, whereas amorphous V_2O_5 exhibits pseudocapacitive behavior [357,367]. However, poor electronic conductivity (10^{-2}–10^{-3} S cm^{-1}) and structural instability are major issues faced by vanadium oxides. Various strategies have been exploited to improve their electrochemical performance, including forming composites with highly conductive materials and structural control to stabilize the material [221]. Liu fabricated a 3D MSC with V_2O_3 to achieve a volumetric energy density of 110 mWh cm^{-3}. Huang et al. [368] fabricated vanadium oxide/carbon nanowire electrode composites to achieve a high areal capacitance of 1.31 F cm^{-2} at 1 mA cm^{-2} in a 5 M LiCl aqueous solution, and the MSC obtained a volumetric energy density of 3.61 mWh cm^{-3} at 0.01 W cm^{-3}, retaining 91% of its capacitance after 10,000 galvanostatic charge–discharge cycles.

Other Binary Metal Oxides

Other binary metal oxides, such as niobium oxides [369–371], titanium oxides [372,373], nickel oxides [374,375], cobalt oxides [376–378], and copper oxides [323,379] have been studied by various investigators. These pseudocapacitive electrode materials suffer poor electronic conductivity and structural instability, limiting their practical applications as MSC electrode materials. However, they have been explored as composites with highly conductive materials [370,372,373]. Oxygen deficient metal oxides could also propose nice electrical conductivity, which could be suitable for high power applications [315,380,381].

Mixed-Metal Oxide Electrodes

Many polycationic oxides have been found to exhibit a capacitive-like behavior and are considered one of the leading contenders to replace carbon-based electrode materials, especially in conventional supercapacitors. Examples of mixed-metal oxides that exhibit (pseudo)capacitive behavior include spinel oxides (AB_2O_4, A = divalent metal ion with +2 oxidation state and B = trivalent metal ion with +3 oxidation states) [382,383] such as $MnFe_2O_4$ [384] and $FeCo_2O_4$ [385]; perovskite oxides (ABO_3) such as; and wolframite transition metal tungstate (AWO_4, A = Mn, Fe, Co, Ni, Cu, Zn) such as $FeWO_4$ [386–388], $CoWO_4$ [389], $NiWO_4$ [390], $ZnWO_4$ [391], and $CuWO_4$ [391]. Unfortunately, the preparation routes of these compounds [386,392] are largely not compatible with microfabrication protocols employed in the electronics industries, thereby restricting their applications for on-chip MSC applications.

However, recent development has shown that there is a possibility of obtaining some of the multicationic mixed-metal oxide electrodes via magnetron sputtering techniques [128,236]. This is a game changer and one of the most promising candidates for on-chip MSC applications. For instance, Lethien group developed mixed-metal oxide electrodes by reactive DC magnetron sputtering, a deposition method widely used in the semiconductor industry to manufacture micro-devices [128,236]. The first study investigated sputtered wolframite-type oxide and iron-tungstate oxide ($FeWO_4$) films in a neutral aqueous electrolyte (5 M $LiNO_3$) (Figure 9a) [128].

The sputtered films exhibited capacitance behavior in the negative potential (vs. Ag/AgCl), in good agreement with the one reported for the $FeWO_4$ bulk counterpart [387]. The sputtered 900 nm-thick $FeWO_4$ film achieved an areal capacitance of 3.5 mFcm^{-2} at 10 mVs^{-1} with excellent capacitance retention. Regarding the low capacitance value obtained for this sputtered $FeWO_4$ film, a small amount of Fe or W is redox active. This group also investigated mixed Mn-Fe spinel oxide films in a neutral aqueous electrolyte (1 M Na_2SO_4) (Figure 9b) [236]. The electrochemical signature of the sputtered $(Fe,Mn)_3O_4$

spinel oxide films is comparable to those reported for their spinel-type Mn-Fe bulk counterparts [393,394]. The areal capacitance at 10 mVs^{-1} is 15.5 $mFcm^{-2}$ for 1 µm thick film, exhibiting excellent coulombic efficiency and long-term cycle stability after 10,000 cycles.

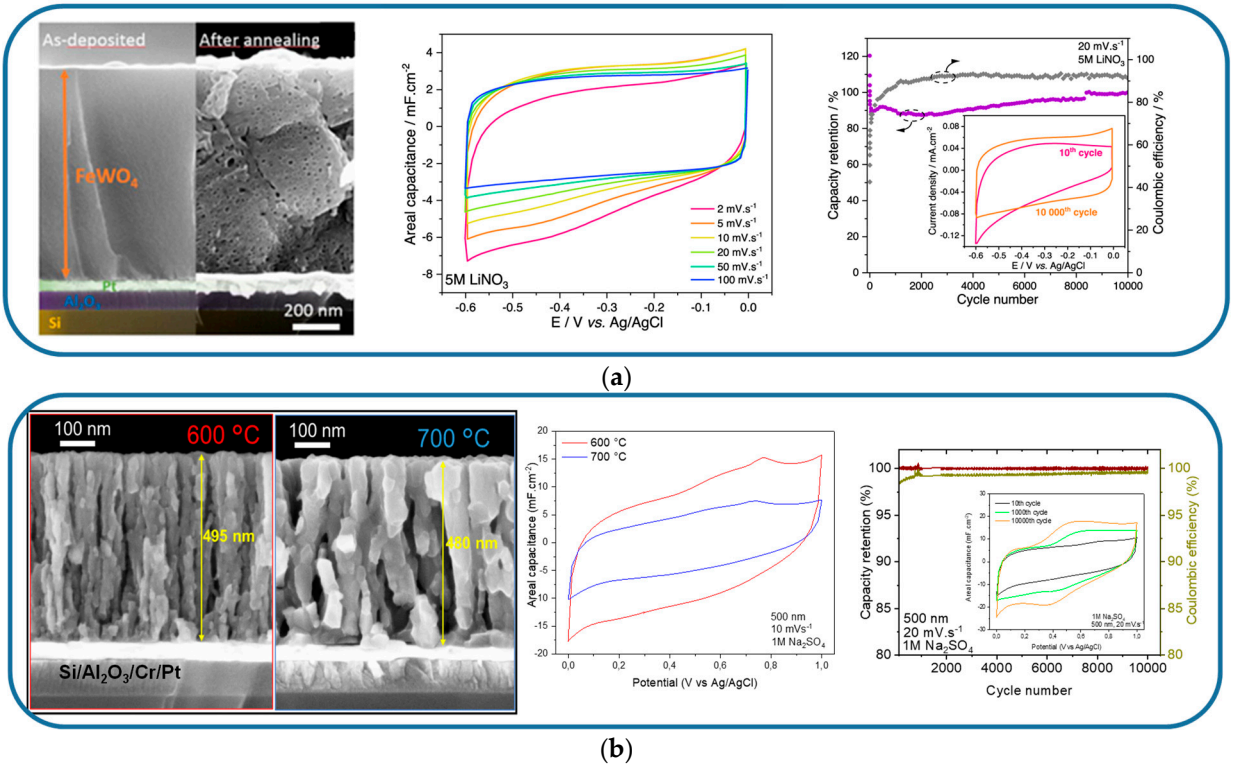

Figure 9. Multicationic oxide electrode materials for on-chip MSC applications. (**a**) Sputtered mixed Fe-W oxide thin film. SEM cross-section images, CV plots of the sputtered $FeWO_4$ films at different sweep rates in neutral aqueous electrolyte (5 M $LiNO_3$), and stability of the electrode over 10,000 cycles, respectively. Reproduced with permission from [129]. Copyright (2021), IOP Publishing. (**b**) Sputtered mixed Mn-Fe oxide thin film. SEM cross-section images of the sputtered films at different post-deposition heat treatments, CV plots of the sputtered $(Mn,Fe)_3O_4$ films at 10 mV s^{-1} in neutral aqueous electrolyte (1 M $NaSO_4$), stability of the electrode over 10,000 cycles, respectively. Reproduced with permission from [239]. Copyright (2022), IOP Publishing.

3.2.2. Metal Nitrides

Metal nitride-based electrode materials have attracted significant attention as promising pseudocapacitive electrodes due to their metal-like conductivity and excellent electrochemical properties [59]. Metal nitrides differ from metal oxide-based electrode materials, which exhibit high capacitance in their hydrous forms and are typically prepared using solution routes. High-performance metal nitrides can be obtained through vacuum deposition techniques, particularly sputtering deposition [139,145,395–398]. This benefit can also be leveraged to perform large-scale depositions of porous nitride thin films, which is considered an advantage for mass production of on-chip MSCs via microfabrication processes. Table 4 summarizes various nitride electrodes for on-chip MSC applications.

Vanadium Nitride

Vanadium nitride (VN) is the most widely investigated nitride material for MSC applications due to its outstanding electrochemical performance in aqueous media [399], multiple oxidation states (II–V), and high electronic conductivity (about 1.6×10^6 S m^{-1}) [398], bifunctional properties, serving as both the current collector and the electrochemically active material (working electrode) [400], its negative potential in aqueous electrolytes, which endows its utilization as negative electrodes in an asymmetric MSC configuration [45,145].

Brousse's group [400] investigated the charge storage mechanism in the VN film electrode prepared by reactive magnetron sputtering in both aqueous (KOH) and organic (NEt_4BF_4) electrolytes; they observed that the charge storage mechanism depends on the nature of the electrolytes. In the presence of KOH, fast and reversible redox reactions were observed, with characteristics of pseudocapacitance, while in the case of NEt_4BF_4 in acetonitrile enabled, only double layer capacitance was observed. Further investigation on the charge storage mechanism was conducted by Bondarchuk et al. [401], leaving room for speculation due to an uncovered anomalous non-faradaic capacitance.

The Lethien group [399] employed a combination of numerous advanced characterization techniques to further unravel the charge storage mechanism in the sputtered porous VN films (Figure 10a). The VN films were obtained via the sputtering deposition technique. X-ray photoelectron spectroscopy (XPS) with time-of-flight secondary ion mass spectrometry (ToF-SIMS) measurements were performed on the films to reveal the species of VN, vanadium oxide (+III and +IV), and a small amount of vanadium oxynitride in the films. A further analysis was conducted using times-resolved operando X-ray absorption spectroscopy (XAS) under synchrotron radiation in KOH electrolyte. The result clearly showed a thin vanadium oxide layer on the VN, which plays a key role in the fast charge transfer occurring during the redox process, and the V oxidation state in the VN film is close to +4, agreeing with the XPS results. The VN film primarily acts as a conductive scaffold for electron transport, while the amorphous mixed-valence vanadium oxides (+3/+4) serve as the redox-active material, allowing fast charge transfer.

A 16 µm-thick sputtered VN film was tested in 1 M KOH to achieve a high capacitance of 1.2 F cm^{-2} (>700 F cm^{-3}). It retained 80% of its initial capacitance after 50,000 cycles. Moreover, the MSC based on the sputtered VN electrode delivered 25 µWh cm^{-2}, which is quite competitive with cutting-edge transition metal oxide/nitride materials and exceeds the performance of standard carbon electrodes [399]. This group made the assumption that a thin layer of vanadium oxides is responsible for the charge storage mechanism while the VN is used for fast electron transport, making this material a pertinent material for MSC applications.

The reaction in Equation (17) was proposed to elucidate the charge storage mechanism of the VN films tested in an alkaline KOH electrolyte [399]:

$$V^{4+}O_2 + H_2O + 2\,Ve^- \leftrightarrow V^{3+}OOH + OH^- \quad (17)$$

However, it has been reported that the VN stability in aqueous electrolytes is a major issue, as it can cause a structural change that affects the potential use of energy storage systems [402]. To address this issue, efforts have been made to improve stability and electrochemical performance by adjusting the physicochemical properties during the deposition processes [62,260]. For instance, Jrondi et al. [255] tuned the sputtering deposition process to achieve a high surface capacitance value of 1.4 F cm^{-2}, which demonstrates excellent cycling stability, retaining 90% of the initial capacitance after 150,000 cycles. Additionally, the film exhibits an ultra-high rate capability, with 75% of the initial capacitance maintained at 1.6 V s^{-1} [255].

Ruthenium Nitride

Ruthenium nitride (RuN) electrodes are unexplored for MSC on-chip applications. Studies have shown that RuN electrode films exhibit good electrochemical properties, similar to those of RuO_2 in aqueous electrolytes [53,397]. A recent investigation by the Lethien group [53] sputtered porous RuN films with nanofeather morphology; the RuNelectrode properties were modified through an electrochemical oxidation process (EOP). The RuN nanofeather electrode benefited from the charge transfer at the electrode/electrolyte interface between the hydroxide ions (from the 1 M KOH electrolyte) and the feather-edge amorphous RuO_2 pre-EOP and the h-RuO_2 post-EOP. The electrode demonstrated remarkable performance (3.2 F cm^{-2} and 3200 F cm^{-3}), with only a slight decrease in rate capability (τ < 10 s).

Table 4. Metal nitride electrodes for on-chip MSCs.

Electrode Material	Substrate	Synthesis/Fabrication	Thickness (nm)	Electrolyte	Cell Volt./Pot. Window, V	Areal Cap. mF cm^{-2}	Vol. Cap. F cm^{-3}	Configuration	Ref.
VN	Ta foil	Sputtering/nitridation	400	1 M KOH	0.6	3	75	Single electrode	[401]
VN	Si/Si_3N_4	Sputtering	16,000	1 M KOH	0.6	1200	700	parallel plates	[399]
VN	Si/Si_3N_4	Sputtering	3400	1 M KOH	0.6	220	650	Single electrode	[59]
VN	Si/Si_3N_4	Sputtering	2000	1 M KOH	0.6	40		Interdigitated	[59]
VN	Si/Si_3N_4	Sputtering	32,200	1 M KOH	0.6	1400		Single electrode	[255]
Cr-doped VN	Si	Sputtering	NA	1 M KOH	1	190	NA	Single electrode	[403]
VN-carbon nanosheets	Carbon nanosheets	Nitridation	17,000	PVA-KOH hydrogel	0.9	2046.12	1203.6	Single electrode	[404]
W_2N	Si/Si_3N_4	Sputtering	7900	1 M KOH	0.6	550	700	Single electrode	[395]
Mo_2N	Ti foils	Sputtering	1242	0.5 M Li_2SO_4	0.9	55	722	Single electrode	[405]
RuN	Si	Sputtering	450	1 M KOH	0.9	6	133	Single electrode	[397]
RuN	Si/Si_3N_4	Sputtering	10,000	1 M KOH	0.85	3200	3200	Single electrode	[53]
VWN_z	Si/Si_3N_4	Sputtering	150	1 M KOH	0.6	11.5	700	Single electrode	[406]
TiN	Si	Sputtering	15,600	0.5 M H_2SO_4	0.8	27.3	42.6	parallel plates	[407]
TiN	Si	Sputtering	770	0.5 M K_2SO_4	0.7	12	146.4	Single electrode	[408]
TiVN	Si	Sputtering	270	1 M KOH	1	15	500	Single electrode	[409]
Nb_4 N_5	Nb foil	Electrodeposition	17,400	1 M H_2SO_4	0.6	225.8	72.3	Single electrode	[410]
Nb_4N_5-N-doped carbon	Nb foil	Electrodeposition	17,402	1 M H_2SO_4	1	232.9	133.85	parallel plates	[410]
CrN	Si	Sputtering	1100	0.5 M H_2SO_4	0.8	12.8	116.36	parallel plates	[411]
CrN	Si	Sputtering	2100	0.5 M H_2SO_4	0.8	17.7	83.26	parallel plates	[412]
CrN	Si	Sputtering	1100	0.5 M H_2SO_4	0.8	31.3	284.55	parallel plates	[413]
Mn_3N_2	Stainless steel	Sputtering	NA	1 M KOH	0.9	118	NA	Single electrode	[414]
MoN_x-TiN	Ti foils	Electrodeposition + nitridation	4000	1.0 M LiOH	0.6	121.5	NA	Single electrode	[415]
Co_3N	Si	Sputtering	929	6 M KOH	0.6	79.1	851.4	Single electrode	[416]
CNTs-TiN (3.4/1.2 μm)	Si/amorphous carbon film	CVD + Sputtering	4600	K_2SO_4	0.7	18.13	-	Single electrode	[417]
CNTs-VN (3.4/1.3 μm)	Si/SiO_2	CVD + Sputtering	4700	K_2SO_4	0.5	37.5	-	Single electrode	[214]
CNTs-VN	CNT fibers	Solvothermal	30,000	3 M KOH	1	564	-	Single electrode	[215]

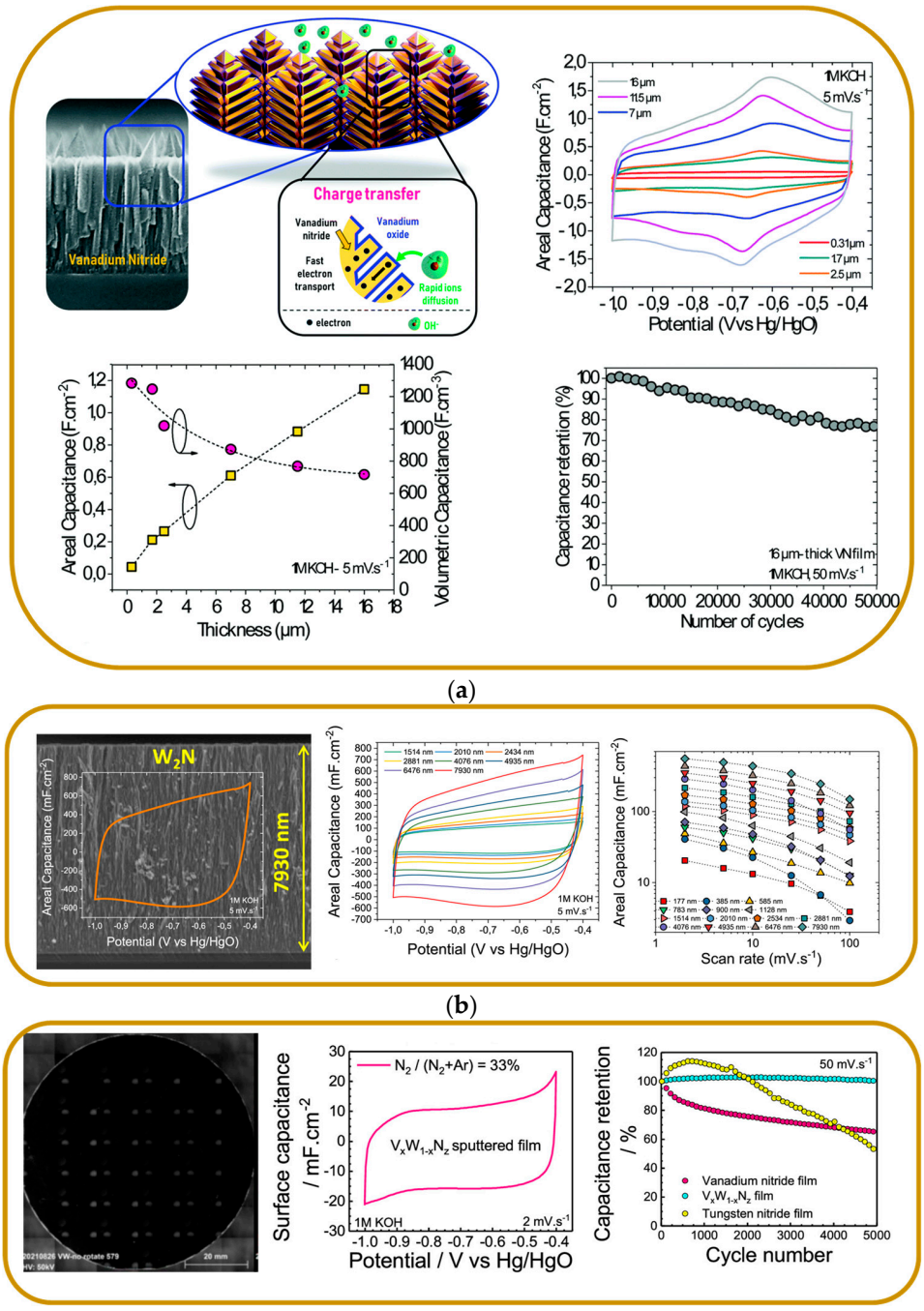

Figure 10. Metal nitride electrode materials for on-chip micro-supercapacitor applications. (**a**) Vanadium nitride electrode films. SEM cross-section images of the sputtered porous VN films with the charge storage process, CV plot of the VN electrode vs. the thickness, evolution of the areal and volumetric capacitances vs. the thickness, and capacitance retention vs. the number of cycles (16 µm-thick film) at 50 mV s^{-1}, respectively. Reproduced with permission from [399]. Copyright (2020), Royal Society of Chemistry. (**b**) Sputtered tungsten nitride films as pseudocapacitive electrodes for on chip micro-supercapacitors. SEM cross-section images of the sputtered W_2N films, CVs of various W_2N film thickness measured at 5 mV s^{-1} in 1 M KOH, and the corresponding areal capacitance, respectively. Reproduced with permission from [395]. Copyright (2019), Elsevier. (**c**) Wafer-scale performance mapping of magnetron-sputtered vanadium tungsten nitride. VWN_z sputtered on silicon wafers, CV plot of the VWN_z films, and film stability in KOH electrolyte, respectively. Reproduced with permission from [406]. Copyright © 2024, American Chemical Society.

Other Binary Nitride Electrodes

Besides the most widely exploited VN-based electrodes, other nitride materials issued from microelectronics can be synthesized/deposited and investigated as electrode materials for on-chip MSC applications. Examples of these metal nitrides are tungsten nitride (WN, W_2N) [395,418], chromium nitride (CrN, Cr_2N) [139,396,411,412], manganese nitride (MnN, Mn_3N_2) [414,419], titanium nitride (TiN) [408,420], molybdenum nitride (MoN) [421] ruthenium nitride (RuN) [397], niobium nitride (NbN) [422], hafnium nitride (HfN) [423], and cobalt nitride (Co_3N) [423]. Wei et al. [411] reported the preparation of CrN thin films by reactive DC magnetron sputtering. The sputtered CrN thin film electrodes achieved a specific areal capacitance of 12.8 mF cm^{-2} at 1.0 mA cm^{-2}, retaining about 92% of the initial capacitance after 20,000 cycles in a 0.5 M H_2SO_4 electrolyte, and fabricated MSCs based on CrN (in a face-to-face configuration) to deliver an energy density of 8.2 mW h cm^{-3} at a power density of 0.7 W cm^{-3} along with outstanding cycling stability. Qi et al. [412] fabricated symmetric MSCs based on porous CrN thin film electrodes deposited by sputtering to obtain a capacitance of 17.7 mF cm^{-2} at a current density of 1.0 mA cm^{-2} in a 0.5 M H_2SO_4 electrolyte, delivering maximum energy and power densities of 7.4 mWh cm^{-3} and 18.2 W cm^{-3}, respectively. Ouendi et al. [395] achieved capacitance values up to 0.55 F cm^{-2}(>700 F cm^{-3}) with sputtered 7.9 µm-thick W_2N films in 1 M KOH aqueous electrolyte (Figure 10b). Sputtered NbN thin film electrodes on silicon substrate demonstrated a volumetric capacitance of 707.1 F cm^{-3} in 0.5 M H_2SO_4 aqueous electrolyte with good cycling stability, recording 92.2% capacitance retention after 20,000 cycles [423]. HfN thin film electrodes deposited by reactive DC magnetron sputtering demonstrated an achieved areal capacitance of 5.6 mF·cm^{-2} at 1.0 mA·cm^{-2} in 0.5 M H_2SO_4 aqueous electrolyte [422]. Sputtered TiN thin films on silicon substrate achieved a volumetric capacitance of 146.4 F cm^{-3}, with outstanding cycling stability over 20,000 cycles [408]. A fabricated MSC based on tailored surface sputtered TiN thin film electrodes achieved energy and power densities of 23 mWh cm^{-3} and 7.4 W cm^{-3}, respectively [420]. Sputtered Mn_3N_2 thin film electrodes were comparatively tested in basic, neutral, and acidic electrolytes, they demonstrated areal capacitance values of 118 mF cm^{-2} for KOH, 68 mF cm^{-2} for KCl, and 27 mF cm^{-2} for Na_2SO_4 at a scan rate of 10 mVs^{-1}. The Mn_3N_2 electrodes indicated better stability in alkaline media than the neutral and acidic electrolytes [414]. These materials are becoming more competitive with VN-based electrodes due to recent concerted efforts to fine-tune their properties to achieve better electrochemical performance.

In addition, the formation of nitride composite (not limited to VN) materials is considered a viable strategy to mitigate against the electrochemical oxidation and the dissolution of the pristine metal nitride materials, usually encountered in aqueous electrolytes, thus enhancing the electrochemical performance and improving the cycle life [402,404,424,425]. Numerous MSCs based on nitride composite electrodes have been exploited with impressive electrochemical performance. Unfortunately, there is a restriction on the on-chip implementation due to the preparation techniques, which are largely not compatible with electronic microfabrication protocols. The common processing routes to obtain the majority of the composites include hydrothermal [404,418,426], a solvothermal process employing nitridation [215,427], and chemical methods [428]. An example is the solvothermal process to prepare VN-CNTs composite electrodes for wearable MSCs application, achieving a specific capacitance of 564 mFcm^{-2} (188 Fcm^{-3}) in a 3 M KOH aqueous electrolyte [215]. Another report of an NV-carbon nanosheet composite (VN-CNS) electrode for MSCs prepared by hydrothermal process demonstrated a high volumetric capacitance of 1203.6 F cm^{-3} at 1.1 A cm^{-3} and a high rate capability of 703.1 F cm^{-3} at 210 A cm^{-3} in 1 M KOH electrolyte, retaining 90% of the initial capacitance after 10,000 cycles [404].

Mixed-Metal Nitride Electrodes

Like mixed-metal oxide electrodes, mixed-metal nitride electrodes are currently receiving notable attention due to the synergy of the participating multivalent metal cations in modifying the properties of their parent compounds to improve electrochemical perfor-

mance. Taking advantage of the processing techniques, especially physical vapor deposition like sputtering techniques that are CMOS compatible, is capable of obtaining thin films on a large wafer. For instance, the electrochemical behavior of VN electrodes is principally due to pseudocapacitive charge storage, exhibiting high areal capacitance [399], while, unlike VN electrodes, TiN appears to be mainly ruled by EDL type, exhibiting high cycling ability [409,420]. The synergistic electrochemical effects of coupling the participating transition metals, in this case, mixed titanium and vanadium (Ti,V)N, have aroused research interest for MSC applications. Achour et al. [409] reported an example of this synergy, using a reactive DC co-sputtering technique to deposit titanium vanadium nitride (TiVN) thin film electrodes with different Ti/V ratios. The results showed that the V-rich electrode sample exhibits a Faradic behavior that limits its cycling ability. Despite a high capacitance of 24 $mFcm^{-2}$ at 2 mVs^{-1}, incorporation of Ti in the film drastically improves the cycling ability, with virtually no fade in capacitance after 10,000 cycles. The Ti-rich electrode exhibits 5 $mFcm^{-2}$, while the TiVN electrode (with a Ti/V ratio close to 1.1) exhibits an areal capacitance value of 15 $mFcm^{-2}$ (500 Fcm^{-3}) at 2 mVs^{-1} in 1 M KOH electrolyte solution. Similarly, a thin film of TiVN deposited on stainless steel substrates by a pulsed DC magnetron sputtering technique was tested with 1 M Na_2SO_4 electrolyte to achieve a volumetric capacitance of 155.94 Fcm^{-3} [424].

In addition, Niobium titanium nitride (NbTiN) thin film electrodes were deposited using the reactive magnetron co-sputtering technique. The electrodes exhibit a specific capacitance of 59.3 mF cm^{-2} at 1.0 mA cm^{-2} (or 154.4 mF cm^{-2} at 100 mV s^{-1}) along with excellent long-term stability (at least 20,000 cycles), superior to that of TiN (26.9 mF cm^{-2} at 1.0 mA cm^{-2}) and NbN (39.6 mF cm^{-2} at 1.0 mA cm^{-2}) electrodes [429]. Dinh et al. [406] investigated the electrochemical properties of sputtered VWN_z on a large silicon wafer in alkali aqueous electrolytes (Figure 10c). The electrode film showed excellent electrochemical performance with a volumetric capacitance of 700 Fcm^{-3} (11.5 mF cm^{-2}) and no loss in capacitance retention after 5000 cycles.

3.2.3. Metal Carbides/Carbonitrides

Transition metal carbides/carbonitrides (MXene) are an emerging class of transition metal-based electrode materials for MSCs applications, having the general formula $M_{n+1}X_nT_x$ ($n = 1$, 2, or 3), where M is an early transition metal (e.g., Sc, Ti, Zr, Hf, V, Nb, Ta, Cr, and Mo), X denotes carbon or nitrogen, and T represents the surface terminations or functional groups (=O, –OH, and/or –F), and x is the number of functional termination groups [430–433]. The unique structures exhibited by MXenes with the inner conductive transition metal carbide layer enable efficient electron transportation, and the hydrophilicity rendered by the transitional metal oxide-like surface functional groups can act as active sites for fast redox reactions and also influence the Fermi level density of the states, thereby electronic properties [432,434]. MXenes are particularly promising because the 2D nature of the nanosheets can facilitate the intercalation of electrolyte ions between adjacent layers and, in the meantime, shorten the ion diffusion paths between positive and negative electrodes [433,434]. Several groups have reported successful synthesis of MXene thin films for MSC applications [434–437].

Titanium carbide MXene ($Ti_3C_2T_x$) has leapt to the forefront and become the most widely studied among the successfully realized MXene family for MSCs applications. This is due to its ultrahigh conductivity (2.4×10^5 S cm^{-1}) [438], good electrochemical properties, having demonstrated an outstanding volumetric capacitance of ≈1500 F cm^{-3} with good rate capability in acidic media [439], and excellent mechanical properties [430]. The Gogotsi group [231] unraveled the charge mechanism exhibited by MXenein aqueous media and observed a change in the interplanar spacing between $Ti_3C_2T_x$ layers, resulting in electrode deformations, i.e., expansion/contraction, which was attributed to the occurrence of spontaneous intercalation of some cations (Li^+, Na^+, Mg^{2+}, K^+, NH_4^+, and Al^{3+}) when MXene samples are exposed to aqueous electrolytes during the cycling process. Electrochemical in situ XAS measurements further detected changes in the Ti oxidation state

during cycling, confirming that the electrochemical behavior of $Ti_3C_2T_x$ is predominantly pseudocapacitive [440]. The group asserted that the spontaneous ion intercalation provides access to electrochemically active transition metal oxide surfaces, with the Ti oxidation state in $Ti_3C_2T_x$ being much closer to +2 than +4, unlike the case in TiO_2 and cubic TiC, while the conductive carbide layer ensures rapid charge transfer. A summary of the electrochemical performance of recently exploited MXene-based on-chip MSCs is presented in Table 5.

$Ti_3C_2T_x$ electrodes are usually prepared via wet etching [434], which is largely compatible with microfabrication protocols and offers a great opportunity for implementation in on-chip MSC applications. MXene-based on-chip MSCs can be achieved through various patterning techniques, either by direct patterning, such as laser scribing or reactive ion etching, of MXene solid on the desired substrate [441,442] or by printing of the MXene ink [430,433]. MXene ($Ti_3C_2T_x$) electrode materials have demonstrated good electrochemical properties in aqueous media.

Table 5. MXene electrodes for on-chip MSCs.

Electrode Material	Substrate	Synthesis/Fabrication	Thickness (nm)	Electrolyte	Areal Cap. mF cm^{-2}	Vol. Cap F cm^{-3}	Energy Density mWh cm^{-3}	Power Density W cm^{-3}	Configuration	Ref.
$Ti_3C_2T_x$	Free-standing	Etching	20,000	1 M KOH	680	340	NA	NA	Single electrode	[231]
$Ti_3C_2T_x$	Free-standing	Etching	12,000	PVA-KOH hydrogel	636	530	NA	NA	Single electrode	[438]
$Ti_3C_2T_x$	Paper	Screen printing	20,000	PVA-H_2SO_4 hydrogel	1108	-	-	-	Intedigitated	[431]
$Ti_3C_2T_x$	3D LIG	direct CO_2 laser-scribing/ lift-off lithography	NA	2 M H_2SO_4	1348	-	-	-	Intedigitated	[230]
$Ti_3C_2T_x$	PET	3D Printing	NA	PVA-H_2SO_4 hydrogel	2337	-	-	-	Intedigitated	[443]
$Ti_3C_2T_x$	Glass	Extrusion 3D Printing	NA	PVA-H_2SO_4 hydrogel	1035	-	1	0.005	Intedigitated	[432]
$Ti_3C_2T_x$	Glass	Spray coating/ laser cutting	1300	PVA-H_2SO_4 hydrogel	27.3	356.8	18	15	Intedigitated	[441]
$Ti_3C_2T_x$	PET	Stamping	690	PVA-H_2SO_4 hydrogel	61	884	44.2	90	Intedigitated	[444]
$Ti_3C_2T_x$	PET	CO2 laser machining + spray coating	4000	PVA-H_3PO_4 hydrogel	23	57.5	2.8	0.744	Intedigitated	[3]
$Ti_3C_2T_x$-Graphene	PET	Spray coating/ Mask-assisted filtration	1000	PVA-H_3PO_4 hydrogel	3.26	33	3.4	0.2	Intedigitated	[445]
$Ti_3C_2T_x$	Paper	Vacuum-assisted filtration/laser printing	2200	PVA-H_2SO_4 hydrogel	27.29	124.05	6.1	0.85	Intedigitated	[446]
$Ti_3C_2T_x$-RuO_2	Paper	Screen printing	270	PVA–KOH hydrogel	23.3	864.2	13.5	48.5	Intedigitated	[433]
$Ti_3C_2T_x$	PET/Au/PDMS	Vacuum-assisted filtration/Laser marking	4000	PVA-H_2SO_4 hydrogel	73	183	12.4	4.38	Intedigitated	[447]
$Ti_3C_2T_x$	Glass	Dip coating/ scalpel engraving	150	PVA-H_3PO_4 hydrogel	0.283	18.9	0.67	6.67	Intedigitated	[435]
$Ti_3C_2T_x$-graphene	Si-SiO_2	Scratch method	5000	PVA-H_3PO_4 hydrogel	18.2	36.4	2.3	0.16	Intedigitated	[448]
$Ti_3C_2T_x$-sodium alginate-Fe^{2+}	Si	Etching/inkjet-printing	730	PVA-H_3PO_4 hydrogel	123.8	1696	85	4.6	Intedigitated	[449]

Jiang et al. [450] fabricated wafer-scale on-chip MXene MSCs for AC-Line filtering applications using a conventional photolithographic lift-off process with 100 nm-thick interdigitated electrodes (Figure 11a) to deliver a volumetric capacitance of 30 F cm^{-3} at 120 Hz and a very short relaxation time constant of 0.45 ms, surpassing conventional electrolytic capacitors of 0.8 ms. The fabricated device is capable of filtering 120 Hz ripples produced by AC line power at a frequency of 60 Hz.

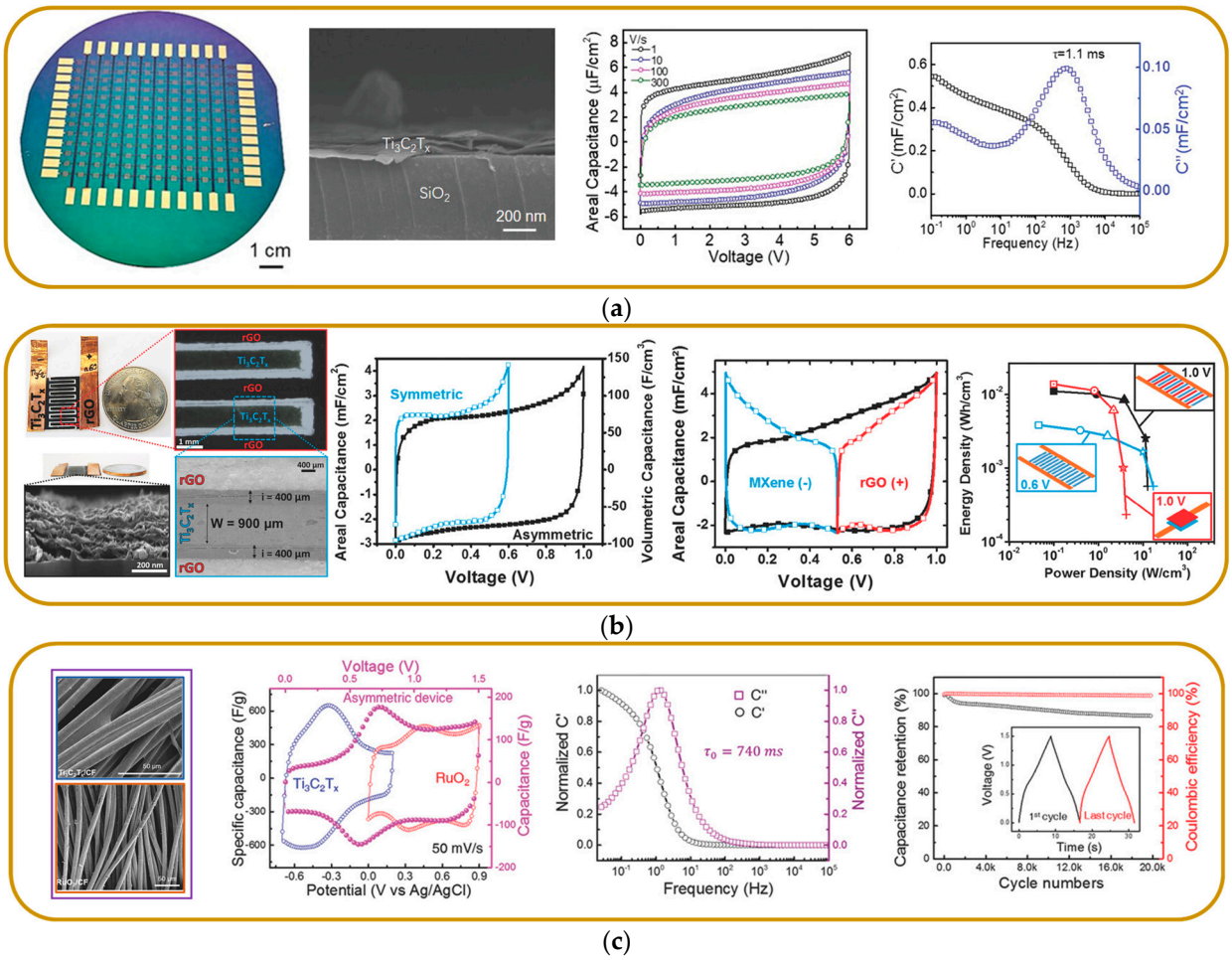

Figure 11. MXene electrode for on-chip micro-supercapacitor applications. (**a**) Wafer scale fabrication of the MXene. Digital photograph showing the wafer scale fabrication of the MXene MSCs, cross-sectional SEM images showing uniform coating of $Ti_3C_2T_x$ on gold, CV plots of $Ti_3C_2T_{x-0.3}$ μm MSCs using PVA/H_3PO_4 gel electrolyte, and C′ and C″ versus frequency, respectively. Reproduced with permission from [450]. Copyright (2019), John Wiley & Sons-Books. (**b**) MXene-rGO asymmetric MSC. Digital photograph of a top-view of the asymmetric MSC device, indicating $Ti_3C_2T_x$ and rGO interdigitated electrode configurations; CVs of the MSC and the individual electrodes recorded at 2 mV s^{-1} in a 3-electrode configuration; comparison between asymmetric interdigitated MSC and all-MXene symmetric interdigitated MSC at 2 mV s^{-1}; Ragone plot of the asymmetric interdigitated MSC, respectively. Reproduced with permission from [136]. Copyright (2017), John Wiley & Sons. (**c**) MXene-RuO_2 asymmetric MSC. Field emission scanning electron microscopy (FSEM) images of $Ti_3C_2T_x$ on carbon fibers (CF) and RuO_2/CF; CVs of RuO_2/CF, $Ti_3C_2T_x$/CF, and the asymmetric device at a scan rate of 50 mV s^{-1}, normalized real (C′) and imaginary (C″) parts of capacitance versus frequency of the device; and cycling stability and Coulombic efficiency of the asymmetric device over 20,000 cycles in 1 m H_2SO_4 electrolyte at a current density of 20 A g^{-1} (inset: the typical charge–discharge profiles for the first and last charge–discharge cycles). Reproduced with permission from [135]. Copyright (2018), John Wiley & Sons.

In a recent study, 3D MXene symmetric MSCs were fabricated using printing techniques [451]. The study leveraged the synergy of a high-voltage "water-in-LiBr" (WiB) gel electrolyte, which has a high voltage window of 1.8 V, and 3D-printed microelectrodes to achieve an ultrahigh areal energy density of 1772 μWh cm^{-2}. However, like other 2D layered materials, MXene nanosheets are prone to self-restacking and agglomeration during electrode microfabrication due to the build-up of van der Waals forces between neighboring nanosheets, leading to a loss of electrochemically active surface to be accessed by electrolyte ions and thus hampering the full utilization of electrochemical reactions [433,452,453]. One of the measures considered to prevent self-restacking is the development of MXene composites by introducing redox-active (such as MnO_2 [454,455] or RuO_2 [433]) or carbon-based [445,456] materials as molecular spacers between the layers to keep the MXene nanosheets separated within the electrodes, thus increasing the accessible electroactive sites and greatly improving the accessibility of electrolyte ions, thereby enhancing the electrochemical performance [433,453,453,457]. Another strategy is the modification of the fabrication process to prevent restacking [431].

Li et al. [433] fabricated MSCs based on $Ti_3C_2T_x$-RuO_2 composite electrode by screen-printing technique to achieve volumetric capacitance of 864.2 F cm^{-3} at 1 mV s^{-1} with PVA–KOH gel electrolyte, having good capacitance retention of 90% after 10,000 cycles and a good rate capability of 304 F cm^{-3} at 2 V s^{-1}. The device achieved a remarkable energy density of 13.5 mWh cm^{-3} and a power density of 48.5 W cm^{-3}. Qin et al. [458] fabricated interdigitated MSCs by conventional photolithography using interconnected porous PEDOT-MXene composite electrodes prepared by electrochemical polymerization (EP). The MSC demonstrated an areal capacitance of 47.4 mF cm^{-2} and a high volumetric energy density of 20.05 mWh cm^{-3}. In another study, Kim et al. [453], fabricated interdigitated MSCs by electron beam lithography and photolithography using $Ti_3C_2T_x$-CNTs composite electrodes to achieve a high areal capacitance of ~317 mF cm^{-2} at a scan rate of 50 mV s^{-1}. Ma et al. [430] fabricated interdigitated MXene-polymer (MXene/poly(3,4-ethylenedioxyth iophene):poly(styrenesulfonic acid) (MXene/poly(3,4-ethylenedioxyth iophene):poly(styrenesulfonic acid) (MP) composite-based MSCs via inkjet printing to deliver a high volumetric capacitance of 754 F cm^{-3} and an energy density of 9.4 mWh cm^{-3} and are considered one of the best performing reported inkjet-printed MSCs to date [179,459–461]. The interdigitated MXene-based MSCs fabricated on a flexible substrate by Zheng et al. [433] via screen printing technique exhibit a remarkably high areal capacitance of 1.1 F cm^{-2} and an energy density of 13.8 μWh cm^{-2} with an aqueous H_2SO_4-PVA gel electrolyte, both of which are considered one of the highest values recorded for MXene-based MSCs.

Furthermore, MXene electrodes have also been combined with other (pseudo)capacitive electrodes in an asymmetric configuration to deliver higher energy density [134,136]. An example was demonstrated by Couly et al. [136] (Figure 11b), combining $Ti_3C_2T_x$ and rGO in a fabricated asymmetric MSC operated at a 1 V voltage window to deliver an energy density of 8.6 mWh cm^{-3} at a power density of 0.2 W cm^{-3}, while retaining 97% of the initial capacitance after 10,000 cycles. Another study combined $Ti_3C_2T_x$ and RuO_2 to increase the cell voltage of symmetric MXene MSCs to about twice their operating voltage window (as shown in Figure 11c). The asymmetric MSCs operated at a voltage window of 1.5 V to deliver an energy density of 37 μW h cm^{-2} at a power density of 40 mW cm^{-2}, with 86% capacitance retention after 20,000 charge–discharge cycles [136].

Zhu et al. [175] took advantage of the synergistic effect of 2D MXene and highly conductive rGO nanosheets to produce an interdigitated laser scribed graphene LSG-MXene (LrGO-MXene) composite electrode (thickness of ~4 μm coated with PVA-H_3PO_4 gel electrolyte) on polyethylene terephthalate (PET) substrate using the laser scribing technique. The device demonstrates outstanding areal capacitance of 2.58 mF cm^{-2} with cycling stability, maintaining > 97.7% of its initial value after 10,000 cycles, and at a power density of 6.2 μW cm^{-2}, it attained a maximum energy density of 170.67 μWh cm^{-2}.

3.2.4. Conducting Polymers

Conducting polymers are equally receiving attention, but a major drawback is their solution-based synthesis. However, 3D conducting polymers prepared through electrodeposition techniques have been reported for on-chip implementation. In addition, the pseudocapacitive properties of the conducting polymers have been explored with other (pseudo)capacitive materials in the form of composite electrodes for MSC applications [462]. Commonly explored conducting polymers for MSC applications include polyaniline (PANI) [463], poly(3,4-ethylene dioxythiophene) (PEDOT) [226], and polypyrrole (PPy) polypyrrole (PPy) [227].

4. Electrolytes

The importance of the electrolytes' role in achieving high-performance MSCs cannot be overemphasized; they are the media that enable the transport of ions in between two electrodes [464]. The conduction of the ions determines the rate at which energy stored in the electrodes can be delivered [464]. Most electrolytes are solutions consisting of salts dissolved in solvents, either water (aqueous) or organic molecules (nonaqueous), and are in a liquid state in the service temperature range [464]. The electrolyte plays a crucial role in transferring charges and balancing charges between the two electrodes [47,465]. It has been reported that developing high-performance active electrode materials is extremely important for increasing the energy and power density of MSCs. Another important factor to consider in improving the specific energy and power, long cycling life, and safety of MSCs is the electrolyte, which determines the final operating voltage of the MSCs [47,465]. The electrode–electrolyte interaction is critically considered in all electrochemical processes, as it influences the electrode–electrolyte interface and the internal structure of active materials. The electrolytes can be classified into various categories, as shown in Figure 12. The details on the electrolyte conductivity, dissociation, and ion transport properties have been reported elsewhere [464,465]. Here, we will briefly mention the most frequently used electrolytes for MSC applications.

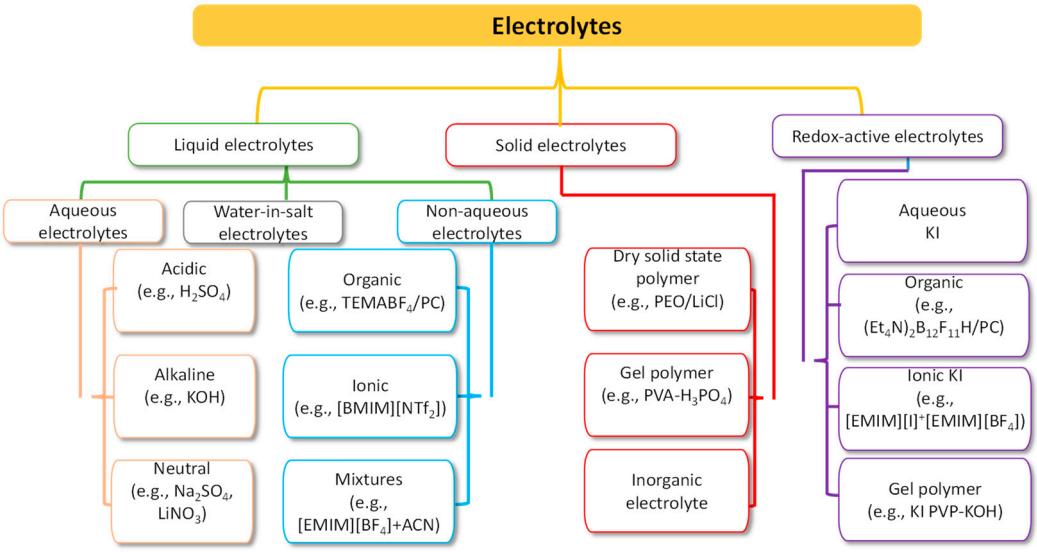

Figure 12. Electrolyte classification for MSC applications [465–468].

4.1. Aqueous Electrolytes (Alkaline, Neutral, and Acidic)

Aqueous electrolytes are known for their ease of handling and exhibit higher conductivity than organic and ionic electrolytes, which is beneficial for lowering the equivalent series resistance (ESR) and improving the power delivery of MSCs [276,465,469]. Aqueous electrolytes fall into three categories: acidic, neutral, and alkaline solutions. However, the narrow potential window, limited to around 1 V due to the water splitting at 1.23 V,

is a major issue in achieving higher energy density. The commonly used aqueous electrolytes are [465] KOH, NaOH, LiOH, Na_2SO_4, H_2SO_4, $(NH_4)_2SO_4$, K_2SO_4, Li_2SO_4, $MgSO_4$, H_3PO_4,$CaSO_4$, $BaSO_4$, KCl, NaCl, LiCl, HCl, CsCl, $CaCl_2$, KNO_3, $LiNO_3$, $Na(CH_3COO)$, $Li(CH_3\text{-}COO)$, $Mg(CH_3COO)_2$, Na_2HPO_4, $NaHCO_3$, $Na_2B_4O_7$, Li-SiW, NaSiW, and K-SiW.

The effects of various electrolyte cations (H^+, Li^+, Na^+, K^+) on the electrochemical performance of MSCs are extensively reviewed by Pal et al., Zhu et al., and Xu et al. [464,465,470]. It has been observed that the hydrated cationic radius influences conductivity and ionic mobility; the hydrated cationic radius is in the order H^+-$H_2O^{\delta-}$ < K^+-$H_2O^{\delta-}$ < Na^+-$H_2O^{\delta-}$ < Li^+-$H_2O^{\delta-}$, as observed by Zhu et al. [470]. The smaller cationic radius gives rise to higher conductivity and ionic mobility, and helps in fast charge transfer, offering more ion adsorption at the electrolyte/electrode interface to further facilitate the fast Faraday reaction [465,470]. The specific capacitance is significantly influenced by cationic mobility, hydrated cationic radius, conductivity, charge/ion exchange, and diffusion [465]. It has also been observed that long-term cycling stability is greatly influenced by the type of cationic species present [470]. In addition, another key player in electrochemical performance is the electrolyte anions (OH^-, SO_4^{2-}, Cl^-, and NO_3^-). Higher conductivity and ionic mobility arise from a smaller ionic radius; an investigation by Wu et al. [471] shows that the hydrated ionic radius is in the order OH^- < Cl^- < NO_3^- < SO_4^{2-}; thus, higher conductivity and ionic mobility anions lead to better capacitive behavior.

4.2. Organic Electrolytes

Organic electrolytes typically consist of organic solvents and conducting salts dissolved in them; they are attractive due to the high voltage window (2.6 to 2.9 V). However, high resistivity is a significant disadvantage due to the large size of molecules, which require a large pore size in the electrodes. Much like aqueous electrolyte-based MSCs, the properties of solvents and salts, such as ion size, ion-solvent interaction, conductivity, and viscosity, significantly impact the performance of MSCs. A comprehensive review of the organic electrolytes, reaction mechanism, and effect of the ionic size of various organic electrolytes used in EDLC and pseudocapacitive devices has been reported elsewhere [465,472].

4.3. Ionic Liquids

Ionic liquids (ILs) are salts of organic cations and organic/inorganic anions with melting points below 100 °C, exhibiting unique structures and properties that make them attractive as alternative electrolytes [473,474]. The physical and chemical properties of the ILs can be tuned through various combinations of cations and anions, and the electrochemical performance of the (pseudo)capacitive electrodes can also be enhanced by tailoring the voltage window and working temperature range [473]. They have potential benefits, including non-flammability, high thermal and electrochemical stability, a high voltage window (>3 V), and low volatility compared to organic electrolytes [465,473]. Commonly used ILs in supercapacitors are based on ammonium, sulfonium, imidazolium, pyrrolidinium, and phosphonium cations and hexafluorophosphate (PF_6), tetrafluoroborate (BF_4), bis(trifluoromethane sulfonyl)imide (TFSI), bis(fluorosulfonyl)imide (FSI), and dicyanamide (DCA) anions [465,473,475–478]. More insight on the ILs for MSCs can be found in refs [465,473].

4.4. Solid-State Electrolytes

Solid-state electrolytes are usually based on polymer electrolytes and have attracted considerable attention in recent years due to the growing demand for on-chip energy storage microdevices, such as MSCs, which leverage their advantages over other electrolytes, such as high ionic conductivity, simple packaging, and leakage-free [465,479–482]. They are typically divided into three types: solid polymer electrolytes (SPEs), gel polymer electrolytes (GPEs) (also called quasi-solid-state electrolytes), and polyelectrolytes. Gel polymer electrolytes have the highest ionic conductivity among them owing to the presence of a liquid phase, making them the preferred choice for MSC applications [465]. On the other

hand, the use of solid polymer electrolytes (SPEs) is limited since they have relatively poor ionic conductivity [482]. However, the high ionic conductivity of gel polymer electrolytes comes with a drawback—they may suffer from narrow operative temperatures due to the presence of water and relatively poor mechanical strength [465,483].

The gel polymer electrolyte is a combination of a polymer host (PEO, PEG, PVA, etc.) and aqueous electrolytes (KOH, H_2SO_4, K_2SO_4, etc.) or a conducting salt dissolved in a solvent [484]. In addition, various polymer hosts have been explored for preparing gel polymer electrolytes such as poly(acrylic acid) (PAA), poly(vinyl alcohol) (PVA), poly(ethyl oxide) (PEO), potassium polyacrylate (PAAK), poly(ether ether ketone) (PEEK), poly-(methylmethacrylate) (PMMA), poly(vinylidene fluoride-co-hexafluoropropylene) (PVDF-HFP), and poly(acrylonitrile)-blockpoly(ethylene glycol)-block-poly(acrylonitrile) (PAN-b-PEG-b-PAN) [465,483]. Hydrogel polymer electrolyte is a gel polymer electrolyte due to the use of water as a plasticizer, involving the combination of aqueous electrolyte and poly host; on the other hand, polymers play host for ionic electrolytes in ionogel electrolytes, aiming to improve the thermal stability and the electrochemically stable potential window [465,484].

4.5. Redox-Active Electrolytes

Redox-active electrolytes are a new class of electrolytes developed to enhance the capacitance of pseudocapacitors through a redox mediator in the electrolyte [146,469,472]. Adding electroactive materials to conventional electrolytes aims to increase their electrochemical performance. More on the redox-active electrolytes can be found in references [146,465,468].

5. Conclusions and Perspectives

In recent years, the development of capacitive materials for on-chip power sources has witnessed significant progress, driven by the demand for miniaturized energy storage solutions with high performance and integration capabilities. This review explores various dielectric materials for electrostatic (micro-/nano-) capacitors, including emerging 2D dielectric and 3D nanostructured materials. It underlines the importance of dielectric materials in influencing the energy density and operational stability of electrostatic (micro-nano-) capacitors. Emerging dielectric materials exhibit unique electrical properties, such as high carrier mobility and tunable bandgaps, which hold promise for next-generation nanocapacitors with enhanced performance and functionality.

Further, various emerging electrode materials for electrochemical micro-supercapacitors (MSCs), including carbon-based materials, transition metal-based materials, and conducting polymers, were examined. Recent advancements in microfabrication processes, doping, and electrode configuration strategies have enhanced electrode materials' performance, paving the way for improved on-chip MSCs. In addition, the preparation of various capacitive materials with a focus on compatibility with on-chip fabrication processes was also examined.

The future development of on-chip energy storage devices, particularly MSCs is poised to significantly impact various industries, notably in the realms of IoT and AI. As technology advances, they are expected to undergo rapid developments in several key areas to enhance their performance, integration capabilities, and application scope. Significant progress is expected in the areas of:

- 2D materials like graphene, MXenes, and transition metal dichalcogenides (TMDs) have a high surface area, excellent electrical conductivity, and tunable properties, affording them the leverage to provide higher energy density and faster charge/discharge cycles.
- 3D material developments using similar 3D templates to fabricate MBs, MSCs, and μ capacitors could be particularly valuable and cost-effective with a streamlined fabrication process, enhancing space efficiency and performance synergy. However, from a technological point of view, some issues may arise, including material compatibility, constraints due to the device's configuration/topology, and fabrication challenges due to the specific requirements.

- Surface area enhancements/topology
- Solid-state electrolytes to offer enhanced safety, ionic conductivity, stability, a wider voltage window to improve energy density, and compatibility with on-chip integration.
- Cycle life improvements by enhancing the active material properties.
- Materials preparation techniques compatible with MEMS technology

There are several potential areas for future research and development in electrode materials for on-chip MSCs. One promising approach is exploring ion implantation strategies, which could lead to improved energy storage performance. These materials have unique properties that could be utilized to overcome current limitations and enable new functionalities in on-chip MSCs. Furthermore, it is essential to develop scalable and cost-effective preparation techniques for electrode materials to facilitate their large-scale production and commercialization. To address compatibility challenges and speed up the translation of research findings into practical applications, innovative approaches such as vacuum deposition techniques should be prioritized.

It is important to tailor the capacitive materials and device architectures to meet the specific requirements to unlock the full potential of the autonomous microelectronics deployed in emerging technologies like the Internet of Things (IoT) and artificial intelligence (AI). This requires continued interdisciplinary research efforts in areas such as materials science, electrochemistry, microfabrication, and device integration.

Author Contributions: B.J. and G.B. performed methodology, investigation, formal analysis, and visualization, wrote, reviewed, and edited the original draft, resources, and data curation. P.R. and C.L. performed resources, conceptualization, methodology, and validation, wrote, reviewed, and edited the original draft, supervision, funding acquisition, and project administration. All authors have read and agreed to the published version of the manuscript.

Funding: This work received funding from Nigerian Government through the Petroleum Technology Development Fund (PTDF)/Campus France and from the French National Research Agency (ARTEMIS project ref ANR-22-ASEN-0001-01).

Conflicts of Interest: The authors declare no conflict of interest.

References

1. Yun, J.; Song, C.; Lee, H.; Park, H.; Jeong, Y.R.; Kim, J.W.; Jin, S.W.; Oh, S.Y.; Sun, L.; Zi, G.; et al. Stretchable Array of High-Performance Micro-Supercapacitors Charged with Solar Cells for Wireless Powering of an Integrated Strain Sensor. *Nano Energy* **2018**, *49*, 644–654. [CrossRef]
2. Guo, R.; Chen, J.; Yang, B.; Liu, L.; Su, L.; Shen, B.; Yan, X.; Guo, R.S.; Chen, J.T.; Yang, B.J.; et al. In-Plane Micro-Supercapacitors for an Integrated Device on One Piece of Paper. *Adv. Funct. Mater.* **2017**, *27*, 1702394. [CrossRef]
3. Jiang, Q.; Wu, C.; Wang, Z.; Wang, A.C.; He, J.H.; Wang, Z.L.; Alshareef, H.N. MXene Electrochemical Microsupercapacitor Integrated with Triboelectric Nanogenerator as a Wearable Self-Charging Power Unit. *Nano Energy* **2018**, *45*, 266–272. [CrossRef]
4. Wang, X.; Yin, Y.; Yi, F.; Dai, K.; Niu, S.; Han, Y.; Zhang, Y.; You, Z. Bioinspired Stretchable Triboelectric Nanogenerator as Energy-Harvesting Skin for Self-Powered Electronics. *Nano Energy* **2017**, *39*, 429–436. [CrossRef]
5. Sudevalayam, S.; Kulkarni, P. Energy Harvesting Sensor Nodes: Survey and Implications. *IEEE Commun. Surv. Tutor.* **2011**, *13*, 443–461. [CrossRef]
6. Lethien, C.; Le Bideau, J.; Brousse, T. Challenges and Prospects of 3D Micro-Supercapacitors for Powering the Internet of Things. *Energy Environ. Sci.* **2019**, *12*, 96–115. [CrossRef]
7. Shen, C.; Xu, S.; Xie, Y.; Sanghadasa, M.; Wang, X.; Lin, L. A Review of On-Chip Micro Supercapacitors for Integrated Self-Powering Systems. *J. Microelectromechanical Syst.* **2017**, *26*, 949–965. [CrossRef]
8. Zheng, S.; Shi, X.; Das, P.; Wu, Z.S.; Bao, X. The Road Towards Planar Microbatteries and Micro-Supercapacitors: From 2D to 3D Device Geometries. *Adv. Mater.* **2019**, *31*, 1900583. [CrossRef] [PubMed]
9. Kyerematen, N.A.; Brousse, T.; Pech, D. Microsupercapacitors as Miniaturized Energy-Storage Components for on-Chip Electronics. *Nat. Nanotechnol.* **2017**, *12*, 7–15. [CrossRef]
10. Spurney, R.G.; Sharma, H.; Pulugurtha, M.R.; Tummala, R.; Lollis, N.; Weaver, M.; Gandhi, S.; Romig, M.; Brumm, H. Ultra-High Density, Thin-Film Tantalum Capacitors with Improved Frequency Characteristics for MHz Switching Power Converters. *J. Electron. Mater.* **2018**, *47*, 5632–5639. [CrossRef]
11. Liu, H.; Zhang, G.; Zheng, X.; Chen, F.; Duan, H. Emerging Miniaturized Energy Storage Devices for Microsystem Applications: From Design to Integration. *Int. J. Extrem. Manuf.* **2020**, *2*, 042001. [CrossRef]

12. Li, Y.; Xiao, S.; Qiu, T.; Lang, X.; Tan, H.; Wang, Y.; Li, Y. Recent Advances on Energy Storage Microdevices: From Materials to Configurations. *Energy Storage Mater.* **2022**, *45*, 741–767. [CrossRef]
13. Liu, L.; Niu, Z.; Chen, J. Design and Integration of Flexible Planar Micro-Supercapacitors. *Nano Res.* **2017**, *10*, 1524–1544. [CrossRef]
14. Hu, H.; Pei, Z.; Ye, C. Recent Advances in Designing and Fabrication of Planar Micro-Supercapacitors for on-Chip Energy Storage. *Energy Storage Mater.* **2015**, *1*, 82–102. [CrossRef]
15. Park, S.H.; Goodall, G.; Kim, W.S. Perspective on 3D-Designed Micro-Supercapacitors. *Mater. Des.* **2020**, *193*, 108797. [CrossRef]
16. Qi, D.; Liu, Y.; Liu, Z.; Zhang, L.; Chen, X.; Qi, D.; Liu, Y.; Liu, Z.; Zhang, L.; Chen, X. Design of Architectures and Materials in In-Plane Micro-Supercapacitors: Current Status and Future Challenges. *Adv. Mater.* **2017**, *29*, 1602802. [CrossRef]
17. Zhang, J.; Zhang, G.; Zhou, T.; Sun, S.; Zhang, J.; Zhou, T.; Zhang, G.; Sun, S. Recent Developments of Planar Micro-Supercapacitors: Fabrication, Properties, and Applications. *Adv. Funct. Mater.* **2020**, *30*, 1910000. [CrossRef]
18. Wu, Z.; Li, L.; Yan, J.M.; Zhang, X.B. Materials Design and System Construction for Conventional and New-Concept Supercapacitors. *Adv. Sci.* **2017**, *4*, 1600382. [CrossRef]
19. Song, W.J.; Yoo, S.; Song, G.; Lee, S.; Kong, M.; Rim, J.; Jeong, U.; Park, S. Recent Progress in Stretchable Batteries for Wearable Electronics. *Batter. Supercaps* **2019**, *2*, 181–199. [CrossRef]
20. Liu, W.; Song, M.S.; Kong, B.; Cui, Y. Flexible and Stretchable Energy Storage: Recent Advances and Future Perspectives. *Adv. Mater.* **2017**, *29*, 1603436. [CrossRef]
21. Zhao, Y.; Guo, J. Development of Flexible Li-Ion Batteries for Flexible Electronics. *InfoMat* **2020**, *2*, 866–878. [CrossRef]
22. Chen, D.; Lou, Z.; Jiang, K.; Shen, G. Device Configurations and Future Prospects of Flexible/Stretchable Lithium-Ion Batteries. *Adv. Funct. Mater.* **2018**, *28*, 1805596. [CrossRef]
23. Jetybayeva, A.; Umirzakov, A.; Uzakbaiuly, B.; Bakenov, Z.; Mukanova, A. Towards Li–S Microbatteries: A Perspective Review. *J. Power Sources* **2023**, *573*, 233158. [CrossRef]
24. Xia, Q.; Zan, F.; Zhang, Q.; Liu, W.; Li, Q.; He, Y.; Hua, J.; Liu, J.; Xu, J.; Wang, J.; et al. All-Solid-State Thin Film Lithium/Lithium-Ion Microbatteries for Powering the Internet of Things. *Adv. Mater.* **2023**, *35*, 2200538. [CrossRef] [PubMed]
25. Hu, B.; Wang, X. Advances in Micro Lithium-Ion Batteries for on-Chip and Wearable Applications. *J. Micromechanics Microengineering* **2021**, *31*, 114002. [CrossRef]
26. Selinis, P.; Farmakis, F. Review—A Review on the Anode and Cathode Materials for Lithium-Ion Batteries with Improved Subzero Temperature Performance. *J. Electrochem. Soc.* **2022**, *169*, 010526. [CrossRef]
27. Yue, C.; Li, J.; Lin, L. Fabrication of Si-Based Three-Dimensional Microbatteries: A Review. *Front. Mech. Eng.* **2017**, *12*, 459–476. [CrossRef]
28. Gao, Y.; Tenhaeff, W.E. Synthesis and Characterization of Thin Film Polyelectrolytes for Solid-State Lithium Microbatteries. *J. Vac. Sci. Technol. B* **2019**, *37*, 051401. [CrossRef]
29. Sheil, R.; Chang, J.P. Synthesis and Integration of Thin Film Solid State Electrolytes for 3D Li-Ion Microbatteries. *J. Vac. Sci. Technol.* **2020**, *38*, 032411. [CrossRef]
30. Jetybayeva, A.; Uzakbaiuly, B.; Mukanova, A.; Myung, S.T.; Bakenov, Z. Recent Advancements in Solid Electrolytes Integrated into All-Solid-State 2D and 3D Lithium-Ion Microbatteries. *J. Mater. Chem. A.* **2021**, *9*, 15140–15178. [CrossRef]
31. Ni, J.; Li, L. Self-Supported 3D Array Electrodes for Sodium Microbatteries. *Adv. Funct. Mater.* **2018**, *28*, 1704880. [CrossRef]
32. Fang, Z.; Wang, J.; Wu, H.; Li, Q.; Fan, S.; Wang, J. Progress and Challenges of Flexible Lithium Ion Batteries. *J. Power Sources* **2020**, *454*, 227932. [CrossRef]
33. Radzuan, R.; Salleh, M.K.M.; Hamzah, M.K.; Zulkefle, H.; Md Sin, N.D.; Rusop, M. Development of Thin Film Capacitors for Power System Applications by PVD Technique. In Proceedings of the SHUSER 2012—2012 IEEE Symposium on Humanities, Science and Engineering Research, Kuala Lumpur, Malaysia, 24–27 June 2012; IEEE: New York, NY, USA, 2012; pp. 1097–1100. [CrossRef]
34. Nguyen, P.; Ng, H.T.; Yamada, Y.; Smith, M.K.; Li, J.; Han, J.; Meyyappan, M.; Lett, N.; Yamada, T.; Chen, Y.P.; et al. High-Dielectric-Constant Silver–Epoxy Composites as Embedded Dielectrics. *Adv. Mater.* **2005**, *17*, 1777–1781. [CrossRef]
35. Özçelik, V.O.; Ciraci, S. High-Performance Planar Nanoscale Dielectric Capacitors. *Phys. Rev. B Condens. Matter Mater. Phys.* **2015**, *91*, 195445. [CrossRef]
36. Yao, S.; Yuan, J.; Mehedi, H.-A.; Gheeraert, E.; Sylvestre, A. Carbon Nanotube Forest Based Electrostatic Capacitor with Excellent Dielectric Performances. *Carbon* **2017**, *116*, 648–654. [CrossRef]
37. Liang, Z.; Liu, M.; Shen, L.; Lu, L.; Ma, C.; Lu, X.; Lou, X.; Jia, C.L. All-Inorganic Flexible Embedded Thin-Film Capacitors for Dielectric Energy Storage with High Performance. *ACS Appl. Mater. Interfaces* **2019**, *11*, 5247–5255. [CrossRef]
38. Tombak, A.; Maria, J.P.; Ayguavives, F.T.; Jin, Z.; Stauf, G.T.; Kingon, A.I.; Mortazawi, A. Voltage-Controlled RF Filters Employing Thin-Film Barium-Strontium-Titanate Tunable Capacitors. *IEEE Trans. Microw. Theory Tech.* **2003**, *51*, 462–467. [CrossRef]
39. Vorobiev, A.; Gevorgian, S. Fabrication of Ferroelectric Components and Devices. In *Ferroelectrics in Microwave Devices, Circuits and Systems: Physics, Modeling, Fabrication and Measurements*; Springer: Berlin/Heidelberg, Germany, 2009; pp. 61–113.
40. Han, K.; Wang, Q. 10.40—Polymers for Thin Film Capacitors: Energy Storage—Li Conducting Polymers. In *Polymer Science: A Comprehensive Reference*; Matyjaszewski, K., Möller, M., Eds.; Elsevier: Amsterdam, The Netherlands, 2012; Volume 1–10, pp. 811–830.

41. Butzen, N.; Krishnarnurthy, H.; Ahmed, Z.; Weng, S.; Ravichandran, K.; Zelikson, M.; Tschanz, J.; Douglas, J. 14.4 A Monolithic 26A/Mm2Imax, 88.5% Peak-Efficiency Continuously Scalable Conversion-Ratio Switched-Capacitor DC-DC Converter. In Proceedings of the Digest of Technical Papers—IEEE International Solid-State Circuits Conference, San Francisco, CA, USA, 19–23 February 2023; IEEE: New York, NY, USA, 2023; Volume 2023, pp. 232–234.
42. Sharma, S.; Chand, P. Supercapacitor and Electrochemical Techniques: A Brief Review. *Results Chem.* **2023**, *5*, 100885. [CrossRef]
43. Bonaccorso, F.; Colombo, L.; Yu, G.; Stoller, M.; Tozzini, V.; Ferrari, A.C.; Ruoff, R.S.; Pellegrini, V. Graphene, Related Two-Dimensional Crystals, and Hybrid Systems for Energy Conversion and Storage. *Science* **2015**, *347*, 1246501. [CrossRef]
44. Chmiola, J.; Celine Largeot, P.L.T.; Simon, P.; Gogotsi, Y. Monolithic Carbide-Derived Carbon Films for Micro-Supercapacitors. *Science* **2010**, *328*, 480–483. [CrossRef]
45. Dinh, K.H.; Roussel, P.; Lethien, C. Advances on Microsupercapacitors: Real Fast Miniaturized Devices toward Technological Dreams for Powering Embedded Electronics? *ACS Omega* **2022**, *8*, 8990. [CrossRef] [PubMed]
46. Huang, C.; Grant, P.S. One-Step Spray Processing of High Power All-Solid-State Supercapacitors. *Sci. Rep.* **2013**, *3*, 2393. [CrossRef] [PubMed]
47. Pandolfo, T.; Ruiz, V.; Sivakkumar, S.; Nerkar, J. General Properties of Electrochemical Capacitors. *Supercapacitors Mater. Syst. Appl.* **2013**, 69–109. [CrossRef]
48. Da Silva, L.M.; Cesar, R.; Moreira, C.M.R.; Santos, J.H.M.; De Souza, L.G.; Pires, B.M.; Vicentini, R.; Nunes, W.; Zanin, H. Reviewing the Fundamentals of Supercapacitors and the Difficulties Involving the Analysis of the Electrochemical Findings Obtained for Porous Electrode Materials. *Energy Storage Mater.* **2020**, *27*, 555–590. [CrossRef]
49. Ceraolo, M.; Lutzemberger, G.; Poli, D. State-Of-Charge Evaluation Of Supercapacitors. *J. Energy Storage* **2017**, *11*, 211–218. [CrossRef]
50. Saha, P.; Dey, S.; Khanra, M. Accurate Estimation of State-of-Charge of Supercapacitor under Uncertain Leakage and Open Circuit Voltage Map. *J. Power Sources* **2019**, *434*, 226696. [CrossRef]
51. Gogotsi, Y.; Simon, P. True Performance Metrics in Electrochemical Energy Storage. *Science* **2011**, *334*, 917–918. [CrossRef]
52. Burke, A. Ultracapacitors: Why, How, and Where Is the Technology. *J. Power Sources* **2000**, *91*, 37–50. [CrossRef]
53. Dinh Khac, H.; Whang, G.; Iadecola, A.; Makhlouf, H.; Barnabé, A.; Teurtrie, A.; Marinova, M.; Huvé, M.; Roch-Jeune, I.; Douard, C.; et al. Nanofeather Ruthenium Nitride Electrodes for Electrochemical Capacitors. *Nat. Mater.* **2024**, *23*, 670–679. [CrossRef]
54. Huang, P.; Lethien, C.; Pinaud, S.; Brousse, K.; Laloo, R.; Turq, V.; Respaud, M.; Demortière, A.; Daffos, B.; Taberna, P.L.; et al. On-Chip and Freestanding Elastic Carbon Films for Micro-Supercapacitors. *Science* **2016**, *351*, 691–695. [CrossRef]
55. Kim, M.S.; Hsia, B.; Carraro, C.; Maboudian, R. Flexible Micro-Supercapacitors with High Energy Density from Simple Transfer of Photoresist-Derived Porous Carbon Electrodes. *Carbon* **2014**, *74*, 163–169. [CrossRef]
56. Beidaghi, M.; Gogotsi, Y. Capacitive Energy Storage in Micro-Scale Devices: Recent Advances in Design and Fabrication of Micro-Supercapacitors. *Energy Environ. Sci.* **2014**, *7*, 867–884. [CrossRef]
57. Chen, F.; Xu, Z.-L. Design and Manufacture of High-Performance Microbatteries: Lithium and Beyond. *Microstructures* **2022**, *2*, 2022012. [CrossRef]
58. Zhu, Z.; Kan, R.; Hu, S.; He, L.; Hong, X.; Tang, H.; Luo, W. Recent Advances in High-Performance Microbatteries: Construction, Application, and Perspective. *Small* **2020**, *16*, 2003251. [CrossRef] [PubMed]
59. Robert, K.; Douard, C.; Demortière, A.; Blanchard, F.; Roussel, P.; Brousse, T.; Lethien, C. On Chip Interdigitated Micro-Supercapacitors Based on Sputtered Bifunctional Vanadium Nitride Thin Films with Finely Tuned Inter- and Intracolumnar Porosities. *Adv. Mater. Technol.* **2018**, *3*, 1800036. [CrossRef]
60. Zhu, C.; Liu, T.; Qian, F.; Han, T.Y.J.; Duoss, E.B.; Kuntz, J.D.; Spadaccini, C.M.; Worsley, M.A.; Li, Y. Supercapacitors Based on Three-Dimensional Hierarchical Graphene Aerogels with Periodic Macropores. *Nano Lett.* **2016**, *16*, 3448–3456. [CrossRef]
61. Manoccio, M.; Esposito, M.; Passaseo, A.; Cuscunà, M.; Tasco, V. Focused Ion Beam Processing for 3d Chiral Photonics Nanostructures. *Micromachines* **2021**, *12*, 6. [CrossRef]
62. Zhang, P.; Wang, F.; Yu, M.; Zhuang, X.; Feng, X. Two-Dimensional Materials for Miniaturized Energy Storage Devices: From Individual Devices to Smart Integrated Systems. *Chem. Soc. Rev.* **2018**, *47*, 7426–7451. [CrossRef]
63. Bao, Z.; Chen, X. Flexible and Stretchable Devices. *Adv. Mater.* **2016**, *28*, 4177–4179. [CrossRef]
64. Strambini, L.; Paghi, A.; Mariani, S.; Sood, A.; Kalliomäki, J.; Järvinen, P.; Toia, F.; Scurati, M.; Morelli, M.; Lamperti, A.; et al. Three-Dimensional Silicon-Integrated Capacitor with Unprecedented Areal Capacitance for on-Chip Energy Storage. *Nano Energy* **2020**, *68*, 104281. [CrossRef]
65. Ulaby, F.T.; Ravaioli, U. *Fundamentals of Applied Electromagnetics*, 8th ed.; Pearson: London, UK, 2023; ISBN 13: 978-1-292-43676-0.
66. Wang, M.; Zhang, J.; Wang, Y.; Lu, Y. Material and Structural Design of Microsupercapacitors. *J. Solid. State Electrochem.* **2022**, *26*, 313–334. [CrossRef]
67. Banerjee, P.; Perez, I.; Henn-Lecordier, L.; Lee, S.B.; Rubloff, G.W. Nanotubular Metal-Insulator-Metal Capacitor Arrays for Energy Storage. *Nat. Nanotechnol.* **2009**, *4*, 292–296. [CrossRef]
68. Jayakrishnan, A.R.; Anina Anju, B.; P Nair, S.K.; Dutta, S.; Silva, J.P.B. Recent Development of Lead-Free Relaxor Ferroelectric and Antiferroelectric Thin Films as Energy Storage Dielectric Capacitors. *J. Eur. Ceram. Soc.* **2024**, *44*, 4332–4349. [CrossRef]
69. Jayakrishnan, A.R.; Silva, J.P.B.; Kamakshi, K.; Dastan, D.; Annapureddy, V.; Pereira, M.; Sekhar, K.C. Are Lead-Free Relaxor Ferroelectric Materials the Most Promising Candidates for Energy Storage Capacitors? *Prog. Mater. Sci.* **2023**, *132*, 101046. [CrossRef]

70. Shim, J.H.; Choi, H.J.; Kim, Y.; Torgersen, J.; An, J.; Lee, M.H.; Prinz, F.B. Process-Property Relationship in High-: K ALD $SrTiO_3$ and $BaTiO_3$: A Review. *J. Mater. Chem. C Mater.* **2017**, *5*, 8000–8013. [CrossRef]
71. Go, D.; Shin, J.W.; Lee, S.; Lee, J.; Yang, B.C.; Won, Y.; Motoyama, M.; An, J. Atomic Layer Deposition for Thin Film Solid-State Battery and Capacitor. *Int. J. Precis. Eng. Manuf. -Green. Technol.* **2023**, *10*, 851–873. [CrossRef]
72. Klootwijk, J.; Kemmeren, A.; Wolters, R.; Roozeboom, F.; Verhoeven, J.; Heuvel, E. van Den Extremely High-Density Capacitors with ALD High-K Dielectric Layers. In *Defects in High-k Gate Dielectric Stacks*; Springer: Heidelberg, Germany, 2006; pp. 17–28.
73. Pan, H.; Li, F.; Liu, Y.; Zhang, Q.; Wang, M.; Lan, S.; Zheng, Y.; Ma, J.; Gu, L.; Shen, Y.; et al. Ultrahigh—Energy Density Lead-Free Dielectric Films via Polymorphic Nanodomain Design. *Science* **2019**, *365*, 578–582. [CrossRef]
74. Liu, Y.; Han, H.; Pan, H.; Lan, S.; Lin, Y.; Ma, J. Enhancement of Breakdown Strength in Relaxor Ferroelectric $Ba(Zr_{0.}3Ti_{0.7})O_3$ Thin Film via Manipulating Growth Oxygen Pressure. *J. Alloys Compd.* **2023**, *937*, 168452. [CrossRef]
75. Lv, P.; Yang, C.; Qian, J.; Wu, H.; Huang, S.; Cheng, X.; Cheng, Z. Flexible Lead-Free Perovskite Oxide Multilayer Film Capacitor Based on $(Na_{0.8}K_{0.2})_{0.5}Bi_{0.5}TiO_3/Ba_{0.5}Sr_{0.5}(Ti_{0.97}Mn_{0.03})O_3$ for High-Performance Dielectric Energy Storage. *Adv. Energy Mater.* **2020**, *10*, 1904229. [CrossRef]
76. Lee, S.W.; Han, J.H.; Kwon, O.S.; Hwang, C.S. Influences of a Crystalline Seed Layer during Atomic Layer Deposition of $SrTiO_3$ Thin Films Using $Ti(O\text{-}IPr)_2(Thd)_2$, $Sr(Thd)_2$, and H_2O. *J. Electrochem. Soc.* **2008**, *155*, G253. [CrossRef]
77. Robertson, J.; Wallace, R.M. High-K Materials and Metal Gates for CMOS Applications. *Mater. Sci. Eng. R Rep.* **2015**, *88*, 1–41. [CrossRef]
78. Jeon, W. Recent Advances in the Understanding of High-k Dielectric Materials Deposited by Atomic Layer Deposition for Dynamic Random-Access Memory Capacitor Applications. *J. Mater. Res.* **2020**, *35*, 775–794. [CrossRef]
79. Smitha, P.S.; Babu, V.S.; Shiny, G. Critical Parameters of High Performance Metal-Insulator-Metal Nanocapacitors: A Review. *Mater. Res. Express* **2019**, *6*, 122003. [CrossRef]
80. Mondal, S.; Pan, T.M. High-Performance $Ni/Lu_2O_3/TaN$ Metal-Insulator-Metal Capacitors. *IEEE Electron. Device Lett.* **2011**, *32*, 1576–1578. [CrossRef]
81. Austin, D.Z.; Allman, D.; Price, D.; Hose, S.; Conley, J.F. Plasma Enhanced Atomic Layer Deposition of Al_2O_3/SiO_2 MIM Capacitors. *IEEE Electron. Device Lett.* **2015**, *36*, 496–498. [CrossRef]
82. Ishikawa, T.; Kodama, D.; Matsui, Y.; Hiratani, M.; Furusawa, T.; Hisamoto, D. High-Capacitance $Cu/Ta_2O_5/Cu$ MIM Structure for SoC Applications Featuring a Single-Mask Add-on Process. In Proceedings of the Technical Digest—International Electron Devices Meeting, San Francisco, CA, USA, 8–11 December 2002; IEEE: New York, NY, USA, 2002; pp. 940–942.
83. Kim, K.D.; Park, M.H.; Kim, H.J.; Kim, Y.J.; Moon, T.; Lee, Y.H.; Hyun, S.D.; Gwon, T.; Hwang, C.S. Ferroelectricity in Undoped-HfO_2 Thin Films Induced by Deposition Temperature Control during Atomic Layer Deposition. *J. Mater. Chem. C Mater.* **2016**, *4*, 6864–6872. [CrossRef]
84. Kambale, K.R.; Mahajan, A.; Butee, S.P.; Kulkarni, A.R.; Venkataramani, N. Effect of Sm_2O_3 Addition on the Dielectric Behaviour of $BaTiO_3$. *Mater. Today Proc.* **2022**, *67*, 404–409. [CrossRef]
85. Khomenkova, L.; Merabet, H.; Chauvat, M.P.; Frilay, C.; Portier, X.; Labbe, C.; Marie, P.; Cardin, J.; Boudin, S.; Rueff, J.M.; et al. Comprehensive Investigation of Er2O3 Thin Films Grown with Different ALD Approaches. *Surf. Interfaces* **2022**, *34*, 102377. [CrossRef]
86. Singh, E.R.; Alam, M.W.; Singh, N.K. Capacitive and RRAM Forming-Free Memory Behavior of Electron-Beam Deposited Ta_2O_5 Thin Film for Nonvolatile Memory Application. *ACS Appl. Electron. Mater.* **2023**, *5*, 3462–3469. [CrossRef]
87. Nam, M.; Lee, S.; Jeong, H.; Yoon, A.; Park, J.S.; Jeon, W. Optimizing the Crystallinity of a ZrO_2 Thin Film Insulator for InGaZnO-Based Metal–Insulator–Semiconductor Capacitors. *Adv. Mater. Interfaces* **2024**, *11*, 2300883. [CrossRef]
88. Lee, D.K.; Kim, H.B.; Kwon, S.H.; Ahn, J.H. Enhanced Electrical Properties of ZrO_2-TiN Based Capacitors by Introducing Ultrathin Metal Oxides. *Mater. Lett.* **2020**, *279*, 128490. [CrossRef]
89. Jeong, J.; Han, Y.; Sohn, H. Effect of La Doping on Dielectric Constant and Tetragonality of ZrO_2 Thin Films Deposited by Atomic Layer Deposition. *J. Alloys Compd.* **2022**, *927*, 166961. [CrossRef]
90. Mehmood, F.; Alcala, R.; Vishnumurthy, P.; Xu, B.; Sachdeva, R.; Mikolajick, T.; Schroeder, U. Reliability Improvement from La_2O_3 Interfaces in $Hf_{0.5}Zr_{0.5}O_2$-Based Ferroelectric Capacitors. *Adv. Mater. Interfaces* **2023**, *10*, 2202151. [CrossRef]
91. Clark, R.D. Emerging Applications for High K Materials in VLSI Technology. *Materials* **2014**, *7*, 2913–2944. [CrossRef]
92. Ho, C.S.; Chang, S.J.; Chen, S.C.; Liou, J.J.; Li, H. A Reliable Si_3N_4/Al_2O_3-HfO_2 Stack MIM Capacitor for High-Voltage Analog Applications. *IEEE Trans. Electron. Devices* **2014**, *61*, 2944–2949. [CrossRef]
93. Patil, S.R.; Barhate, V.N.; Patil, V.S.; Agrawal, K.S.; Mahajan, A.M. The Effect of Post-Deposition Annealing on the Chemical, Structural and Electrical Properties of $Al/ZrO_2/La_2O_3/ZrO_2/Al$ High-k Nanolaminated MIM Capacitors. *J. Mater. Sci. Mater. Electron.* **2022**, *33*, 11227–11235. [CrossRef]
94. Patil, S.R.; Borokar, V.Y.; Rasadujjaman, M.; Zhang, J.; Ding, S.J.; Mahajan, A.M. Investigation of PEALD ZrO_2/La_2O_3-Based High-k Nanolaminates Sandwiched between Al and Ti Electrodes for MIM Capacitors. *J. Mater. Sci. Mater. Electron.* **2023**, *34*, 1284. [CrossRef]
95. Li, S.; Lin, Y.; Li, G.; Yu, H.; Tang, S.; Wu, Y.; Li, X.; Tian, W. Improved Dielectric Properties of La_2O_3–ZrO_2 Bilayer Films for Novel Gate Dielectrics. *Vacuum* **2020**, *178*, 109448. [CrossRef]
96. Ding, S.J.; Hu, H.; Lim, H.F.; Kim, S.J.; Yu, X.F.; Zhu, C.; Li, M.F.; Cho, B.J.; Chan, D.S.H.; Rustagi, S.C.; et al. High-Performance MIM Capacitor Using ALD High-κ HfO 2-Al_2O_3 Laminate Dielectrics. *IEEE Electron. Device Lett.* **2003**, *24*, 730–732. [CrossRef]

97. Jeannot, S.; Bajolet, A.; Manceau, J.P.; Crémer, S.; Deloffre, E.; Oddou, J.P.; Perrot, C.; Benoit, D.; Richard, C.; Bouillon, P.; et al. Toward next High Performances MIM Generation: Up to 30fF/Mm^2 with 3D Architecture and High-k Materials. In Proceedings of the 2007 IEEE Technical Digest—International Electron Devices Meeting International Electron Devices Meeting, Washington, DC, USA, 10–12 December 2007; IEEE: New York, NY, USA, 2007; pp. 997–1000. [CrossRef]
98. Chang, P.; Xie, Y. Evaluation of HfO-Based Ferroelectric Resonant Tunnel Junction by Band Engineering. *IEEE Electron. Device Lett.* **2023**, *44*, 168–171. [CrossRef]
99. Xiong, L.; Hu, J.; Yang, Z.; Li, X.; Zhang, H.; Zhang, G. Dielectric Properties Investigation of Metal–Insulator–Metal (MIM) Capacitors. *Molecules* **2022**, *27*, 3951. [CrossRef] [PubMed]
100. Lee, S.K.; Kim, K.S.; Kim, S.W.; Lee, D.J.; Park, S.J.; Kim, S. Characterizing Voltage Linearity and Leakage Current of High Density $Al_2O_3/HfO_2/Al_2/O_3$ MIM Capacitors. *IEEE Electron. Device Lett.* **2011**, *32*, 384–386. [CrossRef]
101. Park, M.H.; Kim, H.J.; Kim, Y.J.; Moon, T.; Kim, K.D.; Hwang, C.S. Thin HfxZr1-XO_2 Films: A New Lead-Free System for Electrostatic Supercapacitors with Large Energy Storage Density and Robust Thermal Stability. *Adv. Energy Mater.* **2014**, *4*, 1400610. [CrossRef]
102. Kozodaev, M.G.; Chernikova, A.G.; Khakimov, R.R.; Park, M.H.; Markeev, A.M.; Hwang, C.S. La-Doped $Hf_{0.5}Zr_{0.5}O_2$ Thin Films for High-Efficiency Electrostatic Supercapacitors. *Appl. Phys. Lett.* **2018**, *113*, 123902. [CrossRef]
103. Pan, H.; Lan, S.; Xu, S.; Zhang, Q.; Yao, H.; Liu, Y.; Meng, F.; Guo, E.J.; Gu, L.; Yi, D.; et al. Ultrahigh Energy Storage in Superparaelectric Relaxor Ferroelectrics. *Science* **2021**, *374*, 100–104. [CrossRef]
104. Kursumovic, A.; Li, W.W.; Cho, S.; Curran, P.J.; Tjhe, D.H.L.; MacManus-Driscoll, J.L. Lead-Free Relaxor Thin Films with Huge Energy Density and Low Loss for High Temperature Applications. *Nano Energy* **2020**, *71*, 104536. [CrossRef]
105. Fan, Y.; Zhou, Z.; Chen, Y.; Huang, W.; Dong, X. A Novel Lead-Free and High-Performance Barium Strontium Titanate-Based Thin Film Capacitor with Ultrahigh Energy Storage Density and Giant Power Density. *J. Mater. Chem. C Mater.* **2019**, *8*, 50–57. [CrossRef]
106. Liang, Z.; Ma, C.; Shen, L.; Lu, L.; Lu, X.; Lou, X.; Liu, M.; Jia, C.L. Flexible Lead-Free Oxide Film Capacitors with Ultrahigh Energy Storage Performances in Extremely Wide Operating Temperature. *Nano Energy* **2019**, *57*, 519–527. [CrossRef]
107. Hoffmann, M.; Schroeder, U.; Künneth, C.; Kersch, A.; Starschich, S.; Böttger, U.; Mikolajick, T. Ferroelectric Phase Transitions in Nanoscale HfO2 Films Enable Giant Pyroelectric Energy Conversion and Highly Efficient Supercapacitors. *Nano Energy* **2015**, *18*, 154–164. [CrossRef]
108. Lomenzo, P.D.; Chung, C.C.; Zhou, C.; Jones, J.L.; Nishida, T. Doped $Hf_{0.5}Zr_{0.5}O_2$ for High Efficiency Integrated Supercapacitors. *Appl. Phys. Lett.* **2017**, *110*, 232904. [CrossRef]
109. He, Y.; Zheng, G.; Wu, X.; Liu, W.J.; Zhang, D.W.; Ding, S.J. Superhigh Energy Storage Density On-Chip Capacitors with Ferroelectric $Hf_{0.5}Zr_{0.5}O_2$/Antiferroelectric $Hf_{0.25}Zr_{0.75}O_2$ Bilayer Nanofilms Fabricated by Plasma-Enhanced Atomic Layer Deposition. *Nanoscale Adv.* **2022**, *4*, 4648–4657. [CrossRef] [PubMed]
110. Yi, S.H.; Chan, Y.C.; Mo, C.L.; Lin, H.C.; Chen, M.J. Enhancement of Energy Storage for Electrostatic Supercapacitors through Built-in Electric Field Engineering. *Nano Energy* **2022**, *99*, 107342. [CrossRef]
111. Yang, K.; Lee, E.B.; Lee, D.H.; Park, J.Y.; Kim, S.H.; Park, G.H.; Yu, G.T.; Lee, J.I.; Kim, G.H.; Park, M.H. Energy Conversion and Storage Using Artificially Induced Antiferroelectricity in HfO_2/ZrO_2 Nanolaminates. *Compos. B Eng.* **2022**, *236*, 109824. [CrossRef]
112. Haspert, L.C.; Lee, S.B.; Rubloff, G.W. Nanoengineering Strategies for Metal-Insulator-Metal Electrostatic Nanocapacitors. *ACS Nano* **2012**, *6*, 3528–3536. [CrossRef]
113. Hourdakis, E.; Botzakaki, M.A.; Xanthopoulos, N.J. Metal-Insulator-Metal Micro-Capacitors for Integrated Energy Storage up to 105 Hz. *J. Phys. D Appl. Phys.* **2022**, *55*, 455502. [CrossRef]
114. Zhang, Y.; Li, X.; Song, J.; Zhang, S.; Wang, J.; Dai, X.; Liu, B.; Dong, G.; Zhao, L. $AgNbO_3$ Antiferroelectric Film with High Energy Storage Performance. *J. Mater.* **2021**, *7*, 1294–1300. [CrossRef]
115. Ko, E.C.; Kang, W.; Han, J.H. Improved Dielectric Constant and Leakage Current Characteristics of $BaTiO_3$ Thin Film on $SrRuO_3$ Seed Layer. *J. Alloys Compd.* **2022**, *895*, 162579. [CrossRef]
116. Chien, C.S.; Tsai, M.H.; Huang, C.L. Electrical Properties and Current Conduction Mechanisms of $LaGdO_3$ Thin Film by RF Sputtering for RRAM Applications. *J. Asian Ceram. Soc.* **2020**, *8*, 948–956. [CrossRef]
117. Zhang, L.; Pu, Y.; Chen, M.; Peng, X.; Wang, B.; Shang, J. Design Strategies of Perovskite Energy-Storage Dielectrics for next-Generation Capacitors. *J. Eur. Ceram. Soc.* **2023**, *43*, 5713–5747. [CrossRef]
118. Pan, M.J.; Randall, C. A Brief Introduction to Ceramic Capacitors. *IEEE Electr. Insul. Mag.* **2010**, *26*, 44–50. [CrossRef]
119. Ulrich, R.; Schaper, L.; Nelms, D.; Leftwich, M. Comparison of Paraelectric and Ferroelectric Materials for Applications as Dielectrics in Thin Film Integrated Capacitors. *Int. J. Microcircuits Electron. Packag.* **2000**, *23*, 172–181.
120. Dugu, S.; Pavunny, S.P.; Scott, J.F.; Katiyar, R.S. Si:$SrTiO_3$-Al_2O_3-Si:$SrTiO_3$ Multi-Dielectric Architecture for Metal-Insulator-Metal Capacitor Applications. *Appl. Phys. Lett.* **2016**, *109*, 212901. [CrossRef]
121. Nguyen, M.D. Ultrahigh Energy-Storage Performance in Lead-Free BZT Thin-Films by Tuning Relaxor Behavior. *Mater. Res. Bull.* **2021**, *133*, 111072. [CrossRef]
122. Moon, S.; Moon Lee, S.; Lim, H.-K.; Jin, H.-J.; Soo Yun, Y.; Moon, S.; Jin, H.; Lee, S.M.; Lim, H.; Yun, Y.S. Relationship between Multivalent Cation Charge Carriers and Organic Solvents on Nanoporous Carbons in 4 V-Window Magnesium Ion Supercapacitors. *Adv. Energy Mater.* **2021**, *11*, 2101054. [CrossRef]

123. Cabana, J.; Monconduit, L.; Larcher, D.; Palacín, M.R. Beyond Intercalation-Based Li-Ion Batteries: The State of the Art and Challenges of Electrode Materials Reacting through Conversion Reactions. *Adv. Mater.* **2010**, *22*, E170–E192. [CrossRef]
124. Ni, J.; Dai, A.; Yuan, Y.; Li, L.; Lu, J. Three-Dimensional Microbatteries beyond Lithium Ion. *Matter* **2020**, *2*, 1366–1376. [CrossRef]
125. Nasreldin, M.; de Mulatier, S.; Delattre, R.; Ramuz, M.; Djenizian, T. Flexible and Stretchable Microbatteries for Wearable Technologies. *Adv. Mater. Technol.* **2020**, *5*, 2000412. [CrossRef]
126. Tan, H.; Feng, Y.; Rui, X.; Yu, Y.; Huang, S.; Tan, H.T.; Rui, X.H.; Huang, S.M.; Feng, Y.Z.; Yu, Y. Metal Chalcogenides: Paving the Way for High-Performance Sodium/Potassium-Ion Batteries. *Small Methods* **2020**, *4*, 1900563. [CrossRef]
127. Pan, Q.; Tong, Z.; Su, Y.; Qin, S.; Tang, Y.; Pan, Q.G.; Tong, Z.P.; Su, Y.Q.; Qin, S.; Tang, Y.B. Energy Storage Mechanism, Challenge and Design Strategies of Metal Sulfides for Rechargeable Sodium/Potassium-Ion Batteries. *Adv. Funct. Mater.* **2021**, *31*, 2103912. [CrossRef]
128. Buvat, G.; Iadecola, A.; Blanchard, F.; Brousse, T.; Roussel, P.; Lethien, C. A First Outlook of Sputtered FeWO 4 Thin Films for Micro-Supercapacitor Electrodes. *J. Electrochem. Soc.* **2021**, *168*, 030524. [CrossRef]
129. Nunes, W.G.; Freitas, B.G.A.; Beraldo, R.M.; Filho, R.M.; Da Silva, L.M.; Zanin, H. A Rational Experimental Approach to Identify Correctly the Working Voltage Window of Aqueous-Based Supercapacitors. *Sci. Rep.* **2020**, *10*, 19195. [CrossRef]
130. Huang, M.; Li, F.; Dong, F.; Zhang, Y.X.; Zhang, L.L. MnO_2-Based Nanostructures for High-Performance Supercapacitors. *J. Mater. Chem. A Mater.* **2015**, *3*, 21380–21423. [CrossRef]
131. Kumar, A.; Sanger, A.; Kumar, A.; Mishra, Y.K.; Chandra, R. Performance of High Energy Density Symmetric Supercapacitor Based on Sputtered MnO_2 Nanorods. *ChemistrySelect* **2016**, *1*, 3885–3891. [CrossRef]
132. Liu, L.; Zhao, H.; Lei, Y. Advances on Three-Dimensional Electrodes for Micro-Supercapacitors: A Mini-Review. *InfoMat* **2019**, *1*, 74–84. [CrossRef]
133. Yu, M.; Qiu, W.; Wang, F.; Zhai, T.; Fang, P.; Lu, X.; Tong, Y. Three Dimensional Architectures: Design, Assembly and Application in Electrochemical Capacitors. *J. Mater. Chem. A Mater.* **2015**, *3*, 15792–15823. [CrossRef]
134. Xie, Y.; Zhang, H.; Huang, H.; Wang, Z.; Xu, Z.; Zhao, H.; Wang, Y.; Chen, N.; Yang, W. High-Voltage Asymmetric MXene-Based on-Chip Micro-Supercapacitors. *Nano Energy* **2020**, *74*, 104928. [CrossRef]
135. Jiang, Q.; Kurra, N.; Alhabeb, M.; Gogotsi, Y.; Alshareef, H.N. All Pseudocapacitive MXene-RuO_2 Asymmetric Supercapacitors. *Adv. Energy Mater.* **2018**, *8*, 1703043. [CrossRef]
136. Couly, C.; Alhabeb, M.; Van Aken, K.L.; Kurra, N.; Gomes, L.; Navarro-Suárez, A.M.; Anasori, B.; Alshareef, H.N.; Gogotsi, Y. Asymmetric Flexible MXene-Reduced Graphene Oxide Micro-Supercapacitor. *Adv. Electron. Mater.* **2018**, *4*, 1700339. [CrossRef]
137. Xia, C.; Jiang, Q.; Zhao, C.; Beaujuge, P.M.; Alshareef, H.N. Asymmetric Supercapacitors with Metal-like Ternary Selenides and Porous Graphene Electrodes. *Nano Energy* **2016**, *24*, 78–86. [CrossRef]
138. Zhang, Y.; Cao, N.; Szunerits, S.; Addad, A.; Roussel, P.; Boukherroub, R. Fabrication of ZnCoS Nanomaterial for High Energy Flexible Asymmetric Supercapacitors. *Chem. Eng. J.* **2019**, *374*, 347–358. [CrossRef]
139. Adalati, R.; Kumar, A.; Sharma, M.; Chandra, R. Pt Enhanced Capacitive Performance of Cr_2N Electrode toward Flexible Asymmetric Supercapacitor. *Appl. Phys. Lett.* **2021**, *118*, 183901. [CrossRef]
140. Priyadarsini, S.S.; Saxena, S.; Ladole, A.H.; Nehru, D.; Dasgupta, S. Inkjet-Printed Transparent Asymmetric Microsupercapacitors with Mesoporous $NiCo_2O_4$ and Mn_2O_3 Electrodes. *ACS Appl. Energy Mater.* **2024**, *7*, 715–725. [CrossRef]
141. Peng, H.; Ma, G.; Sun, K.; Mu, J.; Luo, M.; Lei, Z. High-Performance Aqueous Asymmetric Supercapacitor Based on Carbon Nanofibers Network and Tungsten Trioxide Nanorod Bundles Electrodes. *Electrochim. Acta* **2014**, *147*, 54–61. [CrossRef]
142. Yang, W.; Zhu, Y.; Jia, Z.; He, L.; Xu, L.; Meng, J.; Tahir, M.; Zhou, Z.; Wang, X.; Mai, L.; et al. Interwoven Nanowire Based On-Chip Asymmetric Microsupercapacitor with High Integrability, Areal Energy, and Power Density. *Adv. Energy Mater.* **2020**, *10*, 2001873. [CrossRef]
143. Shen, K.; Ding, J.; Yang, S.; Shen, K.; Ding, J.W.; Yang, S.B. 3D Printing Quasi-Solid-State Asymmetric Micro-Supercapacitors with Ultrahigh Areal Energy Density. *Adv. Energy Mater.* **2018**, *8*, 1800408. [CrossRef]
144. Ma, B.; Hao, W.; Ruan, W.; Yuan, C.; Wang, Q.; Teng, F. Unveiling Capacitive Behaviors of MoO_2 in Different Electrolytes and Flexible MoO2-Based Asymmetric Micro-Supercapacitor. *J. Energy Storage* **2022**, *52*, 104833. [CrossRef]
145. Asbani, B.; Robert, K.; Roussel, P.; Brousse, T.; Lethien, C. Asymmetric Micro-Supercapacitors Based on Electrodeposited Ruo2 and Sputtered VN Films. *Energy Storage Mater.* **2021**, *37*, 207–214. [CrossRef]
146. Shao, Y.; El-Kady, M.F.; Sun, J.; Li, Y.; Zhang, Q.; Zhu, M.; Wang, H.; Dunn, B.; Kaner, R.B. Design and Mechanisms of Asymmetric Supercapacitors. *Chem. Rev.* **2018**, *118*, 9233–9280. [CrossRef] [PubMed]
147. Zheng, S.; Ma, J.; Wu, Z.S.; Zhou, F.; He, Y.B.; Kang, F.; Cheng, H.M.; Bao, X. All-Solid-State Flexible Planar Lithium Ion Micro-Capacitors. *Energy Environ. Sci.* **2018**, *11*, 2001–2009. [CrossRef]
148. Bai, C.; Zhang, J.; Chen, R.; Wu, W.; Li, X.; Wang, J.; Lu, Y.; Zhao, Y. A 4 V Planar Li-Ion Micro-Supercapacitor with Ultrahigh Energy Density. *ACS Energy Lett.* **2024**, *9*, 410–418. [CrossRef]
149. Zhou, W.; Liu, Z.; Chen, W.; Sun, X.; Luo, M.; Zhang, X.; Li, C.; An, Y.; Song, S.; Wang, K.; et al. A Review on Thermal Behaviors and Thermal Management Systems for Supercapacitors. *Batteries* **2023**, *9*, 128. [CrossRef]
150. Liu, W.; Sun, X.; Yan, X.; Gao, Y.; Zhang, X.; Wang, K.; Ma, Y.; Liu, W.; Sun, X.; Yan, X.; et al. Review of Energy Storage Capacitor Technology. *Batteries* **2024**, *10*, 271. [CrossRef]
151. Li, H.C.; Shen, H.R.; Shi, Y.; Wen, L.; Li, F. Progress and Prospects of Graphene for In-Plane Micro-Supercapacitors. *New Carbon Mater.* **2022**, *37*, 781–801. [CrossRef]

152. Yu, W.; Zhou, H.; Li, B.Q.; Ding, S. 3D Printing of Carbon Nanotubes-Based Microsupercapacitors. *ACS Appl. Mater. Interfaces* **2017**, *9*, 4597–4604. [CrossRef]
153. Kim, S.-K.; Koo, H.-J.; Lee, A.; Braun, P.V.; Kim, S.; Koo, H.; Lee, A.; Braun, P. V Selective Wetting-Induced Micro-Electrode Patterning for Flexible Micro-Supercapacitors. *Adv. Mater.* **2014**, *26*, 5108–5112. [CrossRef]
154. Dousti, B.; Choi, Y., II; Cogan, S.F.; Lee, G.S. A High Energy Density 2D Microsupercapacitor Based on an Interconnected Network of a Horizontally Aligned Carbon Nanotube Sheet. *ACS Appl. Mater. Interfaces* **2020**, *12*, 50011–50023. [CrossRef]
155. Pech, D.; Brunet, M.; Taberna, P.L.; Simon, P.; Fabre, N.; Mesnilgrente, F.; Conédéra, V.; Durou, H. Elaboration of a Microstructured Inkjet-Printed Carbon Electrochemical Capacitor. *J. Power Sources* **2010**, *195*, 1266–1269. [CrossRef]
156. Brousse, K.; Martin, C.; Brisse, A.L.; Lethien, C.; Simon, P.; Taberna, P.L.; Brousse, T. Anthraquinone Modification of Microporous Carbide Derived Carbon Films for On-Chip Micro-Supercapacitors Applications. *Electrochim. Acta* **2017**, *246*, 391–398. [CrossRef]
157. Heon, M.; Lofland, S.; Applegate, J.; Nolte, R.; Cortes, E.; Hettinger, J.D.; Taberna, P.L.; Simon, P.; Huang, P.; Brunet, M.; et al. Continuous Carbide-Derived Carbon Films with High Volumetric Capacitance. *Energy Environ. Sci.* **2010**, *4*, 135–138. [CrossRef]
158. Pech, D.; Brunet, M.; Durou, H.; Huang, P.; Mochalin, V.; Gogotsi, Y.; Taberna, P.L.; Simon, P. Ultrahigh-Power Micrometre-Sized Supercapacitors Based on Onion-like Carbon. *Nat. Nanotechnol.* **2010**, *5*, 651–654. [CrossRef]
159. Kumar, S.; Mukherjee, A.; Telpande, S.; Mahapatra, A.D.; Kumar, P.; Misra, A. Role of the Electrode-Edge in Optically Sensitive Three-Dimensional Carbon Foam-MoS2 Based High-Performance Micro-Supercapacitors. *J. Mater. Chem. A Mater.* **2023**, *11*, 4963–4976. [CrossRef]
160. El-Kady, M.F.; Kaner, R.B. Scalable Fabrication of High-Power Graphene Micro-Supercapacitors for Flexible and on-Chip Energy Storage. *Nat. Commun.* **2013**, *4*, 1475. [CrossRef]
161. Létiche, M.; Brousse, K.; Demortière, A.; Huang, P.; Daffos, B.; Pinaud, S.; Respaud, M.; Chaudret, B.; Roussel, P.; Buchaillot, L.; et al. Sputtered Titanium Carbide Thick Film for High Areal Energy on Chip Carbon-Based Micro-Supercapacitors. *Adv. Funct. Mater.* **2017**, *27*, 1606813. [CrossRef]
162. Eustache, E.; Douard, C.; Retoux, R.; Lethien, C.; Brousse, T.; Eustache, E.; Douard, C.; Brousse, T.; Lethien, C. MnO2 Thin Films on 3D Scaffold: Microsupercapacitor Electrodes Competing with "Bulk" Carbon Electrodes. *Adv. Energy Mater.* **2015**, *5*, 1500680. [CrossRef]
163. Mayorov, A.S.; Gorbachev, R.V.; Morozov, S.V.; Britnell, L.; Jalil, R.; Ponomarenko, L.A.; Blake, P.; Novoselov, K.S.; Watanabe, K.; Taniguchi, T.; et al. Micrometer-Scale Ballistic Transport in Encapsulated Graphene at Room Temperature. *Nano Lett.* **2011**, *11*, 2396–2399. [CrossRef]
164. Beidaghi, M.; Wang, C. Micro-Supercapacitors Based on Interdigital Electrodes of Reduced Graphene Oxide and Carbon Nanotube Composites with Ultrahigh Power Handling Performance. *Adv. Funct. Mater.* **2012**, *22*, 4501–4510. [CrossRef]
165. Xia, J.; Chen, F.; Li, J.; Tao, N. Measurement of the Quantum Capacitance of Graphene. *Nat. Nanotechnol.* **2009**, *4*, 505–509. [CrossRef] [PubMed]
166. El-Kady, M.F.; Strong, V.; Dubin, S.; Kaner, R.B. Laser Scribing of High-Performance and Flexible Graphene-Based Electrochemical Capacitors. *Science* **2012**, *335*, 1326–1330. [CrossRef]
167. Liang, J.; Mondal, A.K.; Wang, D.W.; Iacopi, F. Graphene-Based Planar Microsupercapacitors: Recent Advances and Future Challenges. *Adv. Mater. Technol.* **2019**, *4*, 1800200. [CrossRef]
168. Wu, Z.S.; Parvez, K.; Feng, X.; Müllen, K. Graphene-Based in-Plane Micro-Supercapacitors with High Power and Energy Densities. *Nat. Commun.* **2013**, *4*, 2487. [CrossRef]
169. Niu, Z.; Zhang, L.; Liu, L.; Zhu, B.; Dong, H.; Chen, X. All-Solid-State Flexible Ultrathin Micro-Supercapacitors Based on Graphene. *Adv. Mater.* **2013**, *25*, 4035–4042. [CrossRef] [PubMed]
170. Ye, J.; Tan, H.; Wu, S.; Ni, K.; Pan, F.; Liu, J.; Tao, Z.; Qu, Y.; Ji, H.; Simon, P.; et al. Direct Laser Writing of Graphene Made from Chemical Vapor Deposition for Flexible, Integratable Micro-Supercapacitors with Ultrahigh Power Output. *Adv. Mater.* **2018**, *30*, 1801384. [CrossRef]
171. Velasco, A.; Ryu, Y.K.; Boscá, A.; Ladrón-De-Guevara, A.; Hunt, E.; Zuo, J.; Pedrós, J.; Calle, F.; Martinez, J. Recent Trends in Graphene Supercapacitors: From Large Area to Microsupercapacitors. *Sustain. Energy Fuels* **2021**, *5*, 1235–1254. [CrossRef]
172. Pei, S.; Cheng, H.M. The Reduction of Graphene Oxide. *Carbon* **2012**, *50*, 3210–3228. [CrossRef]
173. Zhu, Y.; Ni, Z.; Gao, J.; Zhang, D.; Wang, S.; Zhao, J. Fabrication of Flexible Planar Micro-Supercapacitors Using Laser Scribed Graphene Electrodes Incorporated with MXene. *J. Phys. Chem. Solids* **2023**, *183*, 111619. [CrossRef]
174. Tarcan, R.; Todor-Boer, O.; Petrovai, I.; Leordean, C.; Astilean, S.; Botiz, I. Reduced Graphene Oxide Today. *J. Mater. Chem. C Mater.* **2020**, *8*, 1198–1224. [CrossRef]
175. Shi, X.; Pei, S.; Zhou, F.; Ren, W.; Cheng, H.M.; Wu, Z.S.; Bao, X. Ultrahigh-Voltage Integrated Micro-Supercapacitors with Designable Shapes and Superior Flexibility. *Energy Environ. Sci.* **2019**, *12*, 1534–1541. [CrossRef]
176. Wang, Y.; Zhao, Y.; Han, Y.; Li, X.; Dai, C.; Zhang, X.; Jin, X.; Shao, C.; Lu, B.; Wang, C.; et al. Fixture-Free Omnidirectional Prestretching Fabrication and Integration of Crumpled in-Plane Micro-Supercapacitors. *Sci. Adv.* **2022**, *8*, eabn8338. [CrossRef]
177. Xiao, H.; Wu, Z.S.; Chen, L.; Zhou, F.; Zheng, S.; Ren, W.; Cheng, H.M.; Bao, X. One-Step Device Fabrication of Phosphorene and Graphene Interdigital Micro-Supercapacitors with High Energy Density. *ACS Nano* **2017**, *11*, 7284–7292. [CrossRef]
178. Chen, M.; Shi, X.; Wang, X.; Liu, H.; Wang, S.; Meng, C.; Liu, Y.; Zhang, L.; Zhu, Y.; Wu, Z.S. Low-Temperature and High-Voltage Planar Micro-Supercapacitors Based on Anti-Freezing Hybrid Gel Electrolyte. *J. Energy Chem.* **2022**, *72*, 195–202. [CrossRef]

179. Li, J.; Sollami Delekta, S.; Zhang, P.; Yang, S.; Lohe, M.R.; Zhuang, X.; Feng, X.; Östling, M. Scalable Fabrication and Integration of Graphene Microsupercapacitors through Full Inkjet Printing. *ACS Nano* **2017**, *11*, 8249–8256. [CrossRef] [PubMed]
180. Zhang, H.; Zhang, X.; Zhang, D.; Sun, X.; Lin, H.; Wang, C.; Ma, Y. One-Step Electrophoretic Deposition of Reduced Graphene Oxide and $Ni(OH)_2$ Composite Films for Controlled Syntheses Supercapacitor Electrodes. *J. Phys. Chem. B* **2013**, *117*, 1616–1627. [CrossRef]
181. Shi, X.; Wu, Z.S.; Qin, J.; Zheng, S.; Wang, S.; Zhou, F.; Sun, C.; Bao, X. Graphene-Based Linear Tandem Micro-Supercapacitors with Metal-Free Current Collectors and High-Voltage Output. *Adv. Mater.* **2017**, *29*, 1703034. [CrossRef] [PubMed]
182. Wang, Y.; Niu, J. Facile Self-Assembly of Exfoliated Graphene/PANI Film for High-Energy Zn-Ion Micro-Supercapacitors. *Molecules* **2023**, *28*, 4470. [CrossRef] [PubMed]
183. Mao, X.; Zhu, L.; Liu, H.; Chen, H.; Ju, P.; Li, W. Synthesis of Graphene via Electrochemical Exfoliation in Different Electrolytes for Direct Electrodeposition of a Cu/Graphene Composite Coating. *RSC Adv.* **2019**, *9*, 35524–35531. [CrossRef]
184. Xiang, L.; Shen, Q.; Zhang, Y.; Bai, W.; Nie, C. One-Step Electrodeposited Ni-Graphene Composite Coating with Excellent Tribological Properties. *Surf. Coat. Technol.* **2019**, *373*, 38–46. [CrossRef]
185. Wuttke, M.; Liu, Z.; Lu, H.; Narita, A.; Müllen, K. Direct Metal-Free Chemical Vapor Deposition of Graphene Films on Insulating Substrates for Micro-Supercapacitors with High Volumetric Capacitance. *Batter. Supercaps* **2019**, *2*, 929–933. [CrossRef]
186. Gupta, N.; Mogera, U.; Kulkarni, G.U. Ultrafast Planar Microsupercapacitor Based on Defect-Free Twisted Multilayer Graphene. *Mater. Res. Bull.* **2022**, *152*, 111841. [CrossRef]
187. Liu, Z.; Chen, Z.; Wang, C.; Wang, H.I.; Wuttke, M.; Wang, X.Y.; Bonn, M.; Chi, L.; Narita, A.; Müllen, K. Bottom-Up, On-Surface-Synthesized Armchair Graphene Nanoribbons for Ultra-High-Power Micro-Supercapacitors. *J. Am. Chem. Soc.* **2020**, *142*, 17881–17886. [CrossRef]
188. Das, P.; Zhang, L.; Zheng, S.; Shi, X.; Li, Y.; Wu, Z.S. Rapid Fabrication of High-Quality Few-Layer Graphene through Gel-Phase Electrochemical Exfoliation of Graphite for High-Energy-Density Ionogel-Based Micro-Supercapacitors. *Carbon* **2022**, *196*, 203–212. [CrossRef]
189. Lin, J.; Peng, Z.; Liu, Y.; Ruiz-Zepeda, F.; Ye, R.; Samuel, E.L.G.; Yacaman, M.J.; Yakobson, B.I.; Tour, J.M. Laser-Induced Porous Graphene Films from Commercial Polymers. *Nat. Commun.* **2014**, *5*, 5714. [CrossRef]
190. Wu, Y.; Chen, J.; Yuan, W.; Zhang, X.; Bai, S.; Chen, Y.; Zhao, B.; Wu, X.; Wang, C.; Huang, H.; et al. Direct Mask-Free Fabrication of Patterned Hierarchical Graphene Electrode for on-Chip Micro-Supercapacitors. *J. Mater. Sci. Technol.* **2023**, *143*, 12–19. [CrossRef]
191. Bellani, S.; Petroni, E.; Del Rio Castillo, A.E.; Curreli, N.; Martín-García, B.; Oropesa-Nuñez, R.; Prato, M.; Bonaccorso, F. Scalable Production of Graphene Inks via Wet-Jet Milling Exfoliation for Screen-Printed Micro-Supercapacitors. *Adv. Funct. Mater.* **2019**, *29*, 1807659. [CrossRef]
192. Cao, C.; Zhou, Y.; Ubnoske, S.; Zang, J.; Cao, Y.; Henry, P.; Parker, C.B.; Glass, J.T. Highly Stretchable Supercapacitors via Crumpled Vertically Aligned Carbon Nanotube Forests. *Adv. Energy Mater.* **2019**, *9*, 1900618. [CrossRef]
193. He, P.; Ding, Z.; Zhao, X.; Liu, J.; Huang, Q.; Peng, J.; Fan, L.Z. Growth of Carbon Nanosheets on Carbon Nanotube Arrays for the Fabrication of Three-Dimensional Micro-Patterned Supercapacitors. *Carbon* **2019**, *155*, 453–461. [CrossRef]
194. Dinh, T.M.; Achour, A.; Vizireanu, S.; Dinescu, G.; Nistor, L.; Armstrong, K.; Guay, D.; Pech, D. Hydrous RuO_2/Carbon Nanowalls Hierarchical Structures for All-Solid-State Ultrahigh-Energy-Density Micro-Supercapacitors. *Nano Energy* **2014**, *10*, 288–294. [CrossRef]
195. Ye, R.; James, D.K.; Tour, J.M. Laser-Induced Graphene: From Discovery to Translation. *Adv. Mater.* **2019**, *31*, 1803621. [CrossRef]
196. Wang, S.; Wu, Z.S.; Zheng, S.; Zhou, F.; Sun, C.; Cheng, H.M.; Bao, X. Scalable Fabrication of Photochemically Reduced Graphene-Based Monolithic Micro-Supercapacitors with Superior Energy and Power Densities. *ACS Nano* **2017**, *11*, 4283–4291. [CrossRef]
197. Zhou, F.; Huang, H.; Xiao, C.; Zheng, S.; Shi, X.; Qin, J.; Fu, Q.; Bao, X.; Feng, X.; Müllen, K.; et al. Electrochemically Scalable Production of Fluorine-Modified Graphene for Flexible and High-Energy Ionogel-Based Microsupercapacitors. *J. Am. Chem. Soc.* **2018**, *140*, 8198–8205. [CrossRef]
198. Rao, Y.; Yuan, M.; Gao, B.; Li, H.; Yu, J.; Chen, X. Laser-Scribed Phosphorus-Doped Graphene Derived from Kevlar Textile for Enhanced Wearable Micro-Supercapacitor. *J. Colloid. Interface Sci.* **2023**, *630*, 586–594. [CrossRef]
199. Wu, Z.S.; Tan, Y.Z.; Zheng, S.; Wang, S.; Parvez, K.; Qin, J.; Shi, X.; Sun, C.; Bao, X.; Feng, X.; et al. Bottom-Up Fabrication of Sulfur-Doped Graphene Films Derived from Sulfur-Annulated Nanographene for Ultrahigh Volumetric Capacitance Micro-Supercapacitors. *J. Am. Chem. Soc.* **2017**, *139*, 4506–4512. [CrossRef] [PubMed]
200. Yuan, M.; Wang, Z.; Rao, Y.; Wang, Y.; Gao, B.; Yu, J.; Li, H.; Chen, X. Laser Direct Writing O/N/S Co-Doped Hierarchically Porous Graphene on Carboxymethyl Chitosan/Lignin-Reinforced Wood for Boosted Microsupercapacitor. *Carbon* **2023**, *202*, 296–304. [CrossRef]
201. El-Kady, M.F.; Ihns, M.; Li, M.; Hwang, J.Y.; Mousavi, M.F.; Chaney, L.; Lech, A.T.; Kaner, R.B. Engineering Three-Dimensional Hybrid Supercapacitors and Microsupercapacitors for High-Performance Integrated Energy Storage. *Proc. Natl. Acad. Sci. USA* **2015**, *112*, 4233–4238. [CrossRef]
202. Zhai, S.; Wang, C.; Karahan, H.E.; Wang, Y.; Chen, X.; Sui, X.; Huang, Q.; Liao, X.; Wang, X.; Chen, Y. Nano-RuO2-Decorated Holey Graphene Composite Fibers for Micro-Supercapacitors with Ultrahigh Energy Density. *Small* **2018**, *14*, 1800582. [CrossRef]
203. Gao, M.; Dong, X.; Wang, K.; Duan, W.; Sun, X.; Zhu, C.; Wang, W. Laser Direct Preparation and Processing of Graphene/MnO Nanocomposite Electrodes for Microsupercapacitors. *J. Energy Storage* **2021**, *33*, 102162. [CrossRef]

204. Lee, H.U.; Kim, S.W. Pen Lithography for Flexible Microsupercapacitors with Layer-by-Layer Assembled Graphene Flake/PEDOT Nanocomposite Electrodes. *J. Mater. Chem. A Mater.* **2017**, *5*, 13581–13590. [CrossRef]
205. Chen, Y.; Guo, M.; Xu, L.; Cai, Y.; Tian, X.; Liao, X.; Wang, Z.; Meng, J.; Hong, X.; Mai, L. In-Situ Selective Surface Engineering of Graphene Micro-Supercapacitor Chips. *Nano Res.* **2022**, *15*, 1492–1499. [CrossRef]
206. Yao, B.; Chandrasekaran, S.; Zhang, H.; Ma, A.; Kang, J.; Zhang, L.; Lu, X.; Qian, F.; Zhu, C.; Duoss, E.B.; et al. 3D-Printed Structure Boosts the Kinetics and Intrinsic Capacitance of Pseudocapacitive Graphene Aerogels. *Adv. Mater.* **2020**, *32*, 1906652. [CrossRef]
207. Wu, C.; Zhang, Z.; Chen, Z.; Jiang, Z.; Li, H.; Cao, H.; Liu, Y.; Zhu, Y.; Fang, Z.; Yu, X. Rational Design of Novel Ultra-Small Amorphous Fe_2O_3 Nanodots/Graphene Heterostructures for All-Solid-State Asymmetric Supercapacitors. *Nano Res.* **2021**, *14*, 953–960. [CrossRef]
208. Zhang, H.; Zhang, Z.; Qi, X.; Yu, J.; Cai, J.; Yang, Z. Manganese Monoxide/Biomass-Inherited Porous Carbon Nanostructure Composite Based on the High Water-Absorbent Agaric for Asymmetric Supercapacitor. *ACS Sustain. Chem. Eng.* **2019**, *7*, 4284–4294. [CrossRef]
209. Lin, J.; Zhang, C.; Yan, Z.; Zhu, Y.; Peng, Z.; Hauge, R.H.; Natelson, D.; Tour, J.M. 3-Dimensional Graphene Carbon Nanotube Carpet-Based Microsupercapacitors with High Electrochemical Performance. *Nano Lett.* **2013**, *13*, 72–78. [CrossRef] [PubMed]
210. Ghosh, A.; Le, V.T.; Bae, J.J.; Lee, Y.H. TLM-PSD Model for Optimization of Energy and Power Density of Vertically Aligned Carbon Nanotube Supercapacitor. *Sci. Rep.* **2013**, *3*, 2939. [CrossRef]
211. Hsia, B.; Marschewski, J.; Wang, S.; In, J.B.; Carraro, C.; Poulikakos, D.; Grigoropoulos, C.P.; Maboudian, R. Highly Flexible, All Solid-State Micro-Supercapacitors from Vertically Aligned Carbon Nanotubes. *Nanotechnology* **2014**, *25*, 055401. [CrossRef]
212. Baughman, R.H.; Zakhidov, A.A.; De Heer, W.A. Carbon Nanotubes—The Route toward Applications. *Science* **2002**, *297*, 787–792. [CrossRef]
213. Zhu, S.; Ni, J.; Li, Y. Carbon Nanotube-Based Electrodes for Flexible Supercapacitors. *Nano Res.* **2020**, *13*, 1825–1841. [CrossRef]
214. Ouldhamadouche, N.; Achour, A.; Lucio-Porto, R.; Islam, M.; Solaymani, S.; Arman, A.; Ahmadpourian, A.; Achour, H.; Le Brizoual, L.; Djouadi, M.A.; et al. Electrodes Based on Nano-Tree-like Vanadium Nitride and Carbon Nanotubes for Micro-Supercapacitors. *J. Mater. Sci. Technol.* **2018**, *34*, 976–982. [CrossRef]
215. Guo, J.; Zhang, Q.; Sun, J.; Li, C.; Zhao, J.; Zhou, Z.; He, B.; Wang, X.; Man, P.; Li, Q.; et al. Direct Growth of Vanadium Nitride Nanosheets on Carbon Nanotube Fibers as Novel Negative Electrodes for High-Energy-Density Wearable Fiber-Shaped Asymmetric Supercapacitors. *J. Power Sources* **2018**, *382*, 122–127. [CrossRef]
216. Pitkänen, O.; Järvinen, T.; Cheng, H.; Lorite, G.S.; Dombovari, A.; Rieppo, L.; Talapatra, S.; Duong, H.M.; Tóth, G.; Juhász, K.L.; et al. On-Chip Integrated Vertically Aligned Carbon Nanotube Based Super- and Pseudocapacitors. *Sci. Rep.* **2017**, *7*, 16594. [CrossRef] [PubMed]
217. Zhang, H.; Wang, B.; Brown, B. Area-Selective Atomic Layer Deposition of Titanium Oxide and Nitride on Vertically Aligned Carbon Nanotubes Patterned by Aerosol Jet Printing for 3D Microsupercapacitors. *J. Power Sources* **2022**, *551*, 232154. [CrossRef]
218. Presser, V.; Heon, M.; Gogotsi, Y. Carbide-Derived Carbons—from Porous Networks to Nanotubes and Graphene. *Adv. Funct. Mater.* **2011**, *21*, 810–833. [CrossRef]
219. Huang, P.; Heon, M.; Pech, D.; Brunet, M.; Taberna, P.L.; Gogotsi, Y.; Lofland, S.; Hettinger, J.D.; Simon, P. Micro-Supercapacitors from Carbide Derived Carbon (CDC) Films on Silicon Chips. *J. Power Sources* **2013**, *225*, 240–244. [CrossRef]
220. Cheng, K.Y.; Bijukumar, D.; Runa, M.; McNallan, M.; Mathew, M. Tribocorrosion Aspects of Implant Coatings: Hip Replacements. In *Tribocorrosion: Fundamentals, Methods, and Materials*; Academic Press: Cambridge, MA, USA, 2021; pp. 93–126.
221. Forouzandeh, P.; Kumaravel, V.; Pillai, S.C. Electrode Materials for Supercapacitors: A Review of Recent Advances. *Catalysts* **2020**, *10*, 969. [CrossRef]
222. Jiang, Y.; Liu, J. Definitions of Pseudocapacitive Materials: A Brief Review. *Energy Environ. Mater.* **2019**, *2*, 30–37. [CrossRef]
223. Liu, J.; Wang, J.; Xu, C.; Jiang, H.; Li, C.; Zhang, L.; Lin, J.; Shen, Z.X. Advanced Energy Storage Devices: Basic Principles, Analytical Methods, and Rational Materials Design. *Adv. Sci.* **2018**, *5*, 1700322. [CrossRef]
224. Conway, B.E. Two-Dimensional and Quasi-Two-Dimensional Isotherms for Li Intercalation and Upd Processes at Surfaces. *Electrochim. Acta* **1993**, *38*, 1249–1258. [CrossRef]
225. Huang, C.; Zhang, W.; Zheng, W. The Debut and Spreading the Landscape for Excellent Vacancies-Promoted Electrochemical Energy Storage of Nano-Architected Molybdenum Oxides. *Mater. Today Energy* **2022**, *30*, 101154. [CrossRef]
226. Diao, Y.; Lu, Y.; Yang, H.; Wang, H.; Chen, H.; D'Arcy, J.M. Direct Conversion of Fe_2O_3 to 3D Nanofibrillar PEDOT Microsupercapacitors. *Adv. Funct. Mater.* **2020**, *30*, 2003394. [CrossRef]
227. Sung, J.H.; Kim, S.J.; Lee, K.H. Fabrication of Microcapacitors Using Conducting Polymer Microelectrodes. *J. Power Sources* **2003**, *124*, 343–350. [CrossRef]
228. Wang, X.; Myers, B.D.; Yan, J.; Shekhawat, G.; Dravid, V.; Lee, P.S. Manganese Oxide Micro-Supercapacitors with Ultra-High Areal Capacitance. *Nanoscale* **2013**, *5*, 4119–4122. [CrossRef]
229. Choi, C.; Robert, K.; Whang, G.; Roussel, P.; Lethien, C.; Dunn, B. Photopatternable Hydroxide Ion Electrolyte for Solid-State Micro-Supercapacitors. *Joule* **2021**, *5*, 2466–2478. [CrossRef]
230. Lei, Y.; Zhao, W.; Zhu, Y.; Buttner, U.; Dong, X.; Alshareef, H.N. Three-Dimensional Ti3C2Tx MXene-Prussian Blue Hybrid Microsupercapacitors by Water Lift-Off Lithography. *ACS Nano* **2022**, *16*, 1974–1985. [CrossRef] [PubMed]

231. Lukatskaya, M.R.; Mashtalir, O.; Ren, C.E.; Dall'Agnese, Y.; Rozier, P.; Taberna, P.L.; Naguib, M.; Simon, P.; Barsoum, M.W.; Gogotsi, Y. Cation Intercalation and High Volumetric Capacitance of Two-Dimensional Titanium Carbide. *Science* **2013**, *341*, 1502–1505. [CrossRef] [PubMed]
232. Feng, J.; Sun, X.; Wu, C.; Peng, L.; Lin, C.; Hu, S.; Yang, J.; Xie, Y. Metallic Few-Layered VS2 Ultrathin Nanosheets: High Two-Dimensional Conductivity for in-Plane Supercapacitors. *J. Am. Chem. Soc.* **2011**, *133*, 17832–17838. [CrossRef] [PubMed]
233. Wang, X.; Zhang, Y.; Zheng, J.; Liu, X.; Meng, C. Hydrothermal Synthesis of VS4/CNTs Composite with Petal-Shape Structures Performing a High Specific Capacity in a Large Potential Range for High-Performance Symmetric Supercapacitors. *J. Colloid. Interface Sci.* **2019**, *554*, 191–201. [CrossRef]
234. Guo, Z.; Yang, L.; Wang, W.; Cao, L.; Dong, B. Ultrathin VS2 Nanoplate with In-Plane and out-of-Plane Defects for an Electrochemical Supercapacitor with Ultrahigh Specific Capacitance. *J. Mater. Chem. A Mater.* **2018**, *6*, 14681–14688. [CrossRef]
235. Karade, S.S.; Banerjee, K.; Majumder, S.; Sankapal, B.R. Novel Application of Non-Aqueous Chemical Bath Deposited Sb_2S_3 Thin Films as Supercapacitive Electrode. *Int. J. Hydrogen Energy* **2016**, *41*, 21278–21285. [CrossRef]
236. Jolayemi, B.; Buvat, G.; Brousse, T.; Roussel, P.; Lethien, C. Sputtered $(Fe,Mn)_3O_4$ Spinel Oxide Thin Films for Micro-Supercapacitor. *J. Electrochem. Soc.* **2022**, *169*, 110524. [CrossRef]
237. Gogotsi, Y.; Penner, R.M. Energy Storage in Nanomaterials—Capacitive, Pseudocapacitive, or Battery-Like? *ACS Nano* **2018**, *12*, 2081–2083. [CrossRef]
238. Nguyen, T.; De Fátima Montemor, M.; Nguyen, T.; Montemor, M.F. Metal Oxide and Hydroxide–Based Aqueous Supercapacitors: From Charge Storage Mechanisms and Functional Electrode Engineering to Need-Tailored Devices. *Adv. Sci.* **2019**, *6*, 1801797. [CrossRef]
239. Huang, T.; Jiang, K.; Chen, D.; Shen, G. Recent Progress and Perspectives of Metal Oxides Based On-Chip Microsupercapacitors. *Chin. Chem. Lett.* **2018**, *29*, 553–563. [CrossRef]
240. Nithya, V.D.; Arul, N.S. Review on α-Fe_2O_3 Based Negative Electrode for High Performance Supercapacitors. *J. Power Sources* **2016**, *327*, 297–318. [CrossRef]
241. Brousse, K.; Pinaud, S.; Nguyen, S.; Fazzini, P.F.; Makarem, R.; Josse, C.; Thimont, Y.; Chaudret, B.; Taberna, P.L.; Respaud, M.; et al. Facile and Scalable Preparation of Ruthenium Oxide-Based Flexible Micro-Supercapacitors. *Adv. Energy Mater.* **2020**, *10*, 1903136. [CrossRef]
242. Guan, M.; Wang, Q.; Zhang, X.; Bao, J.; Gong, X.; Liu, Y. Two-Dimensional Transition Metal Oxide and Hydroxide-Based Hierarchical Architectures for Advanced Supercapacitor Materials. *Front. Chem.* **2020**, *8*, 390. [CrossRef]
243. Liu, C.; Li, Z.; Zhang, Z. MoOx Thin Films Deposited by Magnetron Sputtering as an Anode for Aqueous Micro-Supercapacitors. *Sci. Technol. Adv. Mater.* **2013**, *14*, 065005. [CrossRef]
244. Kim, J.Y.; Lee, S.H.; Yan, Y.; Oh, J.; Zhu, K. Controlled Synthesis of Aligned Ni-NiO Core-Shell Nanowire Arrays on Glass Substrates as a New Supercapacitor Electrode. *RSC Adv.* **2012**, *2*, 8281–8285. [CrossRef]
245. Geramifard, N.; Chakraborty, B.; Dousti, B.; Lee, G.S.; Maeng, J. High-Energy-Density Sputtered Iridium Oxide Micro-Supercapacitors Operating in Physiological Electrolytes. *J. Electrochem. Soc.* **2022**, *169*, 050508. [CrossRef]
246. Deng, W.; Ji, X.; Chen, Q.; Banks, C.E. Electrochemical Capacitors Utilising Transition Metal Oxides: An Update of Recent Developments. *RSC Adv.* **2011**, *1*, 1171–1178. [CrossRef]
247. Hota, M.K.; Jiang, Q.; Mashraei, Y.; Salama, K.N.; Alshareef, H.N. Fractal Electrochemical Microsupercapacitors. *Adv. Electron. Mater.* **2017**, *3*, 1700185. [CrossRef]
248. Wang, Y.T.; Lu, A.H.; Zhang, H.L.; Li, W.C. Synthesis of Nanostructured Mesoporous Manganese Oxides with Three-Dimensional Frameworks and Their Application in Supercapacitors. *J. Phys. Chem. C* **2011**, *115*, 5413–5421. [CrossRef]
249. Han, Z.J.; Pineda, S.; Murdock, A.T.; Seo, D.H.; Ostrikov, K.K.; Bendavid, A. RuO_2-Coated Vertical Graphene Hybrid Electrodes for High-Performance Solid-State Supercapacitors. *J. Mater. Chem. A Mater.* **2017**, *5*, 17293–17301. [CrossRef]
250. Bounor, B.; Asbani, B.; Douard, C.; Favier, F.; Brousse, T.; Lethien, C. On Chip MnO_2-Based 3D Micro-Supercapacitors with Ultra-High Areal Energy Density. *Energy Storage Mater.* **2021**, *38*, 520–527. [CrossRef]
251. Asbani, B.; Buvat, G.; Freixas, J.; Huvé, M.; Troadec, D.; Roussel, P.; Brousse, T.; Lethien, C. Ultra-High Areal Capacitance and High Rate Capability RuO_2 Thin Film Electrodes for 3D Micro-Supercapacitors. *Energy Storage Mater.* **2021**, *42*, 259–267. [CrossRef]
252. Bounor, B.; Asbani, B.; Douard, C.; Deresmes, D.; Stiévenard, D.; Roussel, P.; Favier, F.; Lethien, C.; Brousse, T. Nanostructured MnO2 Films for 3D Micro-Supercapacitors: From New Insights of the Growth Mechanism to the Fine Tuning of Areal Capacitance Values. *J. Electrochem. Soc.* **2023**, *170*, 030530. [CrossRef]
253. Wei, W.; Cui, X.; Chen, W.; Ivey, D.G. Manganese Oxide-Based Materials as Electrochemical Supercapacitor Electrodes. *Chem. Soc. Rev.* **2011**, *40*, 1697–1721. [CrossRef] [PubMed]
254. Tiwari, J.N.; Tiwari, R.N.; Kim, K.S. Zero-Dimensional, One-Dimensional, Two-Dimensional and Three-Dimensional Nanostructured Materials for Advanced Electrochemical Energy Devices. *Prog. Mater. Sci.* **2012**, *57*, 724–803. [CrossRef]
255. Jrondi, A.; Buvat, G.; Pena, F.D.L.; Marinova, M.; Huvé, M.; Brousse, T.; Roussel, P.; Lethien, C. Major Improvement in the Cycling Ability of Pseudocapacitive Vanadium Nitride Films for Micro-Supercapacitor. *Adv. Energy Mater.* **2023**, *13*, 2203462. [CrossRef]
256. Lim, J.H.; Choi, D.J.; Kim, H.-K.; Cho, W., II; Yoon, Y.S. Thin Film Supercapacitors Using a Sputtered RuO_2 Electrode. *J. Electrochem. Soc.* **2001**, *148*, A275. [CrossRef]

257. Patnaik, S.G.; Shamsudeen Seenath, J.; Bourrier, D.; Prabhudev, S.; Guay, D.; Pech, D. Porous RuOxNySzElectrodes for Microsupercapacitors and Microbatteries with Enhanced Areal Performance. *ACS Energy Lett.* **2021**, *6*, 131–139. [CrossRef]
258. Sugimoto, W.; Iwata, H.; Yokoshima, K.; Murakami, Y.; Takasu, Y. Proton and Electron Conductivity in Hydrous Ruthenium Oxides Evaluated by Electrochemical Impedance Spectroscopy: The Origin of Large Capacitance. *J. Phys. Chem. B* **2005**, *109*, 7330–7338. [CrossRef]
259. Yoon, Y.S.; Cho, W.I.; Lim, J.H.; Choi, D.J. Solid-State Thin-Film Supercapacitor with Ruthenium Oxide and Solid Electrolyte Thin Films. *J. Power Sources* **2001**, *101*, 126–129. [CrossRef]
260. Ferris, A.; Garbarino, S.; Guay, D.; Pech, D. 3D RuO_2 Microsupercapacitors with Remarkable Areal Energy. *Adv. Mater.* **2015**, *27*, 6625–6629. [CrossRef] [PubMed]
261. Ponrouch, A.; Garbarino, S.; Bertin, E.; Guay, D. Ultra High Capacitance Values of Pt@RuO_2 Core-Shell Nanotubular Electrodes for Microsupercapacitor Applications. *J. Power Sources* **2013**, *221*, 228–231. [CrossRef]
262. Dinh, T.M.; Armstrong, K.; Guay, D.; Pech, D. High-Resolution on-Chip Supercapacitors with Ultra-High Scan Rate Ability. *J. Mater. Chem. A Mater.* **2014**, *2*, 7170–7174. [CrossRef]
263. Eustache, E.; Douard, C.; Demortière, A.; De Andrade, V.; Brachet, M.; Le Bideau, J.; Brousse, T.; Lethien, C. High Areal Energy 3D-Interdigitated Micro-Supercapacitors in Aqueous and Ionic Liquid Electrolytes. *Adv. Mater. Technol.* **2017**, *2*, 1700126. [CrossRef]
264. Li, F.; Hu, A.; Zhao, X.; Wu, T.; Chen, W.; Lei, T.; Hu, Y.; Huang, M.; Wang, X. On-Chip High-Energy Interdigital Micro-Supercapacitors with 3D Nanotubular Array Electrodes. *J. Mater. Chem. A Mater.* **2022**, *10*, 14051–14059. [CrossRef]
265. Si, W.; Yan, C.; Chen, Y.; Oswald, S.; Han, L.; Schmidt, O.G. On Chip, All Solid-State and Flexible Micro-Supercapacitors with High Performance Based on MnOx/Au Multilayers. *Energy Environ. Sci.* **2013**, *6*, 3218–3223. [CrossRef]
266. Wu, H.; Jiang, K.; Gu, S.; Yang, H.; Lou, Z.; Chen, D.; Shen, G. Two-Dimensional $Ni(OH)_2$ Nanoplates for Flexible on-Chip Microsupercapacitors. *Nano Res.* **2015**, *8*, 3544–3552. [CrossRef]
267. Li, L.; Lou, Z.; Han, W.; Shen, G. Flexible In-Plane Microsupercapacitors with Electrospun NiFe2O4 Nanofibers for Portable Sensing Applications. *Nanoscale* **2016**, *8*, 14986–14991. [CrossRef]
268. Liu, B.; Zhang, Q.; Zhang, L.; Xu, C.; Pan, Z.; Zhou, Q.; Zhou, W.; Wang, J.; Gu, L.; Liu, H.; et al. Electrochemically Exfoliated Chlorine-Doped Graphene for Flexible All-Solid-State Micro-Supercapacitors with High Volumetric Energy Density. *Adv. Mater.* **2022**, *34*, 2106309. [CrossRef]
269. Wu, Z.-S.; Zheng, Y.; Zheng, S.; Wang, S.; Sun, C.; Parvez, K.; Ikeda, T.; Bao, X.; Müllen, K.; Feng, X.; et al. Stacked-Layer Heterostructure Films of 2D Thiophene Nanosheets and Graphene for High-Rate All-Solid-State Pseudocapacitors with Enhanced Volumetric Capacitance. *Adv. Mater.* **2017**, *29*, 1602960. [CrossRef]
270. Liu, L.; Lu, J.Y.; Long, X.L.; Zhou, R.; Liu, Y.Q.; Wu, Y.T.; Yan, K.W. 3D Printing of High-Performance Micro-Supercapacitors with Patterned Exfoliated Graphene/Carbon Nanotube/Silver Nanowire Electrodes. *Sci. China Technol. Sci.* **2021**, *64*, 1065–1073. [CrossRef]
271. Yuan, Y.; Jiang, L.; Li, X.; Zuo, P.; Xu, C.; Tian, M.; Zhang, X.; Wang, S.; Lu, B.; Shao, C.; et al. Laser Photonic-Reduction Stamping for Graphene-Based Micro-Supercapacitors Ultrafast Fabrication. *Nat. Commun.* **2020**, *11*, 6185. [CrossRef]
272. Jung, J.; Jeong, J.R.; Lee, J.; Lee, S.H.; Kim, S.Y.; Kim, M.J.; Nah, J.; Lee, M.H. In Situ Formation of Graphene/Metal Oxide Composites for High-Energy Microsupercapacitors. *NPG Asia Mater.* **2020**, *12*, 50. [CrossRef]
273. Zhang, P.; Zhu, F.; Wang, F.; Wang, J.; Dong, R.; Zhuang, X.; Schmidt, O.G.; Feng, X.; Zhang, P.; Wang, F.; et al. Stimulus-Responsive Micro-Supercapacitors with Ultrahigh Energy Density and Reversible Electrochromic Window. *Adv. Mater.* **2017**, *29*, 1604491. [CrossRef] [PubMed]
274. Li, H.; Tang, P.; Shen, H.; Hu, T.; Chen, J.; Chen, K.; Qi, F.; Yang, H.; Wen, L.; Li, F. Scalable Fabrication of Vanadium Carbide/Graphene Electrodes for High-Energy and Flexible Microsupercapacitors. *Carbon* **2021**, *183*, 840–849. [CrossRef]
275. Tian, H.; Qin, J.; Hou, D.; Li, Q.; Li, C.; Wu, Z.-S.; Mai, Y.; Tian, H.; Hou, D.; Li, Q.; et al. General Interfacial Self-Assembly Engineering for Patterning Two-Dimensional Polymers with Cylindrical Mesopores on Graphene. *Angew. Chem.* **2019**, *131*, 10279–10284. [CrossRef]
276. Lee, H.Y.; Goodenough, J.B. Supercapacitor Behavior with KCl Electrolyte. *J. Solid. State Chem.* **1999**, *144*, 220–223. [CrossRef]
277. Toupin, M.; Brousse, T.; Bélanger, D. Influence of Microstucture on the Charge Storage Properties of Chemically Synthesized Manganese Dioxide. *Chem. Mater.* **2002**, *14*, 3946–3952. [CrossRef]
278. Li, S.H.; Liu, Q.H.; Qi, L.; Lu, L.H.; Wang, H.Y. Progress in Research on Manganese Dioxide Electrode Aterials for Electrochemical Capacitors. *Fenxi Huaxue/Chin. J. Anal. Chem.* **2012**, *40*, 339–346. [CrossRef]
279. Nam, K.W.; Lee, C.W.; Yang, X.Q.; Cho, B.W.; Yoon, W.S.; Kim, K.B. Electrodeposited Manganese Oxides on Three-Dimensional Carbon Nanotube Substrate: Supercapacitive Behaviour in Aqueous and Organic Electrolytes. *J. Power Sources* **2009**, *188*, 323–331. [CrossRef]
280. Yugang, S.; Yuzi, L.; Tu, T.T.; Yang, R. Thermal Transformation of 7sigma;-MnO2 Nanoflowers Studied by in-Situ TEM. *Sci. China Chem.* **2012**, *55*, 2346–2352. [CrossRef]
281. Fischer, A.E.; Pettigrew, K.A.; Rolison, D.R.; Stroud, R.M.; Long, J.W. Incorporation of Homogeneous, Nanoscale MnO2 within Ultraporous Carbon Structures via Self-Limiting Electroless Deposition: Implications for Electrochemical Capacitors. *Nano Lett.* **2007**, *7*, 281–286. [CrossRef] [PubMed]

282. Qin, J.; Wang, S.; Zhou, F.; Das, P.; Zheng, S.; Sun, C.; Bao, X.; Wu, Z.S. 2D Mesoporous MnO_2 Nanosheets for High-Energy Asymmetric Micro-Supercapacitors in Water-in-Salt Gel Electrolyte. *Energy Storage Mater.* **2019**, *18*, 397–404. [CrossRef]
283. Aricò, A.S.; Bruce, P.; Scrosati, B.; Tarascon, J.M.; Van Schalkwijk, W. Nanostructured Materials for Advanced Energy Conversion and Storage Devices. *Nat. Mater.* **2005**, *4*, 366–377. [CrossRef]
284. Liu, W.; Lu, C.; Wang, X.; Tay, R.Y.; Tay, B.K. High-Performance Microsupercapacitors Based on Two-Dimensional Graphene/Manganese Dioxide/Silver Nanowire Ternary Hybrid Film. *ACS Nano* **2015**, *9*, 1528–1542. [CrossRef]
285. Toupin, M.; Brousse, T.; Bélanger, D. Charge Storage Mechanism of MnO_2 Electrode Used in Aqueous Electrochemical Capacitor. *Chem. Mater.* **2004**, *16*, 3184–3190. [CrossRef]
286. Pang, S.-C.; Anderson, M.A.; Chapman, T.W. Novel Electrode Materials for Thin-Film Ultracapacitors: Comparison of Electrochemical Properties of Sol-Gel-Derived and Electrodeposited Manganese Dioxide. *J. Electrochem. Soc.* **2000**, *147*, 444. [CrossRef]
287. Hung, C.J.; Hung, J.H.; Lin, P.; Tseng, T.Y. Electrophoretic Fabrication and Characterizations of Manganese Oxide/Carbon Nanotube Nanocomposite Pseudocapacitors. *J. Electrochem. Soc.* **2011**, *158*, A942. [CrossRef]
288. Wang, Y.; Zhitomirsky, I. Electrophoretic Deposition of Manganese Dioxide—Multiwalled Carbon Nanotube Composites for Electrochemical Supercapacitors. *Langmuir* **2009**, *25*, 9684–9689. [CrossRef]
289. Broughton, J.N.; Brett, M.J. Investigation of Thin Sputtered Mn Films for Electrochemical Capacitors. *Electrochim. Acta* **2004**, *49*, 4439–4446. [CrossRef]
290. Agrawal, R.; Wang, C. On-Chip Asymmetric Microsupercapacitors Combining Reduced Graphene Oxide and Manganese Oxide for High Energy-Power Tradeoff. *Micromachines* **2018**, *9*, 399. [CrossRef]
291. Byun, S.; Shim, Y.; Min Yuk, J.; Lee, C.W.; Yoo, J. Reduced Graphene Oxide as a Charge Reservoir of Manganese Oxide: Interfacial Interaction Promotes Charge Storage Property of MnOx-Based Micro-Supercapacitors. *Chem. Eng. J.* **2022**, *439*, 135569. [CrossRef]
292. Dubal, D.P.; Dhawale, D.S.; Salunkhe, R.R.; Pawar, S.M.; Lokhande, C.D. A Novel Chemical Synthesis and Characterization of Mn3O4 Thin Films for Supercapacitor Application. *Appl. Surf. Sci.* **2010**, *256*, 4411–4416. [CrossRef]
293. Yadav, A.A.; Jadhav, S.N.; Chougule, D.M.; Patil, P.D.; Chavan, U.J.; Kolekar, Y.D. Spray Deposited Hausmannite Mn3O4 Thin Films Using Aqueous/Organic Solvent Mixture for Supercapacitor Applications. *Electrochim. Acta* **2016**, *206*, 134–142. [CrossRef]
294. Wu, Y.; Liu, S.; Wang, H.; Wang, X.; Zhang, X.; Jin, G. A Novel Solvothermal Synthesis of Mn3O4/Graphene Composites for Supercapacitors. *Electrochim. Acta* **2013**, *90*, 210–218. [CrossRef]
295. Shi, X.; Zeng, Z.; Liao, C.; Tao, S.; Guo, E.; Long, X.; Wang, X.; Deng, D.; Dai, Y. Flexible, Planar Integratable and All-Solid-State Micro-Supercapacitors Based on Nanoporous Gold/ Manganese Oxide Hybrid Electrodes via Template Plasma Etching Method. *J. Alloys Compd.* **2018**, *739*, 979–986. [CrossRef]
296. Li, X.J.; Song, Z.-W.; Zhao, Y.; Wang, Y.; Zhao, X.C.; Liang, M.; Chu, W.G.; Jiang, P.; Liu, Y. Vertically Porous Nickel Thin Film Supported Mn3O4 for Enhanced Energy Storage Performance. *J. Colloid. Interface Sci.* **2016**, *483*, 17–25. [CrossRef] [PubMed]
297. Gao, M.; Dong, X.; Mei, X.; Wang, K.; Wang, W.; Zhu, C.; Duan, W.; Sun, X. Laser Direct Writing of Graphene/MnO-Mn3O4 Doped with Sulfur for High-Performance Microsupercapacitors. *J. Energy Storage* **2022**, *49*, 104118. [CrossRef]
298. Li, Y.Q.; Shi, X.M.; Lang, X.Y.; Wen, Z.; Li, J.C.; Jiang, Q. Remarkable Improvements in Volumetric Energy and Power of 3D MnO_2 Microsupercapacitors by Tuning Crystallographic Structures. *Adv. Funct. Mater.* **2016**, *26*, 1830–1839. [CrossRef]
299. Bounor, B.; Seenath, J.S.; Patnaik, S.G.; Bourrier, D.; Tran, C.C.H.; Esvan, J.; Weingarten, L.; Descamps-Mandine, A.; Rochefort, D.; Guay, D.; et al. Low-Cost Micro-Supercapacitors Using Porous Ni/MnO_2 Entangled Pillars and Na-Based Ionic Liquids. *Energy Storage Mater.* **2023**, *63*, 102986. [CrossRef]
300. Liu, C.; Li, Z.; Zhang, Z. Molybdenum Oxide Film with Stable Pseudocapacitive Property for Aqueous Micro-Scale Electrochemical Capacitor. *Electrochim. Acta* **2014**, *134*, 84–91. [CrossRef]
301. Zhu, Y.; Ji, X.; Cheng, S.; Chern, Z.Y.; Jia, J.; Yang, L.; Luo, H.; Yu, J.; Peng, X.; Wang, J.; et al. Fast Energy Storage in Two-Dimensional MoO_2 Enabled by Uniform Oriented Tunnels. *ACS Nano* **2019**, *13*, 9091–9099. [CrossRef] [PubMed]
302. Wang, S.; Yong, H.; Yao, J.; Ma, J.; Liu, B.; Hu, J.; Zhang, Y. Influence of the Phase Evolution and Hydrogen Storage Behaviors of Mg-RE Alloy by a Multi-Valence Mo-Based Catalyst. *J. Energy Storage* **2023**, *58*, 106397. [CrossRef]
303. Vincent, R.C.; Luo, Y.; Andrews, J.L.; Zohar, A.; Zhou, Y.; Yan, Q.; Mozur, E.M.; Preefer, M.B.; Weker, J.N.; Cheetham, A.K.; et al. High-Rate Lithium Cycling and Structure Evolution in Mo_4O_{11}. *Chem. Mater.* **2022**, *34*, 4122–4133. [CrossRef]
304. Ge, H.; Kuwahara, Y.; Yamashita, H. Development of Defective Molybdenum Oxides for Photocatalysis, Thermal Catalysis, and Photothermal Catalysis. *Chem. Commun.* **2022**, *58*, 8466–8479. [CrossRef] [PubMed]
305. Wang, Y.; Wang, H.; Qu, G. Molybdenum-Based Electrode Materials Applied in High-Performance Supercapacitors. *Batteries* **2023**, *9*, 479. [CrossRef]
306. Maheswari, N.; Muralidharan, G. Controlled Synthesis of Nanostructured Molybdenum Oxide Electrodes for High Performance Supercapacitor Devices. *Appl. Surf. Sci.* **2017**, *416*, 461–469. [CrossRef]
307. Tang, W.; Liu, L.; Tian, S.; Li, L.; Yue, Y.; Wu, Y.; Zhu, K. Aqueous Supercapacitors of High Energy Density Based on MoO_3 Nanoplates as Anode Material. *Chem. Commun.* **2011**, *47*, 10058–10060. [CrossRef] [PubMed]
308. Liang, R.; Cao, H.; Qian, D. MoO3 Nanowires as Electrochemical Pseudocapacitor Materials. *Chem. Commun.* **2011**, *47*, 10305–10307. [CrossRef]
309. Zhao, X.Y.; Gong, L.G.; Wang, C.X.; Wang, C.M.; Yu, K.; Zhou, B.B. Silver-Doped Molybdenum Oxide Ternary Nanoparticles with Excellent Supercapacitor and Hydrogen Peroxide-Sensing Performance. *Mater. Today Energy* **2021**, *20*, 100774. [CrossRef]

310. Xu, Y.; Deng, P.; Chen, R.; Xie, W.; Xu, Z.; Yang, Y.; Liu, D.; Huang, F.; Zhuang, Z.; Zhitomirsky, I.; et al. Electric Discharge Direct Writing of 3D Mo-MoOx Pseudocapacitive Micro-Supercapacitors with Designable Patterns. *Ceram. Int.* **2023**, *49*, 22586–22594. [CrossRef]
311. Liu, C.; Li, Z.; Zhang, Z. Growth of [010] Oriented α-MoO_3 Nanorods by Pulsed Electron Beam Deposition. *Appl. Phys. Lett.* **2011**, *99*, 223104. [CrossRef]
312. Prakash, N.G.; Dhananjaya, M.; Narayana, A.L.; Shaik, D.P.; Rosaiah, P.; Hussain, O.M. High Performance One Dimensional α-MoO_3 Nanorods for Supercapacitor Applications. *Ceram. Int.* **2018**, *44*, 9967–9975. [CrossRef]
313. Shaheen, I.; Ahmad, K.S.; Zequine, C.; Gupta, R.K.; Thomas, A.G.; Malik, M.A. Electrochemical Energy Storage by Nanosized MoO_3/PdO Material: Investigation of Its Structural, Optical and Electrochemical Properties for Supercapacitor. *J. Energy Storage* **2021**, *36*, 102447. [CrossRef]
314. Brezesinski, T.; Wang, J.; Tolbert, S.H.; Dunn, B. Ordered Mesoporous α-MoO_3 with Iso-Oriented Nanocrystalline Walls for Thin-Film Pseudocapacitors. *Nat. Mater.* **2010**, *9*, 146–151. [CrossRef]
315. Kim, H.S.; Cook, J.B.; Lin, H.; Ko, J.S.; Tolbert, S.H.; Ozolins, V.; Dunn, B. Oxygen Vacancies Enhance Pseudocapacitive Charge Storage Properties of MoO_3-x. *Nat. Mater.* **2017**, *16*, 454–460. [CrossRef]
316. Gurusamy, L.; Karuppasamy, L.; Anandan, S.; Liu, N.; Lee, G.J.; Liu, C.H.; Wu, J.J. Enhanced Performance of Charge Storage Supercapattery by Dominant Oxygen Deficiency in Crystal Defects of 2-D MoO_3-x Nanoplates. *Appl. Surf. Sci.* **2021**, *541*, 148676. [CrossRef]
317. Xiao, X.; Ding, T.; Yuan, L.; Shen, Y.; Zhong, Q.; Zhang, X.; Cao, Y.; Hu, B.; Zhai, T.; Gong, L.; et al. WO_3-x/MoO_3-x Core/Shell Nanowires on Carbon Fabric as an Anode for All-Solid-State Asymmetric Supercapacitors. *Adv. Energy Mater.* **2012**, *2*, 1328–1332. [CrossRef]
318. Huang, L.; Yao, B.; Sun, J.; Gao, X.; Wu, J.; Wan, J.; Li, T.; Hu, Z.; Zhou, J. Highly Conductive and Flexible Molybdenum Oxide Nanopaper for High Volumetric Supercapacitor Electrode. *J. Mater. Chem. A Mater.* **2017**, *5*, 2897–2903. [CrossRef]
319. Guru Prakash, N.; Dhananjaya, M.; Lakshmi Narayana, A.; Hussain, O.M. One-Dimensional MoO_3/Pd Nanocomposite Electrodes for High Performance Supercapacitors. *Mater. Res. Express* **2019**, *6*, 085543. [CrossRef]
320. Cheng, A.; Shen, Y.; Hong, T.; Zhan, R.; Chen, E.; Chen, Z.; Chen, G.; Liang, M.; Sun, X.; Wang, D.; et al. Self-Assembly Vertical Graphene-Based MoO_3 Nanosheets for High Performance Supercapacitors. *Nanomaterials* **2022**, *12*, 2057. [CrossRef]
321. Zhang, X.; Zhao, W.; Wei, L.; Jin, Y.; Hou, J.; Wang, X.; Guo, X. In-Plane Flexible Solid-State Microsupercapacitors for on-Chip Electronics. *Energy* **2019**, *170*, 338–348. [CrossRef]
322. Chen, J.; Han, S.; Zhao, H.; Bai, J.; Wang, L.; Sun, G.; Zhang, Z.; Pan, X.; Zhou, J.; Xie, E. Robust Wire-Based Supercapacitors Based on Hierarchical A-MoO_3 Nanosheet Arrays with Well-Aligned Laminated Structure. *Chem. Eng. J.* **2017**, *320*, 34–42. [CrossRef]
323. Singh, B.K.; Shaikh, A.; Badrayyana, S.; Mohapatra, D.; Dusane, R.O.; Parida, S. Nanoporous Gold-Copper Oxide Based All-Solid-State Micro-Supercapacitors. *RSC Adv.* **2016**, *6*, 100467–100475. [CrossRef]
324. Zhang, L.; Chen, Z.; Zheng, S.; Qin, S.; Wang, J.; Chen, C.; Liu, D.; Wang, L.; Yang, G.; Su, Y.; et al. Shape-Tailorable High-Energy Asymmetric Micro-Supercapacitors Based on Plasma Reduced and Nitrogen-Doped Graphene Oxide and MoO_2 Nanoparticles. *J. Mater. Chem. A Mater.* **2019**, *7*, 14328–14336. [CrossRef]
325. Lin, N.; Chen, H.; Wang, W.; Lu, L. Laser-Induced Graphene/MoO_2 Core-Shell Electrodes on Carbon Cloth for Integrated, High-Voltage, and In-Planar Microsupercapacitors. *Adv. Mater. Technol.* **2021**, *6*, 2000991. [CrossRef]
326. Zhang, L.; Yang, G.; Chen, Z.; Liu, D.; Wang, J.; Qian, Y.; Chen, C.; Liu, Y.; Wang, L.; Razal, J.; et al. MXene Coupled with Molybdenum Dioxide Nanoparticles as 2D-0D Pseudocapacitive Electrode for High Performance Flexible Asymmetric Micro-Supercapacitors. *J. Mater.* **2020**, *6*, 138–144. [CrossRef]
327. Liu, D.-Q.; Yu, S.-H.; Son, S.-W.; Joo, S.-K. Electrochemical Performance of Iridium Oxide Thin Film for Supercapacitor Prepared by Radio Frequency Magnetron Sputtering Method. *ECS Trans.* **2008**, *16*, 103. [CrossRef]
328. Liao, P.C.; Ho, W.S.; Huang, Y.S.; Tiong, K.K. Characterization of Sputtered Iridium Dioxide Thin Films. *J. Mater. Res.* **1998**, *13*, 1318–1326. [CrossRef]
329. Beknalkar, S.A.; Teli, A.M.; Harale, N.S.; Shin, J.C.; Patil, P.S. Construction of IrO_2@Mn_3O_4 Core-Shell Heterostructured Nanocomposites for High Performance Symmetric Supercapacitor Device. *J. Alloys Compd.* **2021**, *887*, 161328. [CrossRef]
330. Sethuraman, B.; Purushothaman, K.K.; Muralidharan, G. Synthesis of Mesh-like Fe_2O_3/C Nanocomposite via Greener Route for High Performance Supercapacitors. *RSC Adv.* **2014**, *4*, 4631–4637. [CrossRef]
331. Tang, Q.; Wang, W.; Wang, G. The Perfect Matching between the Low-Cost Fe_2O_3 Nanowire Anode and the NiO Nanoflake Cathode Significantly Enhances the Energy Density of Asymmetric Supercapacitors. *J. Mater. Chem. A Mater.* **2015**, *3*, 6662–6670. [CrossRef]
332. Kulal, P.M.; Dubal, D.P.; Lokhande, C.D.; Fulari, V.J. Chemical Synthesis of Fe_2O_3 Thin Films for Supercapacitor Application. *J. Alloys Compd.* **2011**, *509*, 2567–2571. [CrossRef]
333. Xie, K.; Li, J.; Lai, Y.; Lu, W.; Zhang, Z.; Liu, Y.; Zhou, L.; Huang, H. Highly Ordered Iron Oxide Nanotube Arrays as Electrodes for Electrochemical Energy Storage. *Electrochem. Commun.* **2011**, *13*, 657–660. [CrossRef]
334. Gund, G.S.; Dubal, D.P.; Chodankar, N.R.; Cho, J.Y.; Gomez-Romero, P.; Park, C.; Lokhande, C.D. Low-Cost Flexible Supercapacitors with High-Energy Density Based on Nanostructured MnO_2 and Fe_2O_3 Thin Films Directly Fabricated onto Stainless Steel. *Sci. Rep.* **2015**, *5*, 12454. [CrossRef] [PubMed]

335. Shivakumara, S.; Penki, T.R.; Munichandraiah, N. High Specific Surface Area α-Fe_2O_3 Nanostructures as High Performance Electrode Material for Supercapacitors. *Mater. Lett.* **2014**, *131*, 100–103. [CrossRef]
336. Wang, D.; Wang, Q.; Wang, T. Controlled Synthesis of Mesoporous Hematite Nanostructures and Their Application as Electrochemical Capacitor Electrodes. *Nanotechnology* **2011**, *22*, 135604. [CrossRef]
337. Zeng, Y.; Yu, M.; Meng, Y.; Fang, P.; Lu, X.; Tong, Y. Iron-Based Supercapacitor Electrodes: Advances and Challenges. *Adv. Energy Mater.* **2016**, *6*, 1601053. [CrossRef]
338. Xia, Q.; Xu, M.; Xia, H.; Xie, J. Nanostructured Iron Oxide/Hydroxide-Based Electrode Materials for Supercapacitors. *ChemNanoMat* **2016**, *2*, 588–600. [CrossRef]
339. Ma, J.; Guo, X.; Yan, Y.; Xue, H.; Pang, H. FeO_x-Based Materials for Electrochemical Energy Storage. *Adv. Sci.* **2018**, *5*, 1700986. [CrossRef]
340. Yu, S.; Hong Ng, V.M.; Wang, F.; Xiao, Z.; Li, C.; Kong, L.B.; Que, W.; Zhou, K. Synthesis and Application of Iron-Based Nanomaterials as Anodes of Lithium-Ion Batteries and Supercapacitors. *J. Mater. Chem. A Mater.* **2018**, *6*, 9332–9367. [CrossRef]
341. El Issmaeli, Y.; Lahrichi, A.; Kalanur, S.S.; Natarajan, S.K.; Pollet, B.G. Recent Advances and Prospects of FeOOH-Based Electrode Materials for Supercapacitors. *Batteries* **2023**, *9*, 259. [CrossRef]
342. Sakurai, S.; Namai, A.; Hashimoto, K.; Ohkoshi, S.I. First Observation of Phase Transformation of All Four Fe_2O_3 Phases (γ → ε → β → α-Phase). *J. Am. Chem. Soc.* **2009**, *131*, 18299–18303. [CrossRef]
343. Danno, T.; Nakatsuka, D.; Kusano, Y.; Asaoka, H.; Nakanishi, M.; Fujii, T.; Ikeda, Y.; Takada, J. Crystal Structure of β-Fe_2O_3 and Topotactic Phase Transformation to α-Fe_2O_3. *Cryst. Growth Des.* **2013**, *13*, 770–774. [CrossRef]
344. An, C.; Zhang, Y.; Guo, H.; Wang, Y. Metal Oxide-Based Supercapacitors: Progress and Prospectives. *Nanoscale Adv.* **2019**, *1*, 4644–4658. [CrossRef]
345. Wang, T.; Chen, H.C.; Yu, F.; Zhao, X.S.; Wang, H. Boosting the Cycling Stability of Transition Metal Compounds-Based Supercapacitors. *Energy Storage Mater.* **2019**, *16*, 545–573. [CrossRef]
346. Zhang, H.; Cao, Y.; Chee, M.O.L.; Dong, P.; Ye, M.; Shen, J. Recent Advances in Micro-Supercapacitors. *Nanoscale* **2019**, *11*, 5807–5821. [CrossRef]
347. Sheng, S.; Liu, W.; Zhu, K.; Cheng, K.; Ye, K.; Wang, G.; Cao, D.; Yan, J. Fe_3O_4 Nanospheres in Situ Decorated Graphene as High-Performance Anode for Asymmetric Supercapacitor with Impressive Energy Density. *J. Colloid. Interface Sci.* **2019**, *536*, 235–244. [CrossRef]
348. Zhu, M.; Meng, W.; Huang, Y.; Huang, Y.; Zhi, C. Proton-Insertion-Enhanced Pseudocapacitance Based on the Assembly Structure of Tungsten Oxide. *ACS Appl. Mater. Interfaces* **2014**, *6*, 18901–18910. [CrossRef]
349. Zheng, F.; Gong, H.; Li, Z.; Yang, W.; Xu, J.; Hu, P.; Li, Y.; Gong, Y.; Zhen, Q. Tertiary Structure of Cactus-like WO_3 Spheres Self-Assembled on Cu Foil for Supercapacitive Electrode Materials. *J. Alloys Compd.* **2017**, *712*, 345–354. [CrossRef]
350. Yoon, S.; Kang, E.; Kon Kim, J.; Wee Lee, C.; Lee, J. Development of High-Performance Supercapacitor Electrodes Using Novel Ordered Mesoporous Tungsten Oxide Materials with High Electrical Conductivity. *Chem. Commun.* **2011**, *47*, 1021–1023. [CrossRef]
351. Yang, P.; Sun, P.; Du, L.; Liang, Z.; Xie, W.; Cai, X.; Huang, L.; Tan, S.; Mai, W. Quantitative Analysis of Charge Storage Process of Tungsten Oxide That Combines Pseudocapacitive and Electrochromic Properties. *J. Phys. Chem. C* **2015**, *119*, 16483–16489. [CrossRef]
352. Liu, X.; Sheng, G.; Zhong, M.; Zhou, X. Dispersed and Size-Selected WO_3 Nanoparticles in Carbon Aerogel for Supercapacitor Applications. *Mater. Des.* **2018**, *141*, 220–229. [CrossRef]
353. Jia, J.; Liu, X.; Mi, R.; Liu, N.; Xiong, Z.; Yuan, L.; Wang, C.; Sheng, G.; Cao, L.; Zhou, X.; et al. Self-Assembled Pancake-like Hexagonal Tungsten Oxide with Ordered Mesopores for Supercapacitors. *J. Mater. Chem. A Mater.* **2018**, *6*, 15330–15339. [CrossRef]
354. Huang, X.; Liu, H.; Zhang, X.; Jiang, H. High Performance All-Solid-State Flexible Micro-Pseudocapacitor Based on Hierarchically Nanostructured Tungsten Trioxide Composite. *ACS Appl. Mater. Interfaces* **2015**, *7*, 27845–27852. [CrossRef]
355. Shinde, P.A.; Jun, S.C. Review on Recent Progress in the Development of Tungsten Oxide Based Electrodes for Electrochemical Energy Storage. *ChemSusChem* **2020**, *13*, 11–38. [CrossRef]
356. Cong, S.; Geng, F.; Zhao, Z. Tungsten Oxide Materials for Optoelectronic Applications. *Adv. Mater.* **2016**, *28*, 10518–10528. [CrossRef] [PubMed]
357. Augustyn, V.; Simon, P.; Dunn, B. Pseudocapacitive Oxide Materials for High-Rate Electrochemical Energy Storage. *Energy Environ. Sci.* **2014**, *7*, 1597–1614. [CrossRef]
358. Lin, J.; Du, X. High Performance Asymmetric Supercapacitor Based on Hierarchical Carbon Cloth in Situ Deposited with H-Wo_3 Nanobelts as Negative Electrode and Carbon Nanotubes as Positive Electrode. *Micromachines* **2021**, *12*, 1195. [CrossRef]
359. Shi, F.; Li, J.; Xiao, J.; Zhao, X.; Li, H.; An, Q.; Zhai, S.; Wang, K.; Wei, L.; Tong, Y. Three-Dimensional Hierarchical Porous Lignin-Derived Carbon/WO_3 for High-Performance Solid-State Planar Micro-Supercapacitor. *Int. J. Biol. Macromol.* **2021**, *190*, 11–18. [CrossRef]
360. Hepel, M.; Petrukhina, M.A.; Samuilov, V. High Power-Density WO_3-x–Grafted Corannulene-Modified Graphene Nanostructures for Micro-Supercapacitors. *J. Electroanal. Chem.* **2023**, *928*, 116990. [CrossRef]
361. Lillard, R.S.; Kanner, G.S.; Butt, D.P. The Nature of Oxide Films on Tungsten in Acidic and Alkaline Solutions. *J. Electrochem. Soc.* **1998**, *145*, 2718. [CrossRef]

362. Anik, M.; Osseo-Asare, K. Effect of PH on the Anodic Behavior of Tungsten. *J. Electrochem. Soc.* **2002**, *149*, B224. [CrossRef]
363. Di Paola, A.; Di Quarto, F.; Sunseri, C. Electrochromism in Anodically Formed Tungsten Oxide Films. *J. Electrochem. Soc.* **1978**, *125*, 1344. [CrossRef]
364. El-Basiouny, M.S.; Hassan, S.A.; Hefny, M.M. On the Electrochemical Behaviour of Tungsten: The Formation and Dissolution of Tungsten Oxide in Sulphuric Acid Solutions. *Corros. Sci.* **1980**, *20*, 909–917. [CrossRef]
365. Qu, Q.T.; Liu, L.L.; Wu, Y.P.; Holze, R. Electrochemical Behavior of $V_2O_5{\cdot}0.6H_2O$ Nanoribbons in Neutral Aqueous Electrolyte Solution. *Electrochim. Acta* **2013**, *96*, 8–12. [CrossRef]
366. Yan, Y.; Li, B.; Guo, W.; Pang, H.; Xue, H. Vanadium Based Materials as Electrode Materials for High Performance Supercapacitors. *J. Power Sources* **2016**, *329*, 148–169. [CrossRef]
367. Lai, W.-Y.; Wei Huang, P.; Kang, J.; Zhang, Q.; Wang, Y.; Wen-Yong Lai, S.; Zhang, Y.-Z.; Wang, Y.; Cheng, T.; Yao, L.-Q.; et al. Printed Supercapacitors: Materials, Printing and Applications. *Chem. Soc. Rev.* **2019**, *48*, 3229–3264. [CrossRef]
368. Huang, Z.H.; Song, Y.; Liu, X.X. Boosting Operating Voltage of Vanadium Oxide-Based Symmetric Aqueous Supercapacitor to 2 V. *Chem. Eng. J.* **2019**, *358*, 1529–1538. [CrossRef]
369. Arico, C.; Ouendi, S.; Taberna, P.L.; Roussel, P.; Simon, P.; Lethien, C. Fast Electrochemical Storage Process in Sputtered Nb_2O_5 Porous Thin Films. *ACS Nano* **2019**, *13*, 5826–5832. [CrossRef]
370. Ahmad, M.W.; Dey, B.; Syed, A.; Bahkali, A.H.; Verma, M.; Yang, D.J.; Choudhury, A. MOFs-Derived Niobium Oxide Nanoparticles/Carbon Nanofiber Hybrid Paper as Flexible Binder-Free Electrode for Solid-State Asymmetric Supercapacitors. *J. Alloys Compd.* **2023**, *957*, 170269. [CrossRef]
371. Brousse, K.; Taberna, P.L.; Simon, P. Current Collector-Free Interdigitated Nb_2O_5//$LiFePO_4$ Micro-Batteries Prepared by a Simple Laser-Writing Process. *J. Electrochem. Soc.* **2022**, *169*, 070534. [CrossRef]
372. Yuan, Y.; Li, X.; Jiang, L.; Liang, M.; Zhang, X.; Wu, S.; Wu, J.; Tian, M.; Zhao, Y.; Qu, L. Laser Maskless Fast Patterning for Multitype Microsupercapacitors. *Nat. Commun.* **2023**, *14*, 3967. [CrossRef] [PubMed]
373. Zhang, H.; Wang, B.; Brown, B. Atomic Layer Deposition of Titanium Oxide and Nitride on Vertically Aligned Carbon Nanotubes for Energy Dense 3D Microsupercapacitors. *Appl. Surf. Sci.* **2020**, *521*, 146349. [CrossRef]
374. Siddiqui, S.A.; Das, S.; Rani, S.; Afshan, M.; Pahuja, M.; Jain, A.; Rani, D.; Chaudhary, N.; Jyoti; Ghosh, R.; et al. Phosphorus-Doped Nickel Oxide Micro-Supercapacitor: Unleashing the Power of Energy Storage for Miniaturized Electronic Devices. *Small* **2023**, *20*, 2306756. [CrossRef]
375. Zhang, K.; Ying, G.; Liu, L.; Ma, F.; Su, L.; Zhang, C.; Wu, D.; Wang, X.; Zhou, Y. Three-Dimensional Porous Ti_3C_2 Tx-NiO Composite Electrodes with Enhanced Electrochemical Performance for Supercapacitors. *Materials* **2019**, *12*, 188. [CrossRef]
376. Rao, Y.; Yuan, M.; Luo, F.; Li, H.; Yu, J.; Chen, X. Laser In-Situ Synthesis of Metallic Cobalt Decorated Porous Graphene for Flexible In-Plane Microsupercapacitors. *J. Colloid. Interface Sci.* **2022**, *610*, 775–784. [CrossRef]
377. Zhu, Y.G.; Wang, Y.; Shi, Y.; Wong, J.I.; Yang, H.Y. CoO Nanoflowers Woven by CNT Network for High Energy Density Flexible Micro-Supercapacitor. *Nano Energy* **2014**, *3*, 46–54. [CrossRef]
378. Li, M.; Jia, C.; Zhang, D.; Luo, Y.; Ma, Y.; Luo, G.; Zhao, L.; Wang, L.; Li, Z.; Lin, Q.; et al. An Efficient Cobalt-Nickel Phosphate Positive Electrode for High-Performance Hybrid Microsupercapacitors. *J. Energy Storage* **2023**, *64*, 107144. [CrossRef]
379. Mahendra, G.; Malathi, R.; Kedhareswara, S.P.; Lakshmi-Narayana, A.; Dhananjaya, M.; Guruprakash, N.; Hussain, O.M.; Mauger, A.; Julien, C.M. RF Sputter-Deposited Nanostructured CuO Films for Micro-Supercapacitors. *Appl. Nano* **2021**, *2*, 46–66. [CrossRef]
380. Sayed, D.M.; Salem, K.E.; Allam, N.K. Optimized Lithography-Free Fabrication of Sub-100 Nm Nb_2O_5 Nanotube Films as Negative Supercapacitor Electrodes: Tuned Oxygen Vacancies and Cationic Intercalation. *ACS Appl. Mater. Interfaces* **2022**, *14*, 25545–25555. [CrossRef] [PubMed]
381. Zhai, X.; Liu, J.; Zhao, Y.; Chen, C.; Zhao, X.; Li, J.; Jin, H. Oxygen Vacancy Boosted the Electrochemistry Performance of Ti^{4+} Doped Nb_2O_5 toward Lithium Ion Battery. *Appl. Surf. Sci.* **2020**, *499*, 143905. [CrossRef]
382. Taffa, D.H.; Dillert, R.; Ulpe, A.C.; Bauerfeind, K.C.L.; Bredow, T.; Bahnemann, D.W.; Wark, M. Photoelectrochemical and Theoretical Investigations of Spinel Type Ferrites ($M_xFe_{3-x}O_4$) for Water Splitting: A Mini-Review. *J. Photonics Energy* **2016**, *7*, 012009. [CrossRef]
383. Szotek, Z.; Temmerman, W.M.; Ködderitzsch, D.; Svane, A.; Petit, L.; Winter, H. Electronic Structures of Normal and Inverse Spinel Ferrites from First Principles. *Phys. Rev. B Condens. Matter Mater. Phys.* **2006**, *74*, 174431. [CrossRef]
384. Lin, Y.P.; Wu, N.L. Characterization of $MnFe_2O_4$/$LiMn_2O_4$ Aqueous Asymmetric Supercapacitor. *J. Power Sources* **2011**, *196*, 851–854. [CrossRef]
385. Zhu, B.; Tang, S.; Vongehr, S.; Xie, H.; Zhu, J.; Meng, X. $FeCo_2O_4$ Submicron-Tube Arrays Grown on Ni Foam as High Rate-Capability and Cycling-Stability Electrodes Allowing Superior Energy and Power Densities with Symmetric Supercapacitors. *Chem. Commun.* **2016**, *52*, 2624–2627. [CrossRef]
386. Lannelongue, P.; Le Vot, S.; Fontaine, O.; Brousse, T.; Favier, F. Electrochemical Study of Asymmetric Aqueous Supercapacitors Based on High Density Oxides: C/$Ba_{0.5}Sr_{0.5}Co_{0.8}Fe_{0.2}O_3$-δ and FeWO4/$Ba_{0.5}Sr_{0.5}Co_{0.8}Fe_{0.2}O_3$-δ. *Electrochim. Acta* **2019**, *326*, 134886. [CrossRef]
387. Goubard-Bretesché, N.; Crosnier, O.; Payen, C.; Favier, F.; Brousse, T. Nanocrystalline $FeWO_4$ as a Pseudocapacitive Electrode Material for High Volumetric Energy Density Supercapacitors Operated in an Aqueous Electrolyte. *Electrochem. Commun.* **2015**, *57*, 61–64. [CrossRef]

388. Goubard-Bretesché, N.; Crosnier, O.; Douard, C.; Iadecola, A.; Retoux, R.; Payen, C.; Doublet, M.L.; Kisu, K.; Iwama, E.; Naoi, K.; et al. Unveiling Pseudocapacitive Charge Storage Behavior in $FeWO_4$ Electrode Material by Operando X-Ray Absorption Spectroscopy. *Small* **2020**, *16*, 2002855. [CrossRef]
389. Xing, X.; Gui, Y.; Zhang, G.; Song, C. $CoWO_4$ Nanoparticles Prepared by Two Methods Displaying Different Structures and Supercapacitive Performances. *Electrochim. Acta* **2015**, *157*, 15–22. [CrossRef]
390. Xu, X.; Gao, J.; Huang, G.; Qiu, H.; Wang, Z.; Wu, J.; Pan, Z.; Xing, F. Fabrication of $CoWO_4$@$NiWO_4$ Nanocomposites with Good Supercapacitve Performances. *Electrochim. Acta* **2015**, *174*, 837–845. [CrossRef]
391. Yang, Y.; Zhu, J.; Shi, W.; Zhou, J.; Gong, D.; Gu, S.; Wang, L.; Xu, Z.; Lu, B. 3D Nanoporous $ZnWO_4$ Nanoparticles with Excellent Electrochemical Performances for Supercapacitors. *Mater. Lett.* **2016**, *177*, 34–38. [CrossRef]
392. Jadhav, S.; Donolikar, P.D.; Chodankar, N.R.; Dongale, T.D.; Dubal, D.P.; Patil, D.R. Nano-Dimensional Iron Tungstate for Super High Energy Density Symmetric Supercapacitor with Redox Electrolyte. *J. Solid. State Electrochem.* **2019**, *23*, 3459–3465. [CrossRef]
393. Kuo, S.-L.; Lee, J.-F.; Wu, N.-L. Study on Pseudocapacitance Mechanism of Aqueous $MnFe_2O_4$ Supercapacitor. *J. Electrochem. Soc.* **2007**, *154*, A34. [CrossRef]
394. Kuo, S.L.; Wu, N.L. Electrochemical Capacitor of $MnFe_2O_4$ with NaCl Electrolyte. *Electrochem. Solid-State Lett.* **2005**, *8*, A495. [CrossRef]
395. Ouendi, S.; Robert, K.; Stievenard, D.; Brousse, T.; Roussel, P.; Lethien, C. Sputtered Tungsten Nitride Films as Pseudocapacitive Electrode for on Chip Micro-Supercapacitors. *Energy Storage Mater.* **2019**, *20*, 243–252. [CrossRef]
396. Arif, M.; Sanger, A.; Singh, A. Sputter Deposited Chromium Nitride Thin Electrodes for Supercapacitor Applications. *Mater. Lett.* **2018**, *220*, 213–217. [CrossRef]
397. Bouhtiyya, S.; Lucio Porto, R.; Laïk, B.; Boulet, P.; Capon, F.; Pereira-Ramos, J.P.; Brousse, T.; Pierson, J.F. Application of Sputtered Ruthenium Nitride Thin Films as Electrode Material for Energy-Storage Devices. *Scr. Mater.* **2013**, *68*, 659–662. [CrossRef]
398. Adalati, R.; Sharma, M.; Sharma, S.; Kumar, A.; Malik, G.; Boukherroub, R.; Chandra, R. Metal Nitrides as Efficient Electrode Material for Supercapacitors: A Review. *J. Energy Storage* **2022**, *56*, 105912. [CrossRef]
399. Robert, K.; Stiévenard, D.; Deresmes, D.; Douard, C.; Iadecola, A.; Troadec, D.; Simon, P.; Nuns, N.; Marinova, M.; Huvé, M.; et al. Novel Insights into the Charge Storage Mechanism in Pseudocapacitive Vanadium Nitride Thick Films for High-Performance on-Chip Micro-Supercapacitors. *Energy Environ. Sci.* **2020**, *13*, 949–957. [CrossRef]
400. Lucio-Porto, R.; Bouhtiyya, S.; Pierson, J.F.; Morel, A.; Capon, F.; Boulet, P.; Brousse, T. VN Thin Films as Electrode Materials for Electrochemical Capacitors. *Electrochim. Acta* **2014**, *141*, 203–211. [CrossRef]
401. Bondarchuk, O.; Morel, A.; Bélanger, D.; Goikolea, E.; Brousse, T.; Mysyk, R. Thin Films of Pure Vanadium Nitride: Evidence for Anomalous Non-Faradaic Capacitance. *J. Power Sources* **2016**, *324*, 439–446. [CrossRef]
402. Zhou, Y.; Guo, W.; Li, T. A Review on Transition Metal Nitrides as Electrode Materials for Supercapacitors. *Ceram. Int.* **2019**, *45*, 21062–21076. [CrossRef]
403. Durai, G.; Kuppusami, P.; Maiyalagan, T.; Theerthagiri, J.; Vinoth Kumar, P.; Kim, H.S. Influence of Chromium Content on Microstructural and Electrochemical Supercapacitive Properties of Vanadium Nitride Thin Films Developed by Reactive Magnetron Co-Sputtering Process. *Ceram. Int.* **2019**, *45*, 12643–12653. [CrossRef]
404. Li, Q.; Chen, Y.; Zhang, J.; Tian, W.; Wang, L.; Ren, Z.; Ren, X.; Li, X.; Gao, B.; Peng, X.; et al. Spatially Confined Synthesis of Vanadium Nitride Nanodots Intercalated Carbon Nanosheets with Ultrahigh Volumetric Capacitance and Long Life for Flexible Supercapacitors. *Nano Energy* **2018**, *51*, 128–136. [CrossRef]
405. Chen, L.; Liu, C.; Zhang, Z. Novel [111] Oriented γ-Mo_2N Thin Films Deposited by Magnetron Sputtering as an Anode for Aqueous Micro-Supercapacitors. *Electrochim. Acta* **2017**, *245*, 237–248. [CrossRef]
406. Dinh, K.H.; Robert, K.; Thuriot-Roukos, J.; Huvé, M.; Simon, P.; Troadec, D.; Lethien, C.; Roussel, P. Wafer-Scale Performance Mapping of Magnetron-Sputtered Ternary Vanadium Tungsten Nitride for Microsupercapacitors. *Chem. Mater.* **2023**, *35*, 8654–8663. [CrossRef]
407. Wei, B.; Liang, H.; Zhang, D.; Qi, Z.; Shen, H.; Wang, Z. Magnetron Sputtered TiN Thin Films toward Enhanced Performance Supercapacitor Electrodes. *Mater. Renew. Sustain. Energy* **2018**, *7*, 11. [CrossRef]
408. Achour, A.; Porto, R.L.; Soussou, M.A.; Islam, M.; Boujtita, M.; Aissa, K.A.; Le Brizoual, L.; Djouadi, A.; Brousse, T. Titanium Nitride Films for Micro-Supercapacitors: Effect of Surface Chemistry and Film Morphology on the Capacitance. *J. Power Sources* **2015**, *300*, 525–532. [CrossRef]
409. Achour, A.; Lucio-Porto, R.; Chaker, M.; Arman, A.; Ahmadpourian, A.; Soussou, M.A.; Boujtita, M.; Le Brizoual, L.; Djouadi, M.A.; Brousse, T. Titanium Vanadium Nitride Electrode for Micro-Supercapacitors. *Electrochem. Commun.* **2017**, *77*, 40–43. [CrossRef]
410. Cui, H.; Zhu, G.; Liu, X.; Liu, F.; Xie, Y.; Yang, C.; Lin, T.; Gu, H.; Huang, F. Niobium Nitride Nb4N5 as a New High-Performance Electrode Material for Supercapacitors. *Adv. Sci.* **2015**, *2*, 1500126. [CrossRef] [PubMed]
411. Wei, B.; Liang, H.; Zhang, D.; Wu, Z.; Qi, Z.; Wang, Z. CrN Thin Films Prepared by Reactive DC Magnetron Sputtering for Symmetric Supercapacitors. *J. Mater. Chem. A Mater.* **2017**, *5*, 2844–2851. [CrossRef]
412. Qi, Z.; Wei, B.; Wang, J.; Yang, Y.; Wang, Z. Nanostructured Porous CrN Thin Films by Oblique Angle Magnetron Sputtering for Symmetric Supercapacitors. *J. Alloys Compd.* **2019**, *806*, 953–959. [CrossRef]
413. Wei, B.; Mei, G.; Liang, H.; Qi, Z.; Zhang, D.; Shen, H.; Wang, Z. Porous CrN Thin Films by Selectively Etching CrCuN for Symmetric Supercapacitors. *J. Power Sources* **2018**, *385*, 39–44. [CrossRef]

414. Durai, G.; Kuppusami, P.; Maiyalagan, T.; Ahila, M.; Vinoth kumar, P. Supercapacitive Properties of Manganese Nitride Thin Film Electrodes Prepared by Reactive Magnetron Sputtering: Effect of Different Electrolytes. *Ceram. Int.* **2019**, *45*, 17120–17127. [CrossRef]
415. Xie, Y.; Tian, F. Capacitive Performance of Molybdenum Nitride/Titanium Nitride Nanotube Array for Supercapacitor. *Mater. Sci. Eng. B* **2017**, *215*, 64–70. [CrossRef]
416. Zhang, H.; Hu, W.; Wei, B.; Zheng, J.; Qi, Z.; Wang, Z. Freestanding Co3N Thin Film for High Performance Supercapacitors. *Ceram. Int.* **2021**, *47*, 3267–3271. [CrossRef]
417. Achour, A.; Ducros, J.B.; Porto, R.L.; Boujtita, M.; Gautron, E.; Le Brizoual, L.; Djouadi, M.A.; Brousse, T. Hierarchical Nanocomposite Electrodes Based on Titanium Nitride and Carbon Nanotubes for Micro-Supercapacitors. *Nano Energy* **2014**, *7*, 104–113. [CrossRef]
418. Salman, A.; Padmajan Sasikala, S.; Kim, I.H.; Kim, J.T.; Lee, G.S.; Kim, J.G.; Kim, S.O. Tungsten Nitride-Coated Graphene Fibers for High-Performance Wearable Supercapacitors. *Nanoscale* **2020**, *12*, 20239–20249. [CrossRef]
419. Zhang, W.-B.; Ma, X.-J.; Kong, L.-B.; Luo, Y.-C.; Kang, L. Capacitive Intermetallic Manganese Nitride with High Volumetric Energy Densities. *J. Electrochem. Soc.* **2016**, *163*, A2830. [CrossRef]
420. Sun, N.; Zhou, D.; Liu, W.; Shi, S.; Tian, Z.; Liu, F.; Li, S.; Wang, J.; Ali, F. Tailoring Surface Chemistry and Morphology of Titanium Nitride Electrode for On-Chip Supercapacitors. *ACS Sustain. Chem. Eng.* **2020**, *8*, 7869–7878. [CrossRef]
421. Lv, F.; Ma, H.; Shen, L.; Jiang, Y.; Sun, T.; Ma, J.; Geng, X.; Kiran, A.; Zhu, N. Wearable Helical Molybdenum Nitride Supercapacitors for Self-Powered Healthcare Smartsensors. *ACS Appl. Mater. Interfaces* **2021**, *13*, 29780–29787. [CrossRef]
422. Shen, H.; Wei, B.; Zhang, D.; Qi, Z.; Wang, Z. Magnetron Sputtered NbN Thin Film Electrodes for Supercapacitors. *Mater. Lett.* **2018**, *229*, 17–20. [CrossRef]
423. Gao, Z.; Wu, Z.; Zhao, S.; Zhang, T.; Wang, Q. Enhanced Capacitive Property of HfN Film Electrode by Plasma Etching for Supercapacitors. *Mater. Lett.* **2019**, *235*, 148–152. [CrossRef]
424. Anusha Thampi, V.V.; Nithiyanantham, U.; Nanda Kumar, A.K.; Martin, P.; Bendavid, A.; Subramanian, B. Fabrication of Sputtered Titanium Vanadium Nitride (TiVN) Thin Films for Micro-Supercapacitors. *J. Mater. Sci. Mater. Electron.* **2018**, *29*, 12457–12465. [CrossRef]
425. Yi, C.-Q.; Zou, J.-P.; Yang, H.-Z.; Leng, X. Recent Advances in Pseudocapacitor Electrode Materials: Transition Metal Oxides and Nitrides. *Trans. Nonferrous Met. Soc. China (Engl. Ed.)* **2018**, *28*, 1980–2001. [CrossRef]
426. Zhao, J.; Li, C.; Zhang, Q.; Zhang, J.; Wang, X.; Lin, Z.; Wang, J.; Lv, W.; Lu, C.; Wong, C.P.; et al. An All-Solid-State, Lightweight, and Flexible Asymmetric Supercapacitor Based on Cabbage-like $ZnCo_2O_4$ and Porous VN Nanowires Electrode Materials. *J. Mater. Chem. A Mater.* **2017**, *5*, 6928–6936. [CrossRef]
427. Wei, B.; Shang, C.; Shui, L.; Wang, X.; Zhou, G. TiVN Composite Hollow Mesospheres for High-Performance Supercapacitors. *Mater. Res. Express* **2019**, *6*, 025801. [CrossRef]
428. Su, Y.; Zhitomirsky, I. Hybrid MnO_2/Carbon Nanotube-VN/Carbon Nanotube Supercapacitors. *J. Power Sources* **2014**, *267*, 235–242. [CrossRef]
429. Wei, B.; Ming, F.; Liang, H.; Qi, Z.; Hu, W.; Wang, Z. All Nitride Asymmetric Supercapacitors of Niobium Titanium Nitride-Vanadium Nitride. *J. Power Sources* **2021**, *481*, 228842. [CrossRef]
430. Ma, J.; Zheng, S.; Cao, Y.; Zhu, Y.; Das, P.; Wang, H.; Liu, Y.; Wang, J.; Chi, L.; Liu, S.; et al. Aqueous MXene/PH1000 Hybrid Inks for Inkjet-Printing Micro-Supercapacitors with Unprecedented Volumetric Capacitance and Modular Self-Powered Microelectronics. *Adv. Energy Mater.* **2021**, *11*, 2100746. [CrossRef]
431. Zheng, S.; Wang, H.; Das, P.; Zhang, Y.; Cao, Y.; Ma, J.; Liu, S.; Wu, Z.S. Multitasking MXene Inks Enable High-Performance Printable Microelectrochemical Energy Storage Devices for All-Flexible Self-Powered Integrated Systems. *Adv. Mater.* **2021**, *33*, 2005449. [CrossRef] [PubMed]
432. Orangi, J.; Hamade, F.; Davis, V.A.; Beidaghi, M. 3D Printing of Additive-Free 2D $Ti_3C_2T_x$ (MXene) Ink for Fabrication of Micro-Supercapacitors with Ultra-High Energy Densities. *ACS Nano* **2020**, *14*, 640–650. [CrossRef] [PubMed]
433. Li, H.; Li, X.; Liang, J.; Chen, Y. Hydrous RuO_2-Decorated MXene Coordinating with Silver Nanowire Inks Enabling Fully Printed Micro-Supercapacitors with Extraordinary Volumetric Performance. *Adv. Energy Mater.* **2019**, *9*, 1803987. [CrossRef]
434. Jiang, Q.; Lei, Y.; Liang, H.; Xi, K.; Xia, C.; Alshareef, H.N. Review of MXene Electrochemical Microsupercapacitors. *Energy Storage Mater.* **2020**, *27*, 78–95. [CrossRef]
435. Salles, P.; Quain, E.; Kurra, N.; Sarycheva, A.; Gogotsi, Y. Automated Scalpel Patterning of Solution Processed Thin Films for Fabrication of Transparent MXene Microsupercapacitors. *Small* **2018**, *14*, e1802864. [CrossRef]
436. Hu, H.; Bai, Z.; Niu, B.; Wu, M.; Hua, T. Binder-Free Bonding of Modularized MXene Thin Films into Thick Film Electrodes for on-Chip Micro-Supercapacitors with Enhanced Areal Performance Metrics. *J. Mater. Chem. A Mater.* **2018**, *6*, 14876–14884. [CrossRef]
437. Biswas, A.; Natu, V.; Puthirath, A.B. Thin-Film Growth of MAX Phases as Functional Materials. *Oxf. Open Mater. Sci.* **2021**, *1*, itab020. [CrossRef]
438. Ling, Z.; Ren, C.E.; Zhao, M.Q.; Yang, J.; Giammarco, J.M.; Qiu, J.; Barsoum, M.W.; Gogotsi, Y. Flexible and Conductive MXene Films and Nanocomposites with High Capacitance. *Proc. Natl. Acad. Sci. USA* **2014**, *111*, 16676–16681. [CrossRef]

439. Lukatskaya, M.R.; Kota, S.; Lin, Z.; Zhao, M.Q.; Shpigel, N.; Levi, M.D.; Halim, J.; Taberna, P.L.; Barsoum, M.W.; Simon, P.; et al. Ultra-High-Rate Pseudocapacitive Energy Storage in Two-Dimensional Transition Metal Carbides. *Nat. Energy* **2017**, *6*, 17105. [CrossRef]
440. Lukatskaya, M.R.; Bak, S.M.; Yu, X.; Yang, X.Q.; Barsoum, M.W.; Gogotsi, Y. Probing the Mechanism of High Capacitance in 2D Titanium Carbide Using in Situ X-Ray Absorption Spectroscopy. *Adv. Energy Mater.* **2015**, *5*, 1500589. [CrossRef]
441. Peng, Y.Y.; Akuzum, B.; Kurra, N.; Zhao, M.Q.; Alhabeb, M.; Anasori, B.; Kumbur, E.C.; Alshareef, H.N.; Ger, M.-D.; Gogotsi, Y. All-MXene (2D Titanium Carbide) Solid-State Microsupercapacitors for on-Chip Energy Storage. *Energy Environ. Sci.* **2016**, *9*, 2847–2854. [CrossRef]
442. Jiao, S.; Zhou, A.; Wu, M.; Hu, H. Kirigami Patterning of MXene/Bacterial Cellulose Composite Paper for All-Solid-State Stretchable Micro-Supercapacitor Arrays. *Adv. Sci.* **2019**, *6*, 1900529. [CrossRef] [PubMed]
443. Yuan, M.; Wang, L.; Liu, X.; Du, X.; Zhang, G.; Chang, Y.; Xia, Q.; Hu, Q.; Zhou, A. 3D Printing Quasi-Solid-State Micro-Supercapacitors with Ultrahigh Areal Energy Density Based on High Concentration MXene Sediment. *Chem. Eng. J.* **2023**, *451*, 138686. [CrossRef]
444. Zhang, C.J.; Kremer, M.P.; Seral-Ascaso, A.; Park, S.H.; McEvoy, N.; Anasori, B.; Gogotsi, Y.; Nicolosi, V. Stamping of Flexible, Coplanar Micro-Supercapacitors Using MXene Inks. *Adv. Funct. Mater.* **2018**, *28*, 1705506. [CrossRef]
445. Li, H.; Hou, Y.; Wang, F.; Lohe, M.R.; Zhuang, X.; Niu, L.; Feng, X.; Li, H.; Hou, Y.; Wang, F.; et al. Flexible All-Solid-State Supercapacitors with High Volumetric Capacitances Boosted by Solution Processable MXene and Electrochemically Exfoliated Graphene. *Adv. Energy Mater.* **2017**, *7*, 1601847. [CrossRef]
446. Hu, H.; Hua, T. An Easily Manipulated Protocol for Patterning of MXenes on Paper for Planar Micro-Supercapacitors. *J. Mater. Chem. A Mater.* **2017**, *5*, 19639–19648. [CrossRef]
447. Huang, H.; Su, H.; Zhang, H.; Xu, L.; Chu, X.; Hu, C.; Liu, H.; Chen, N.; Liu, F.; Deng, W.; et al. Extraordinary Areal and Volumetric Performance of Flexible Solid-State Micro-Supercapacitors Based on Highly Conductive Freestanding $Ti_3C_2T_x$ Films. *Adv. Electron. Mater.* **2018**, *4*, 1800179. [CrossRef]
448. Li, P.; Shi, W.; Liu, W.; Chen, Y.; Xu, X.; Ye, S.; Yin, R.; Zhang, L.; Xu, L.; Cao, X. Fabrication of High-Performance MXene-Based All-Solid-State Flexible Microsupercapacitor Based on a Facile Scratch Method. *Nanotechnology* **2018**, *29*, 445401. [CrossRef]
449. Wang, G.; Zhang, R.; Zhang, H.; Cheng, K. Aqueous MXene Inks for Inkjet-Printing Microsupercapacitors with Ultrahigh Energy Densities. *J. Colloid. Interface Sci.* **2023**, *645*, 359–370. [CrossRef]
450. Jiang, Q.; Kurra, N.; Maleski, K.; Lei, Y.; Liang, H.; Zhang, Y.; Gogotsi, Y.; Alshareef, H.N. On-Chip MXene Microsupercapacitors for AC-Line Filtering Applications. *Adv. Energy Mater.* **2019**, *9*, 1901061. [CrossRef]
451. Zhu, Y.; Zhang, Q.; Ma, J.; Das, P.; Zhang, L.; Liu, H.; Wang, S.; Li, H.; Wu, Z.S. Three-Dimensional (3D)-Printed MXene High-Voltage Aqueous Micro-Supercapacitors with Ultrahigh Areal Energy Density and Low-Temperature Tolerance. *Carbon Energy* **2024**, *6*, e481. [CrossRef]
452. Fan, Z.; Wang, Y.; Xie, Z.; Wang, D.; Yuan, Y.; Kang, H.; Su, B.; Cheng, Z.; Liu, Y. Modified MXene/Holey Graphene Films for Advanced Supercapacitor Electrodes with Superior Energy Storage. *Adv. Sci.* **2018**, *5*, 1800750. [CrossRef]
453. Kim, E.; Lee, B.J.; Maleski, K.; Chae, Y.; Lee, Y.; Gogotsi, Y.; Ahn, C.W. Microsupercapacitor with a 500 Nm Gap between MXene/CNT Electrodes. *Nano Energy* **2021**, *81*, 105616. [CrossRef]
454. Liu, W.; Wang, Z.; Su, Y.; Li, Q.; Zhao, Z.; Geng, F. Molecularly Stacking Manganese Dioxide/Titanium Carbide Sheets to Produce Highly Flexible and Conductive Film Electrodes with Improved Pseudocapacitive Performances. *Adv. Energy Mater.* **2017**, *7*, 1602834. [CrossRef]
455. Tian, Y.; Yang, C.; Que, W.; Liu, X.; Yin, X.; Kong, L.B. Flexible and Free-Standing 2D Titanium Carbide Film Decorated with Manganese Oxide Nanoparticles as a High Volumetric Capacity Electrode for Supercapacitor. *J. Power Sources* **2017**, *359*, 332–339. [CrossRef]
456. Zhao, M.-Q.; Ren, C.E.; Ling, Z.; Lukatskaya, M.R.; Zhang, C.; Van Aken, K.L.; Barsoum, M.W.; Gogotsi, Y.; Zhao, M.; Ren, C.E.; et al. Flexible MXene/Carbon Nanotube Composite Paper with High Volumetric Capacitance. *Adv. Mater.* **2015**, *27*, 339–345. [CrossRef]
457. Yan, J.; Ren, C.E.; Maleski, K.; Hatter, C.B.; Anasori, B.; Urbankowski, P.; Sarycheva, A.; Gogotsi, Y. Flexible MXene/Graphene Films for Ultrafast Supercapacitors with Outstanding Volumetric Capacitance. *Adv. Funct. Mater.* **2017**, *27*, 1701264. [CrossRef]
458. Qin, L.; Tao, Q.; Liu, X.; Fahlman, M.; Halim, J.; Persson, P.O.Å.; Rosen, J.; Zhang, F. Polymer-MXene Composite Films Formed by MXene-Facilitated Electrochemical Polymerization for Flexible Solid-State Microsupercapacitors. *Nano Energy* **2019**, *60*, 734–742. [CrossRef]
459. Zhang, C.J.; McKeon, L.; Kremer, M.P.; Park, S.H.; Ronan, O.; Seral-Ascaso, A.; Barwich, S.; Coileáin, C.; McEvoy, N.; Nerl, H.C.; et al. Additive-Free MXene Inks and Direct Printing of Micro-Supercapacitors. *Nat. Commun.* **2019**, *10*, 1795. [CrossRef]
460. Wang, Y.; Zhang, Y.Z.; Dubbink, D.; ten Elshof, J.E. Inkjet Printing of δ-MnO_2 Nanosheets for Flexible Solid-State Micro-Supercapacitor. *Nano Energy* **2018**, *49*, 481–488. [CrossRef]
461. Li, L.; Secor, E.B.; Chen, K.S.; Zhu, J.; Liu, X.; Gao, T.Z.; Seo, J.W.T.; Zhao, Y.; Hersam, M.C. High-Performance Solid-State Supercapacitors and Microsupercapacitors Derived from Printable Graphene Inks. *Adv. Energy Mater.* **2016**, *6*, 1600909. [CrossRef]
462. Van Toan, N.; Kim Tuoi, T.T.; Li, J.; Inomata, N.; Ono, T. Liquid and Solid States On-Chip Micro-Supercapacitors Using Silicon Nanowire-Graphene Nanowall-Pani Electrode Based on Microfabrication Technology. *Mater. Res. Bull.* **2020**, *131*, 110977. [CrossRef]

463. Wang, K.; Zou, W.; Quan, B.; Yu, A.; Wu, H.; Jiang, P.; Wei, Z. An All-Solid-State Flexible Micro-Supercapacitor on a Chip. *Adv. Energy Mater.* **2011**, *1*, 1068–1072. [CrossRef]
464. Xu, K. Nonaqueous Liquid Electrolytes for Lithium-Based Rechargeable Batteries. *Chem. Rev.* **2004**, *104*, 4303–4418. [CrossRef]
465. Pal, B.; Yang, S.; Ramesh, S.; Thangadurai, V.; Jose, R. Electrolyte Selection for Supercapacitive Devices: A Critical Review. *Nanoscale Adv.* **2019**, *1*, 3807–3835. [CrossRef]
466. Mendhe, A.; Panda, H.S. Discover Materials A Review on Electrolytes for Supercapacitor Device. *Discov Mater* **2023**, *3*, 29. [CrossRef]
467. Yu, L.; Chen, G.Z. Ionic Liquid-Based Electrolytes for Supercapacitor and Supercapattery. *Front. Chem.* **2019**, *7*, 272. [CrossRef]
468. Bhat, M.Y.; Hashmi, S.A.; Khan, M.; Choi, D.; Qurashi, A. Frontiers and Recent Developments on Supercapacitor's Materials, Design, and Applications: Transport and Power System Applications. *J. Energy Storage* **2023**, *58*, 106104. [CrossRef]
469. Wang, R.; Li, Q.; Cheng, L.; Li, H.; Wang, B.; Zhao, X.S.; Guo, P. Electrochemical Properties of Manganese Ferrite-Based Supercapacitors in Aqueous Electrolyte: The Effect of Ionic Radius. *Colloids Surf. A Physicochem. Eng. Asp.* **2014**, *457*, 94–99. [CrossRef]
470. Zhu, J.; Xu, Y.; Wang, J.; Lin, J.; Sun, X.; Mao, S. The Effect of Various Electrolyte Cations on Electrochemical Performance of Polypyrrole/RGO Based Supercapacitors. *Phys. Chem. Chem. Phys.* **2015**, *17*, 28666–28673. [CrossRef] [PubMed]
471. Wu, H.; Wang, X.; Jiang, L.; Wu, C.; Zhao, Q.; Liu, X.; Hu, B.; Yi, L. The Effects of Electrolyte on the Supercapacitive Performance of Activated Calcium Carbide-Derived Carbon. *J. Power Sources* **2013**, *226*, 202–209. [CrossRef]
472. Lim, Y.; Yoon, J.; Yun, J.; Kim, D.; Hong, S.Y.; Lee, S.J.; Zi, G.; Ha, J.S. Erratum: Biaxially Stretchable, Integrated Array of High Performance Microsupercapacitors. *ACS Nano* **2014**, *8*, 11639–11650, Erratum in *ACS Nano* **2015**, *9*, 6634. [CrossRef]
473. Armand, M.; Endres, F.; MacFarlane, D.R.; Ohno, H.; Scrosati, B. Ionic-Liquid Materials for the Electrochemical Challenges of the Future. *Nat. Mater.* **2009**, *8*, 621–629. [CrossRef]
474. Liew, C.W.; Arifin, K.H.; Kawamura, J.; Iwai, Y.; Ramesh, S.; Arof, A.K. Effect of Halide Anions in Ionic Liquid Added Poly(Vinyl Alcohol)-Based Ion Conductors for Electrical Double Layer Capacitors. *J. Non Cryst. Solids* **2017**, *458*, 97–106. [CrossRef]
475. Rennie, A.J.R.; Sanchez-Ramirez, N.; Torresi, R.M.; Hall, P.J. Ether-Bond-Containing Ionic Liquids as Supercapacitor Electrolytes. *J. Phys. Chem. Lett.* **2013**, *4*, 2970–2974. [CrossRef] [PubMed]
476. Pohlmann, S.; Olyschläger, T.; Goodrich, P.; Alvarez Vicente, J.; Jacquemin, J.; Balducci, A. Azepanium-Based Ionic Liquids as Green Electrolytes for High Voltage Supercapacitors. *J. Power Sources* **2015**, *273*, 931–936. [CrossRef]
477. Timperman, L.; Skowron, P.; Boisset, A.; Galiano, H.; Lemordant, D.; Frackowiak, E.; Béguin, F.; Anouti, M. Triethylammonium Bis(Tetrafluoromethylsulfonyl)Amide Protic Ionic Liquid as an Electrolyte for Electrical Double-Layer Capacitors. *Phys. Chem. Chem. Phys.* **2012**, *14*, 8199–8207. [CrossRef]
478. Kurig, H.; Vestli, M.; Tõnurist, K.; Jänes, A.; Lust, E. Influence of Room Temperature Ionic Liquid Anion Chemical Composition and Electrical Charge Delocalization on the Supercapacitor Properties. *J. Electrochem. Soc.* **2012**, *159*, A944. [CrossRef]
479. Łatoszyńska, A.A.; Zukowska, G.Z.; Rutkowska, I.A.; Taberna, P.L.; Simon, P.; Kulesza, P.J.; Wieczorek, W. Non-Aqueous Gel Polymer Electrolyte with Phosphoric Acid Ester and Its Application for Quasi Solid-State Supercapacitors. *J. Power Sources* **2015**, *274*, 1147–1154. [CrossRef]
480. Francisco, B.E.; Jones, C.M.; Lee, S.H.; Stoldt, C.R. Nanostructured All-Solid-State Supercapacitor Based on Li_2S-P_2S_5 Glass-Ceramic Electrolyte. *Appl. Phys. Lett.* **2012**, *100*, 103902. [CrossRef]
481. Chong, M.Y.; Numan, A.; Liew, C.W.; Ng, H.M.; Ramesh, K.; Ramesh, S. Enhancing the Performance of Green Solid-State Electric Double-Layer Capacitor Incorporated with Fumed Silica Nanoparticles. *J. Phys. Chem. Solids* **2018**, *117*, 194–203. [CrossRef]
482. Murugan, R.; Thangadurai, V.; Weppner, W. Fast Lithium Ion Conduction in Garnet-Type $Li_7La_3Zr_2O_{12}$. *Angew. Chem. -Int. Ed.* **2007**, *46*, 7778–7781. [CrossRef] [PubMed]
483. Verma, M.L.; Minakshi, M.; Singh, N.K. Synthesis and Characterization of Solid Polymer Electrolyte Based on Activated Carbon for Solid State Capacitor. *Electrochim. Acta* **2014**, *137*, 497–503. [CrossRef]
484. Pal, B.; Yasin, A.; Kunwar, R.; Yang, S.; Yusoff, M.M.; Jose, R. Polymer versus Cation of Gel Polymer Electrolytes in the Charge Storage of Asymmetric Supercapacitors. *Ind. Eng. Chem. Res.* **2019**, *58*, 654–664. [CrossRef]